

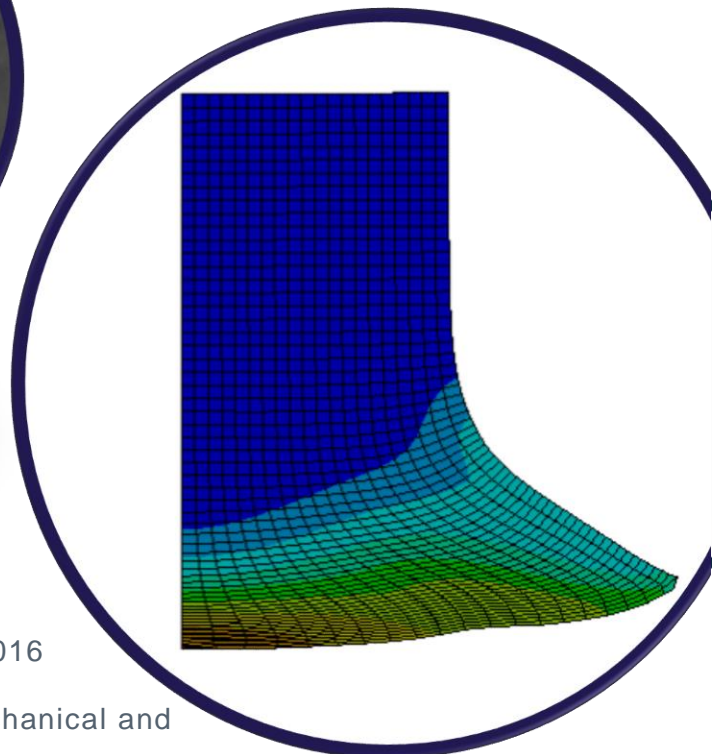
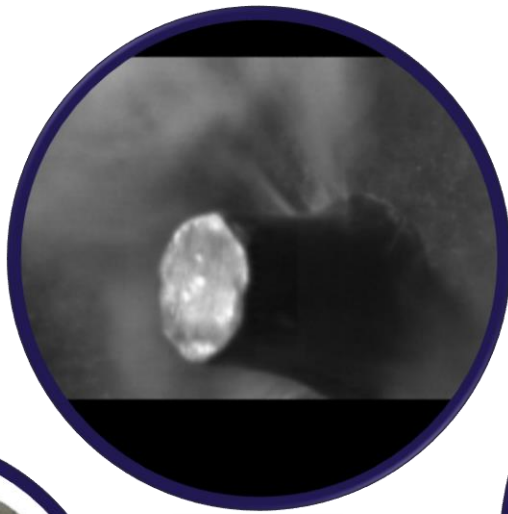


AALBORG UNIVERSITY
STUDENT REPORT

BALLISTIC PROPERTIES OF PROJECTILE MATERIAL

DMS3 2.225A

In collaboration with Composhield A/S



Autumn 2016

Department of Mechanical and
Manufacturing Engineering



AALBORG UNIVERSITY

**Department of Mechanical and
Manufacturing Engineering**

Fibigerstræde 16
DK 9220 Aalborg Øst
www.ses.aau.dk

Title:

Ballistic Properties of Projectile
material

Project period:

DMS3, Autumn semester 2016

Project group:

2.225-A

Group members:

Søren Barrett
Rasmus Viking L. R. Christiansen
Ahmad Othman

Supervisors:

Jørgen Asbøll Kepler

Number printed:

Digital

Number of pages:

76 (99)

Annex:

ZIP-archive

Submission date:

2016-12-20

Synopsis:

This report treats terminal ballistics which is the branch of the ballistic science concerning the mechanics of impact. The purpose of this project is to determine the parameters governing projectile failure when impact against a target is achieved. In the analytical approach, a model has been derived capable of determining the amount of deformation in the projectile after impact including the residual length and change in frontal area due to plastic deformation, the stress and strain distribution in the projectile and the penetration depth into the target. An already proven method is also adopted, and modified for this specific impact case, capable of determining the mass loss due to erosion and the change in length due to plastic deformation. An analytical method of obtaining the resistance pressure, by which the target resists penetration, and a method of determining the dynamic yield strength in the projectile material are also implemented. A numerical section explaining the main factors and approaches in hydrocode and dynamic modelling is also devised along with simulations of projectile impact. Finally, experimental work using the ballistic test facility on the university is conducted as validation of the former models, and as an additional source of obtaining the necessary data.

Søren Barrett

Rasmus V. L. R. Christiansen

Ahmad Othman

PREFACE

This semester project is written by group DMS3-2.225a as documentation of the group work performed on the 3rd semester of the master studies in 'Design of Mechanical Systems' under the Department of Mechanical and Manufacturing Engineering (M-tech) at Aalborg University. The project period was from the 2nd of September to the 20th of December, and the work is conducted under the supervision of associate professor Jørgen Asbøll Kepler and with help from Herluf Montes Schütte from Composhield.

The studies have made use of the commercial programs MATLAB for the analytical models and ANSYS Autodyn and ANSYS explicit dynamics for numerical models in hydrocode and parametric study. Finally the terminal ballistics test facility in the basement of Fibigerstræde 14, consisting of a gas-cannon proven for a pressure of up to 200 bars, has been used for the experimental work using compressed atmospheric air achieving velocities of 530 m/s for the given projectiles.

Appended to the report is an appendix containing additional elaborating information or data necessary for the models etc. References to the appendix sections are located in the report when necessary. As this report is in a digital version only, a file containing the additional data normally appended on a CD is located on the web-page of the report which can be found in the project database of the university. In this file, one can find video documentation of the impact, material tests, MATLAB and ANSYS files etc.

References in the report are made using the Harvard method, meaning the authors of the reference along with the year the material is published are stated in the report in [Author, year]. Additional information on the material is listed in the bibliography sorted by the last name of the first author.

We would like to thank our supervisor for counselling and assistance, Jørgen Asbøll Kepler. We would also like to thank Composhield for the cooperation, support and materials used in the project, and the company representative Herluf Montes Schütte for offering his time, guiding and support.

Abstract

This project treats terminal ballistics and the determination of parameters and effects influencing projectile failure when impacting an armour plate. By increasing this knowledge, it is perhaps possible to increase the efficiency of the armour solutions available for clients of Composhield, the proposer of this project, in theatres of operation around the world.

An analytical, a numerical and an experimental approach is taken in an attempt of determining the governing effects and three different materials are used, namely a steel, an aluminium and a brass. Furthermore, only a cylindrical projectile with a blunt face and a length of 15 mm and a diameter of $\text{Ø}10$ mm is used in the models and experiments. Such a projectile is known as a fragment simulating projectile (FSP) and represents projectiles or fragments often experienced in connection with improvised explosive devices (IED).

In the analytical approach method of determining the retarding pressure of the armour plate on the projectile without use of empirical constants is derived along with an analytical approach of determining the dynamic yield strength of the projectile material as long as it is used for impacts below the plastic wave velocity in the material. Based on this work, a model capable of determining the amount of deformation, both in the longitudinal and radial direction including the stress-distribution and the penetration depth into the target, is set up. This model yields a very good correlation with experimental and numerical findings. Less successfully, a model for impact of projectiles on ceramics is adopted and modified for projectile to steel impact is adopted. This model is capable of treating impacts above the plastic wave velocity and thereby erosion, i.e. mass loss, of the projectile. The modifications made for this model is however not sufficient, and a rather poor correlation with experiments and simulation is found.

In the numerical approach, use of hydrocode in ANSYS Autodyne and Explicit Dynamics is made. Different methods and material models are presented. Assumption and validity of axisymmetry is verified for the case of cylindrical projectiles. A convergence study is conducted to validate and determine optimal mesh size. Simulations mimicking the experimental set up is conducted and post impact length of projectiles are obtained for steel and aluminium. Numeric element erosion and failure are omitted from final simulations. The conducted simulations shows good correlation with experimental results.

In the experimental work, as wide a velocity range as possible on the available test equipment has been tested in an attempt to verify the models above in as wide a range as possible. Furthermore, observations in the projectiles after impact yield some additional information models and simulations do not show. A test campaign of the three materials with two shots at six different velocities for a total of 28 impacts is conducted in a velocity range of $\{220 - 530\}$ m/s. Both ductile fractures, i.e. plastic deformation in a shape known as mushrooming, and brittle fractures are observed. The models are not capable of modelling the brittle failures, and these are therefore omitted in the comparison of the results from the different approaches.

CONTENTS

Abstract	i
1 Introduction	1
1.1 Report summary	2
2 Definition of Problem	5
2.1 Terminal Ballistics	5
2.1.1 Threats in terminal ballistics	5
2.1.2 Neutralization of threats in terminal ballistics	6
2.1.3 Passive armour material options	8
2.2 Projectile defeat mechanisms	11
2.2.1 Wave propagation	11
2.2.2 Three phases of terminal ballistic	12
3 Analytical Model of Projectile Deformation	15
3.1 Assumptions	15
3.2 Retarding force the target exerts on the projectile	16
3.2.1 Rigid projectiles	21
3.2.2 Non rigid projectiles	23
3.2.3 Approach for deformation threshold velocity v_d	24
3.3 Analytical model for deformed projectiles	25
3.3.1 Main assumptions	25
3.3.2 Derivation of the model equations	27
3.3.3 Verification of the model	32
3.4 Modified model by den Reijer	33
3.4.1 Assumptions and simplifications	34
3.4.2 Projectile model	35
3.5 Implementation of model on present study	39
4 Numerical simulations	45
4.1 Methods	45
4.1.1 Lagrange	45
4.1.2 Euler	46
4.1.3 ALE	46
4.1.4 SPH	46

4.2	Material models	47
4.2.1	Equation of State	47
4.2.2	Strength	47
4.2.3	Failure	48
4.3	Simulations and results	49
4.3.1	Comparing axisymmetric and full 3D	49
4.3.2	Convergence study of hydrocode	50
4.3.3	Simulation of experiments	53
4.3.4	Choosing materials	53
5	Experiments and Laboratory Work	55
5.1	Presentation of experimental equipment and set-up	55
5.1.1	Ballistic test facility	55
5.1.2	Projectiles	56
5.1.3	Targets	57
5.2	Test campaign	58
5.3	Experimental observations on projectiles	59
5.4	Failure criteria	65
6	Comparison of the analytical, numerical, and experimental results	69
6.1	Model derived in section 3.3 and Experiments	69
6.2	Modified den Reijer Model and Experiments	71
6.3	Hydrocode and Experiments	72
6.4	Graphical comparison of results	73
7	Conclusion	75
	Bibliography	77
	Nomenclature	81
A	Model by den Reijer in a modified version	83
B	Hardness test	89
C	Tensile and Compression test	91
D	Obtaining material constants using numerical optimisation	97
	Annex	99

CHAPTER 1

INTRODUCTION

In previous, current and future theatre of operations, the need for protection from armour against still more severe threats of advanced projectiles and fragments from explosive devices is ever present. As the projectiles and fragments are becoming increasingly more effective against regular improvised passive armour such as a steel plate, the development of effective armour against this threat is likewise becoming increasingly important. Especially in cases where the more effective threat cannot be eliminated by using an even thicker steel plate, such as on vehicles where manoeuvrability, operational range, driveability, cargo hold and stealth capabilities etc. are greatly influenced by the bulk of the applied armour. This has led to the development of composite-armour which is now an essential part of modern armour solutions. The composite armour utilise the great compressive strength of ceramics confined by composite material with high specific toughness and strength entailing a very capable lightweight substitute for e.g. steel when it comes to neutralizing the threats.

A company with a market-share in this specific type of armour-design is Composhield and they have proposed a project in which investigations on the ballistic properties of the projectile materials are to be conducted with the aim of prospective determine unknown ballistic or material weaknesses in the interaction between projectile and armour that can be exploited in the armour design. For academic purposes, analytical, numerical and experimental models are used in determining and describing projectile behaviour for different materials on different target situations.

Company profile

Composhield A/S, a contraction of Composite Shielding, was formed in year 2000 after it had been running as an internal research project in the company Giantcode A/S since year 1996 developing novel technologies for patent applications, [Composhield, 2016]. The company now holds on to seven patent or patent pending technologies and products, and, as part of an expansion process into the North American market, is a part of a joint-venture with AT&F (American Tank and Fabrication Company) called AMTANK Armor since 2007.

The company strategy is to develop technologies with superior quality and make strategic partnerships with the purpose of becoming the preferred supplier of protective solutions for military and civilian use.

1.1 Report summary

The following section offers a brief overview of the chapters of the report. The purpose is to guide the reader and explain some of the reasoning behind the different parts of the report.

Aim of the project

The goals of this project are to receive a solid understanding of the parameters governing terminal ballistics, and especially to achieve a sound understanding of projectile behaviour and modelling during impact. This understanding is achieved through some extensive analytical and numerical modelling, along with some experimental work. The main tasks in the analytical modelling are to understand and sort the parameters and equations implemented in a wide spectrum of models, often contradicting, to set-up a valid model and determine some of the key parameters in projectile defeat. For the numerical models, the main task is to understand the use of hydrocode and the effects the different parameters have on the accuracy of the numerical simulation and enhance our abilities to use the powerful numerical tools available in our professional life afterwards. The experimental work necessary in a project like this serves a similar purpose, along with abilities of interpreting experimental data, as analytical and numerical models basically are worthless if the real world does not yield the same results, granted that the experimental work is conducted after good scientific practice.

Report overview

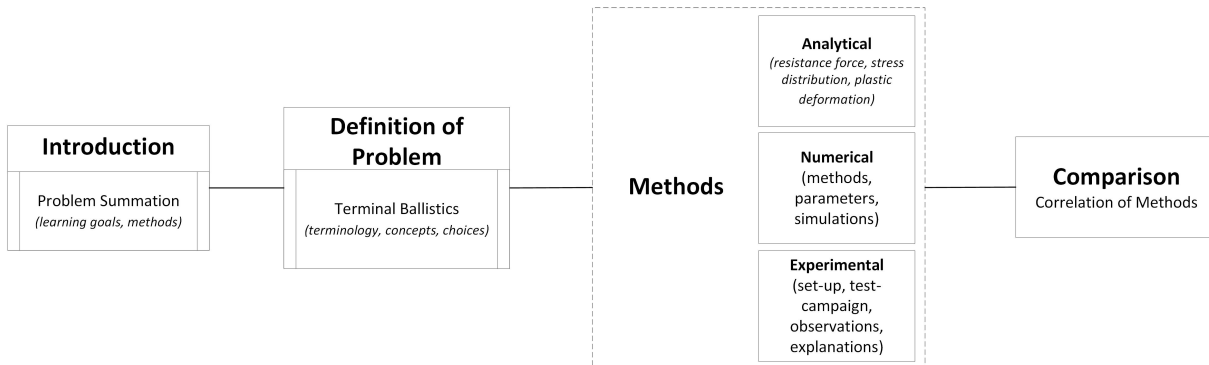


Figure 1.1: *Visualisation of the report/project summary.*

Chapter 2 - Definition of Problem.

This chapter briefly explains the concept of terminal ballistics including a presentation of the threats in the theatre of operation, methods of neutralising these threats, material options when choosing the method of neutralisation and mechanisms governing the neutralisation of a given threat. The purpose of these sections are to get an inexperienced person within the field of terminal ballistics 'up-to-speed' with regards to the terminology used throughout the remainder of the project. Furthermore, the explanations of some choices regarding projectiles for experiments, materials etc. are found in this chapter.

Chapter 3 - Analytical Model of Projectile Deformation.

This chapter presents the analytical work performed during the project, along with the necessary assumptions and approximations made within a relatively empirical research field. The chapter includes a semi-analytical approach for determining the pressure a given armour plate resists penetration of a projectile, dependent on i.a. the projectile shape both for rigid and non-rigid projectiles. Using the method of the target resistance force, a model for calculating the deformation shape, strains and stress-distribution in a non-rigid cylindrical projectile is developed. This is followed by a presentation of a model developed for impact on ceramics by [den Reijer, 1991], and modified for use in this present study. This model is able to describe the erosion and reduction in length due to plastic deformation in a projectile.

The chapter also includes a section describing how the necessary parameters for use in the methods are determined or approximated.

Chapter 4 - Numerical simulations.

Numerical simulations of impacts is likewise performed and presented in this chapter. The theory behind use of hydrocodes are explained to achieve a sound understanding of the different parameters and tools available in the simulations, and the impact these parameters have on the exactness of simulation.

Chapter 5 - Experiments and Laboratory Work.

A presentation of the experimental equipment and set-up is given in this chapter, including the projectiles and targets used in the experiments. This is followed by a presentation of the test-campaign conducted for validation of the analytical and numerical models and simulations. A variety of observations are made during the experiments, and in a section of this chapter an attempt is made for explaining these observation by use of known failure criteria and stress patterns.

Chapter 6 - Comparison of the analytical, numerical, and experimental results.

This chapter serves as summary of the different methods applied through the project, and presents a comparison of the results across the analytical, numerical and experimental work, followed by some explanation of possible discrepancies noticed.

CHAPTER 2

DEFINITION OF PROBLEM

The following chapter treats terminal ballistics, i.e. the mechanics of impact, on an introductory level by introducing the terminology, definitions and considerations with relevance, or applying, for this project.

2.1 Terminal Ballistics

Ballistics is the science of mechanics dealing with launch, flight and end effects of projectiles. A complete ballistic model is commonly separated into three branches each consisting of specific characteristics. These branches are;

interior ballistics treating the dynamics of the projectile during launch

exterior ballistics treating the trajectory of the projectile

terminal ballistics concerning the interaction between projectile and target

The current study is focused on the terminal ballistics branch.

A sample of parameters which are of importance in terminal ballistics is target density and strength, projectile density and strength, elasticity and plasticity of solids, fracture mechanics, pressure and temperature dependencies, strike angle or obliquity of target and impact velocity. The relevant impact velocities for this study is in the range of 0,5 - 2,0 km/s which is formally known as the ordnance velocity range used as the definition of the usual projectile velocity for personnel, armoured vehicles and building neutralization, [Rosenberg and Dekel, 2012], along with the sub-ordnance range. As it is only possible to reach velocities of up to ≈ 550 m/s, with the projectiles used in this project, using compressed atmospheric air in the test equipment, the ordnance range and the hypervelocity range of 2,0 km/s or faster is out of scope in this study due to these restrictions as it is impossible to experimentally validate finding etc. in the analytical and numerical models, at least using in-house experiments. In the high ordnance to hypervelocity range, the governing mechanics in the terminal ballistic changes to fluid mechanics as well, this is likewise not treated in this project.

2.1.1 Threats in terminal ballistics

The threats against armour are divided into two main classes, namely; kinetic energy projectiles and chemical energy boosted weapons.

Threats from the chemical boosted weapon class use the energy of an explosive to further increase the penetration, and perhaps perforation, capabilities against the armour. This class of threats usually takes place in the hypervelocity range and the projectile material is commonly deformed into a jet, due to the pressure from the explosive, entailing distinctive penetration mechanics. The special developed anti-armour weapons within this class

is e.g. capable of penetrating a slab of rolled homogeneous armour (RHA) of a meter in thickness. It is refrained from treating this class of threats in the present study.

The kinetic energy class of threats is furthermore dividable into, depending on the literature, two subclasses; small arms projectiles (calibre: < 20 mm) and higher-calibre projectiles (calibre: 20 mm $<$).

Small arms projectiles.

These are projectiles fired from rifle or machine gun. They consist of a penetrating mass or core that may be of a hard material such as steel or tungsten or a soft material, usually lead, depending on whether the projectile is respectively armour-piercing (AP-projectiles) and used for perforation of targets or used to cause a ballistic trauma and incapacitate a target (ball-projectiles). The penetrator core usually sets within a brass jacket for protection of the rifling in the barrel. The shape of these projectiles are often ogive simply because this is the most effective shape for target penetration and aerodynamic stability, figure 2.1, [Hazell, 2015]. The aspect ratio, i.e length-to-diameter (L/D) ratio, of these projectiles is typically in the range of 3:1 to 5:1 with muzzle velocities of up to 1000 m/s, [Deníz, 2010]. When the aspect ratio (L/D) is near 1, the projectiles are designated fragment simulators, [Rosenberg and Dekel, 2012]. These are often represented as cylinders, why this project utilise similar projectiles in the gas-cannon for experiments, analytical models and simulations.

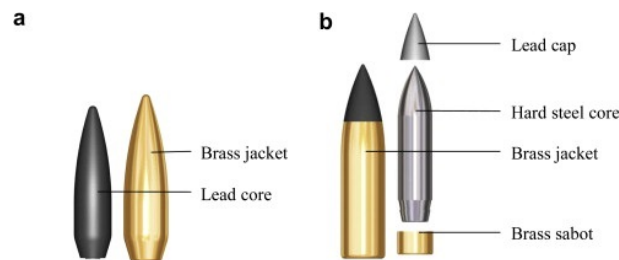


Figure 2.1: *Geometry, and composition of (a) 7,62 mm ball-projectile and (b) AP-projectile. From Børvik et al. [2009].*

Higher-calibre projectiles.

These are also known as long-rod penetrators (aspect ratio $L/D = 10$ or larger) and are usually fired from a cannon e.g. from a tank, figure 2.2. They consist of highly dense materials of steel, tungsten or depleted uranium. The aspect ratio is typically in the range of 15-30 and the muzzle velocity is in the range of 1400 - 1900 m/s. The great advantage of using a long-rod penetrator is the linear tendency between the length and the achievable penetration depth into the target.

2.1.2 Neutralization of threats in terminal ballistics

Armour in different configurations is used in neutralising the aforementioned threats, sec. 2.1.1. The classification of the armour configuration is based on the manner of neutralisation of the threat and can be separated into three groups. The classifications are passive, reactive and active armour, [Deníz, 2010].

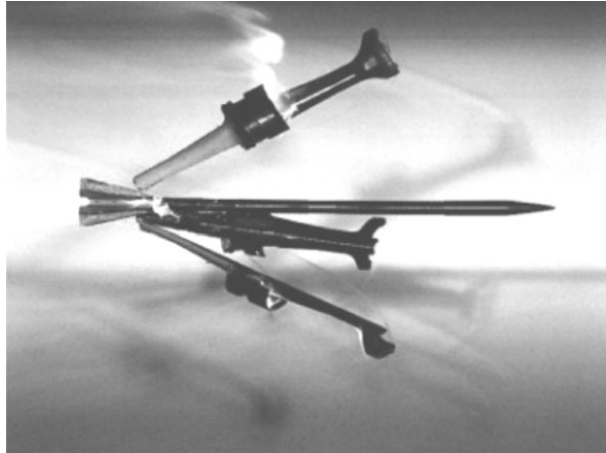


Figure 2.2: *Long-rod penetrator of the type APFS-DS (Armour Piercing Fin Stabilized - Discarding Sabot) with sabot used only for launch of the rod in the cannon (tight fit for maximum utilisation of launch pressure) and break away due to aerodynamic forces mid-flight. From Rosenberg and Dekel [2012].*

Passive armour.

This absorbs the kinetic energy in the projectile through use of material properties and/or combination of materials and/or geometric designs.

The simplest form of passive armour protection is to simply place some material between the threat and the target, e.g. a high strength steel plate. This armour might then take a direct singular impact from the threat, and has to neutralise the threat based on material properties and dimensions alone. This is generally not sufficient due to more sophisticated projectile threats or the necessary bulk of the armour is unsustainable.

Composite armour combine lightweight materials such as ceramics or polymers and high strength and high dense materials. The purpose of the lightweight material is to initiate the projectile break-up and absorb and diffuse the energy from the threat aiding the high dense material in the complete neutralisation of the projectile. This initiation of break-up and distribution of energy permits lighter armour solutions.

The passive armour solution can be divided into two components; energy disruptor or energy absorber depending on how the armour solution suppress the projectile's energy. Armours in the disruptor category neutralise the projectile by dispersing the energy through fragmentation or erosion of the projectile. This typically require the use of high strength-/high hardness materials. Armours in the absorber category neutralise the projectile by absorbing and dissipating the energy as heat through use of elastic and plastic deformation. This require the use of ductile and tough materials. Often, a combination of these two components is used in modern armour applications, e.g. a hard ceramic combined with a ductile metal back plate, often steel or aluminium.

As mentioned in sec. 2.1.1, the penetration depth is dependent on the length of the rod and jet, so as a countermeasure, spaced armour is used to initiate the jet or rod erosion, and simply increase the distance the rod or jet have to travel before perforation of the armour is achieved.

Sloped armour is inducing an obliquity between projectile and target which means the relative thickness of the armour is increased against direct line of fire. The projectile might also ricochet or deflect on the armour while the obliquity induces a bending moment in the projectile initiating break-up as well.

Reactive armour.

This neutralise the threat by reacting upon impact of a projectile and deploy design specific countermeasures often in form of a kinetic response designed to deflect or disrupt the incoming threat. The reactive is installed in-between two, often, metallic skins like a sandwich structure. Different classifications of reactive armour are used such as;

Explosive reactive armour where the reactive element is an explosive reacting to a sufficient amount of kinetic energy and accelerate the outer skin of the armour outwards deflecting the projectile or increasing the armour thickness and thereby necessary penetration depth for shaped charge jets. Similar, *non-explosive reactive armour* reacts in the same manner but does only use an energetic reactive – the definition is purely a grading-system as an explosive likewise is energetic – and the outwards pressure generated is therefore less.

Non-energetic armour uses materials that absorbs energy such as elastomers. During impact, some of the kinetic energy is dissipated into the inert elastomer layer and the resulting energy is absorbed by the armour plates.

Electromagnetic reactive armour is only in the test phase and as far it is known not implemented on any operational devices. It is effectively a capacitor under a very high voltage. During impact, the projectile closes the circuit meaning the capacitor is discharged inflecting a great amount of energy into the penetrator destroying it.

Active armour.

This uses sensors to detect incoming threats and deploy countermeasures such as a swarm of fragments effectively setting of the explosive warhead or destroying the kinetic projectile.

This study only make use of the *passive armour classification* in search of projectile defeat mechanisms.

2.1.3 Passive armour material options

A complete overview of available materials for the passive armour classification is not achieved. However, in general the available materials are metals, ceramics and polymer-composites. Within each material class exist a number of material options along with combinations across the material classes to obtain an armour that takes advantage of the specific material parameters while minimising the weight and volume and maximising the cost-benefit such as a composite armour. An introduction to available materials in this study follows.

Ceramics are a solid compound material consisting of at least a metallic and non-metallic material bounded by heat and possibly a pressure, [Hazell, 2015]. Ceramic are widely used in armour applications as the penetration mechanisms governing projectile and target in-

teraction are highly dependent on the compressive stresses. The ceramics offer great properties in compression strength and hardness, perhaps as much as an order of magnitude higher than metals, [Hazell, 2015], meaning they are ideal for initiating projectile failure. Furthermore, ceramics usually have a low density. The main concern with the ceramics are their brittleness and the many microscopical cracks, i.e. they are not very tough or capable of undergoing plastic deformation. The necessary energy to permit crack growth in ceramics are in the order of 1% of a projectiles kinetic energy, [Woodward, 1990]. This means, a second projectile strike in the already damaged zone might result in armour defeat. Common ceramics used for armour applications are alumina (Al_2O_3), boron carbide (B_4C) and silicium carbide (SiC).

Metals are still the most common material in design of armour. This is because most metals offer efficient protection due to their properties in structural and fatigue load conditions while being relatively cheap.

Different steel alloys are the most used metallic armour material because of the general great main properties as hardness, toughness and strength along with relatively easy manufacturing. Four designated groups of steel armour exists and these are *rolled-homogeneous armour (RHA)*, *high-hardness armour (HHA)*, *variable-hardness armour* and *perforated armour* and within each group the armours are sorted in different classes, table 2.1, depending on hardness and tensile strength, [Hazell, 2015]. The treats of the first two groups of steel armour are as the designation suggest. The variable-hardness armour has varying properties through the thickness of the armour plate. In these armour plates, one side is exposed to a surface hardening meaning the armour plate possess both the absorbing properties of regular ductile steel regarding crack propagation, and the projectile disruptive properties of hardened steel leading to a more effective armour plate. The perforated armour is special as holes are introduced in the armour plate intentionally. It is shown in [Chocron et al., 2001] that a projectile hitting an edge is an effective method of disrupting or fragmentate the incoming threat.

The available armour plates, ARMOX 500 and ARMOX 600 and the equivalent Quardian 500, where the number indicate the hardness in brinell (BHN), place in class 3A or class 4, as the tensile strength of these are approximately 1300 - 1600 MPa.

The **polymer-composites** such as carbon-epoxies, E-glass, S-glass and Aramids generally possess a high specific-strength and specific-stiffness due to the lay-up of fibre laminates bonded by a matrix. This make them very useful in e.g body armours against knife slash or hand-weapons, but insufficient against high energy threats unless combined with ceramic tiles.

Targets of these materials are not used in this project, and it is therefore refrained from further discussion.

Classification	Description	Hardness (BHN)	UTS (MPa)	Elongation (%)
Class 1	Readily weldable steel subjected to structural loads.	262-311	895-1050	15
Class 2	Readily weldable steel to protect against AP ammunition.	255-341	895-955	14-16
Class 3	Readily weldable higher hardness steel manufactured in thin sections.	470-540	1450-1850	8
Class 3A	Readily weldable higher hardness steel manufactured in thin sections.	420-480	1200-1600	9
Class 4	Higher carbon and alloy content higher hardness armour for thick sections.	475-605	1450-2000	7
Class 5	High alloy content armour with very high hardness used for special applications such as perforated armor.	560-655	1800-2400	6

Table 2.1: *Sub-classification of rolled-homogeneous armour (RHA) according to the UK Ministry of Defence. From Defence Procurement Agency [2002].*

2.2 Projectile defeat mechanisms

There are several ways in which a projectile may fail during a high velocity impact into an armour plate of either steel or ceramic. This section describes the wave propagation observed in the projectiles during the numerical studies, and is furthermore important as the velocity of the wave is one of the governing mechanics in projectile defeat. A description of the three phases of terminal ballistics is likewise described, as, especially, the analytical methods make use of the distinctive characteristics in each of these phases.

2.2.1 Wave propagation

When applying a load on a structure, the effect of the load is propagating through the material as a wave at a given speed, i.e. it requires a finite time before the entire structure is affected by the applied load. The speed of the wave in the elastic region is determined as

$$u_{ela} = \sqrt{\frac{E}{\rho}} \tag{2.1}$$

where E and ρ are Young's modulus and density of the material in which the wave propagate, respectively. Furthermore, u_{ela} is also the speed of sound in the material. By changing the modulus for the plastic part, one determines the plastic wave speed in the material.

In many cases, the short instance the structure is in a state of non-equilibrium as the load effect propagates through the structure is neglected. This is not feasible when studying cases where the load is applied over a very short period, i.e. terminal ballistics.

The propagation of the wave through the material is shown on a one-dimensional mass-spring system in figure 2.3. When the wave reaches the end, i.e. the last mass, the system reacts depending on the boundary conditions. If the end is restrained, the entire wave front reflects back through the system, as a compression wave. This is only the case in theory. If the end is free, the wave will, depending on the magnitude, either return as a reflection wave (tensile wave) through the system after stretching the last spring or stretch the spring beyond return, i.e. exceeding the tensile stress of the material. When the system is stretched, one might, in the case of a projectile hitting an armour plate, observe spalling or lamination failure on the backside of the plate. This results in fragments consisting of the armour plate with velocities of up to one-third of the wave-speed in the material, i.e dangerous for soft targets behind the plate, [Hazell, 2015].

It is impossible to experience a completely retained boundary condition, and the behaviour of the stress wave depends on the adjacent material. A part of the stress wave is reflected back through the system, and a part continues. This is dependent on the elastic and density properties of the adjacent materials – i.e the difference in material impedance, [Hazell, 2015].

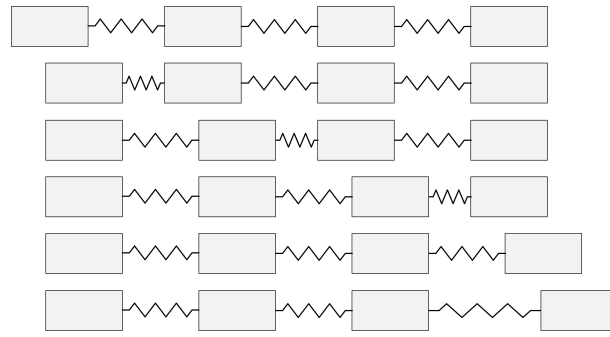


Figure 2.3: *Propagation of 'wave' in a one-dimensional mass-spring system.*

2.2.2 Three phases of terminal ballistic

Terminal ballistic, or a projectile impact, consists of three phases. An erosion phase where the projectile is losing mass, a plastic deformation phase in which the projectile deforms to a mushroom-like shape, hence in popular called mushrooming, and a rigid phase in which the projectile either penetrate the target, or is defeated by the target. Figure 2.4.

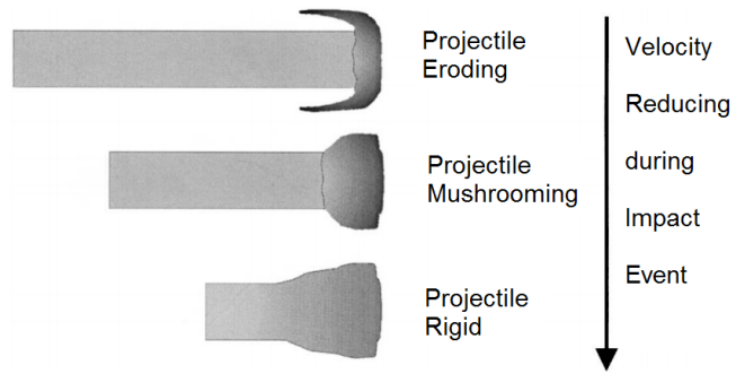


Figure 2.4: *Erosion, mushrooming and rigid behaviour of projectile, Scientific Academic Publishing [2013].*

Erosion

In terminal ballistics, the term erosion describes the phenomenon of mass loss from both projectile and target. The rate at which erosion happens is dependent on the relative velocity of the plastic wave and the material hardness between projectile and target, [Hazell, 2015]. As erosion describes the mass loss of the projectile, it implies a separation of material from the projectile. The momentum of this material, or mass, is then disregarded during modelling, figure 2.4.

Closely linked to the erosion phenomena, the projectile, at initial impact with a ceramic, experiences dwelling and during this dwelling, the projectile is losing mass due to erosion. Dwelling describes the short instance of time at which the projectile seems to be unable to penetrate the ceramic, and appears to *dwell* on the surface. The dwelling phenomena persists until the strength of the ceramics has been reduced, which happens when a

characteristic fracture cone has developed in the ceramic, figure 2.5. The fracture cone forms due to the development of a tensile wave from the reflexion of the compressive wave, initiated by the impact of the projectile, on the back face of the ceramic, similarly as described and seen in sec. 2.2.1 and figure 2.3.

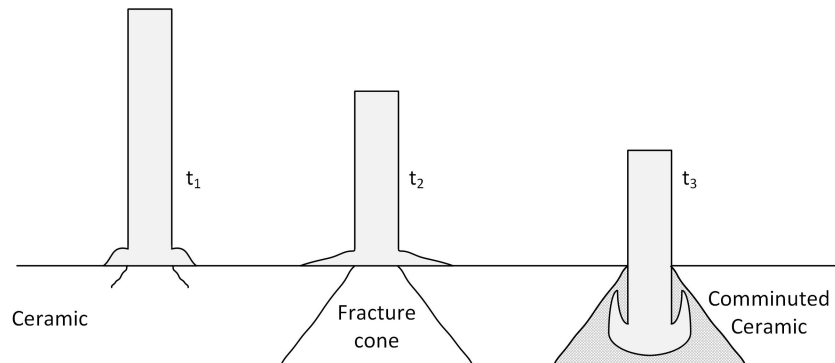


Figure 2.5: *Different phases of dwelling. The time of dwelling depend on the thickness of the ceramic, along with the speed of sound, i.e. fracture, in the ceramic material.*

Plastic deformation or Mushrooming

During projectile penetration of an armour plate, at a lower velocity than the above-described erosion, the projectile might experience plastic deformation of the tip commonly known as mushrooming. The mushrooming of a projectile is often a transition stage between erosion of the projectile, and rigid penetration. During mushrooming, the projectile expand in tip area and shortens in the longitudinal direction due to plastic deformation, figure 2.4. This reduces the penetration ability of the projectile and is therefore not desired in projectile/armour impacts, but is e.g. desired in ammunition used by police forces etc.

Rigid phase

The final phase is the rigid phase, which is initiated when the relative velocity of tail-end and the front-end of the projectile is zero. In this phase, the projectile either perforate the armour, or is defeated by the armour.

CHAPTER 3

ANALYTICAL MODEL OF PROJECTILE DEFORMATION

This project treats a narrow range of the terminal ballistic field with regards to the projectile and target materials studied. The following chapter is therefore only tested for the projectile materials; steel, aluminium and brass, and for the target materials; ARMOX 500 and Quardian 500 which both are high hardness steels specially designed for impacts. Furthermore, only cylindrical projectiles with a blunt front-end in a normal impact is treated in the models. An attempt of making it as general as possible has been made, but in a few cases this has not been achieved.

The main objectives are to describe the projectile behaviour during impact, analyse stresses and strains and determine the most effective parameters influencing the fracture or defeat of the projectile. The main focus is therefore on the projectile, but as the behaviour of the projectile is target dependent in all real cases, a sufficient amount of target parameters are included.

Two analytical models are derived in this section to obtain an understanding of the deformations and penetration capabilities of the projectile.

The analytical chapter is followed by a numerical and experimental study of the same cases, both for comparison, validation and additional findings.

3.1 Assumptions

Some general assumptions applicable throughout the entire analytical section are taken. These assumptions are listed and explained in the following.

1. The projectile and target materials are in-compressible and the density is constant in both materials. In most cases the physical assumptions and derived equations are not applicable without conservation of volume. In-compressible material is a valid assumption for most cases, especially for the metallic materials which are the only type of materials used in this study.
2. The projectile material behavior is linear elastic-plastic and stresses are strain rate independent. This assumption might be valid only when dealing with a limited range of strains where the straight line may represent the real curve which follows an exponential relation in most cases.
3. Thermal and elastic energy dissipation is neglected. In most studies the increase in temperature during impact is neglected, especially for the low and moderate impact velocities where the thermal energy is small in comparison to the plastic energy. Although, an increase in temperature often change the material properties the effects are neglected in this study for simplicity.
4. Mass conservation is applied for rigid and mushrooming phases. Although fragments may separate from the projectile during the mushrooming phase, their momentum is

included in the total equation where the study accounts for the stresses and strains in the projectile.

5. The study is applied on short projectiles although some parameters are obtained from the study of long-rod penetration. The validity of these parameters are assessed for each individual case. The field on terminal ballistics is often divided into multiple fields of study depending on both aspect ratio of the projectile, and the impact velocity. This report only deals with short projectiles in the sub-ordnance to low-ordnance velocity range.

Some further assumptions are used for some specific cases and these are described when necessary.

3.2 Retarding force the target exerts on the projectile

A large number of empirical relations and engineering models have been proposed over the years to account for the penetration depth for a given projectile/target combination in terms of impact velocity. They differ from each other by the basic assumptions concerning the retarding forces, i.e. stresses the target exert on the projectile.

For mass conservation impacts i.e. rigid projectile, no erosion, the process is governed by the projectile's deceleration a , which is caused by the retarding force the target exerts on the projectile during its penetration [Rosenberg and Dekel, 2012].

The deceleration of the projectile can be described as

$$a = \frac{dv}{dt} = \frac{dv}{dx} \frac{dx}{dt} = v \frac{dv}{dx} \quad (3.1)$$

From which the penetration increment is obtained

$$\begin{aligned} dx &= \frac{v}{a(v)} dv \\ \Rightarrow P &= \int_0^{v_0} \frac{v}{a(v)} dv \end{aligned} \quad (3.2)$$

where P is the penetration depth in the target and v_0 is the impact velocity. The only unknown quantity in this equation is the actual dependence of the deceleration on penetration velocity, $a = a(v)$. Various functional forms for $a(v)$ have been suggested over the years for different projectile/target combinations, and all of them are special cases of the general expression

$$a(v) = C + Av + Bv^2 \quad (3.3)$$

where the constants A, B and C have been determined empirically for each set of experiments. One of the most popular forms for the deceleration was suggested by Leonard Euler (1745) and the British gun engineer Benjamin Robins (1742), where they consider the deceleration as a constant.

$$a = C = \text{constant} \quad (3.4)$$

Inserting this expressions for $a(v)$ in eq. 3.2 and integrating between the boundary conditions, results in the following expressions for the final penetration depth P in terms of impact velocity v_0

$$P = \frac{v_0^2}{2C} \quad (3.5)$$

The constant deceleration C can be determined empirically for any projectile/target combination.

A more efficient way is to define the deceleration in terms of the material properties of the projectile and the target, which is the aim in this section.

A constant deceleration means that the target exerts a constant retarding force F on the projectile during the penetration. The retarding force can be expressed by the stress R_t , which the target exerts on the rod, multiplied by its cross section area πr^2 , where r is the radius of the projectile cross section. Thus for a cylindrical projectile with mass m and radius r one can write:

$$F = m a = \pi r^2 R_t = \text{constant} \quad (3.6)$$

Defining the stress R_t leads to the definition of the deceleration, retarding force and the penetration depth.

A derivation of R_t is done by the group as follows.

The following analysis is only valid for semi infinite targets. The magnitude of energy needed to penetrate the target defines exactly the force needed for penetration, where this energy is equivalent to the work done by the penetration force.

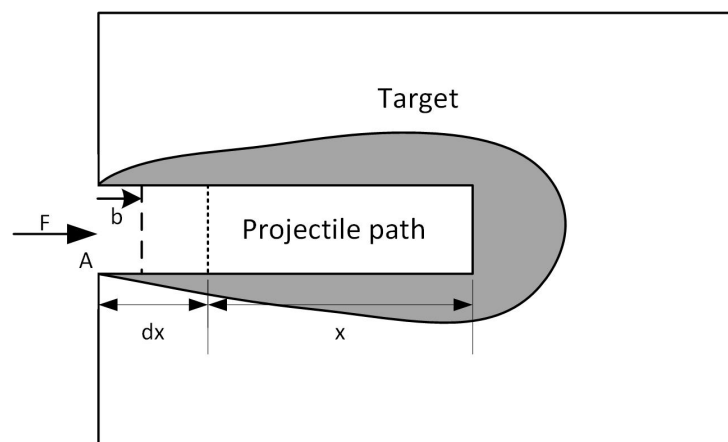


Figure 3.1: *Propagation of penetration depth in a semi infinite target.*

Figure 3.1 shows a cylindrical projectile path in the target material where x is the final depth of penetration, dx is a finite distance of the total penetration depth, b is the first step length where the force F pushes the material into the target to initiate the penetration.

This event is expected to occur as follows:

1. When F moves a distance b within the finite portion dx , it causes only elastic strains in the finite volume defined by dx .
2. The strains in the portion dx is given as

$$\varepsilon = \frac{(dx - b) - dx}{dx} = \frac{-b}{dx} \quad (3.7)$$

3. The work done by the force F is

$$dW = F b \quad (3.8)$$

4. Before the strain ε reaches the plastic region, all compression stresses are transferred to the surrounding material, the shaded area around the path in fig. 3.1, leaving the portion dx free of stress before F gets forward again.
5. The strain energy absorbed by the material through the portion $dV = A dx$ is

$$dU = dV Y_t d\varepsilon \quad (3.9)$$

where Y_t is the dynamic yield strength for the target material and dV is the finite volume which absorbs the energy.

6. For each progress of F the stresses around the path increases to yield the material and the largest plastic deformation is in the material surrounding the front of the projectile.

The work done by the external forces is equal to the strain energy, equating eqs. 3.8 and 3.9 and by dividing both sides by ε it can be found

$$F dx = -dV Y_t \frac{d\varepsilon}{\varepsilon} \quad (3.10)$$

where $F = R_{t1} A$. Integrating both sides of eq. 3.10 and noting that $\varepsilon = \frac{E}{Y_t}$ the stress needed for perforating the target material is

$$R_{t1} = Y_t \ln \left(\frac{E}{Y_t} \right) \quad (3.11)$$

This equation describes the stress needed to deform the target material by a cylindrical projectile with blunt front end. The additional stress needed to shear the deformed material during penetration is described next.

During penetration a cylindrical projectile cuts a surface equal to the circumference of a circle multiplied by the penetration depth. To obtain the work done by this shear force an elementary form of the Peach-Koehler formula is used

$$F_s = \tau b \quad (3.12)$$

where $F_s = (R_{t2} A/2 \pi r)$ is the force per unit length acts on the dislocation caused by the applied stress, R_{t2} is the applied stress, τ is the shear stress of the target material and b is a finite distance crossed by the force as can be seen in figure 3.2. This equation indicates that the distributed force per unit length on a glide dislocation is simply the product of the shear stress resolved on the slip plane in the direction of the Burgers vector by the magnitude of the Burgers vector.

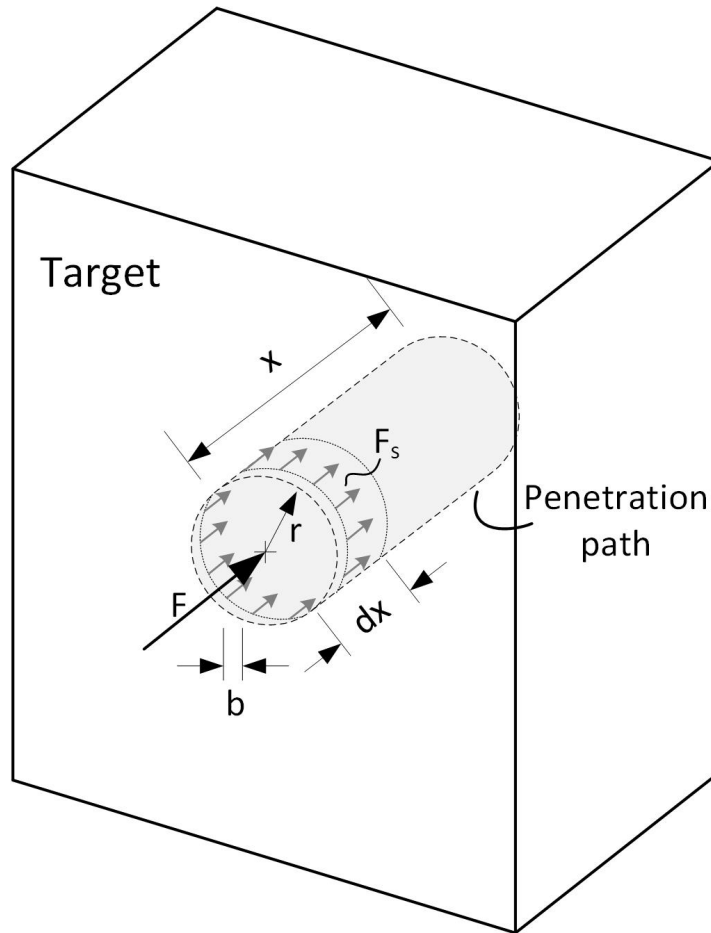


Figure 3.2: *Shear force acts on the dislocation.*

Considering the energy changes associated can be done by allowing the dislocation segment to glide all the way through the cylindrical element. The element moves in the direction of the Burgers vector, when this happens, the work done by the shear force is

$$dW_\tau = \tau b(2 \pi r dx) \quad (3.13)$$

Equivalently the work as the distributed force on the dislocation times the distance it moves in the process can be expressed. This is

$$dW_{eq} = (2 \pi r F_s)b \quad (3.14)$$

where $(2 \pi r F_s)$ is the total force acting on the dislocation segment. Equating these equivalent work effects gives

$$\tau b(2 \pi r dx) = (2 \pi r F_s)b \quad (3.15)$$

and for finite volume where $dx = r$ eq. 3.15 becomes

$$R_{t2} = 2\tau \quad (3.16)$$

which gives the stress magnitude needed for defeating the shear strength of the material for circular cross section during impact. The total resistance the target exerts on the projectile can be obtained by summation of eqs. 3.11 and 3.16 which gives

$$R_t = Y_t \ln \left(\frac{E}{Y_t} \right) + 2\tau \quad (3.17)$$

In the case of normal impact where the external stress is normal stress, the shear stress is taken as $\tau = \frac{1}{2}Y_t$.

A proper formula describing the target resistance to penetration has been one of the main objectives for researchers and many experiments were done for this purpose. Simulations of [Rosenberg and Dekel, 2012] were aimed at finding a general relation between R_t and the relevant parameters of the target Y_t , E , for rods with different nose shapes. The simulation resulted in the following expression for R_t

$$\frac{R_t}{Y_t} = 1.1 \ln \left(\frac{E}{Y_t} \right) + k \quad (3.18)$$

where Y_t and E are the dynamic strength and Young's modulus of the target material and k is a constant that accounts for the projectile nose shape. A spherical, conical and ogive nose shape were used in this simulation where the values of k are -0.2 , -0.93 , -1.15 respectively [Rosenberg and Dekel, 2012].

It is clear that this equation is very similar to equation 3.17. There are some advantages in eq. 3.17 over eq. 3.18.

1. The shear stress is accounted for in eq. 3.17 where it is absent in eq. 3.18.
2. Eq. 3.18 gives one constant number to account for the nose shape, and ignores the blunted projectiles, actually the nose shapes from the same type e.g. the conical ones can differ by the length and sharpness and thereby by the penetration capability. Since eq. 3.17 has no terms related to the projectile material or shape, it is applicable for any type of nose shapes, where the entrance face can be handled by using a variable cross section while neglecting the shear term. For the remaining part of the projectile, a constant cross section and implementation of the shear term is used, as is shown.
3. The fitting number k in eq. 3.18 is an empirical number and it might be target or projectile properties dependent.

In spite of the above differences between the two equation, the results obtained by them are very close as will be shown later.

3.2.1 Rigid projectiles

For high strength projectiles and moderate impact velocities where the deformations of the projectile are negligible, the cross sectional area of the projectile is considered as constant during the impact. A numerical simulation in [Rosenberg and Dekel, 2012] of a rigid rod with a spherical nose impacting an aluminium target of 0,42 GPa in dynamic strength is used for validating eq. 3.17. Substituting $E = 69$ GPa in eq. 3.17 yields $R_t = 2,5$ GPa, where the resistance force exerted on the rod is $F = R_t A$, where A is the cross sectional area. During the entrance face the cross section changes between 0 and πr^2 where the velocity changes between v_0 and v_1 , during this phase the resistance force changes as the cross sectional area changes. The entrance phase ends with projectile velocity v_1 and the penetration phase starts with constant resistance force and thereby constant deceleration as the cross sectional area is a constant.

During the penetration phase, where the cross sectional area is constant and the resistance force is constant, the projectile velocity changes between v_1 and 0. Substituting in eq. 3.2 gives the total penetration in terms of the impact velocity. Figure 3.3 shows the good correlation between the analytical solution and the numerical simulation which is also in good correlation with eq. 3.18.

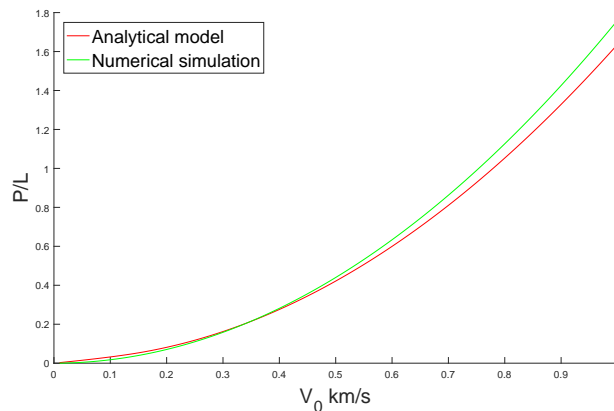


Figure 3.3: *Penetration of rigid spherical nose shaped rod of aluminum target.*

For another validation of eq. 3.17, a comparison with a simulation study for a rigid sphere impacting a semi infinite target is performed. A simulation of steel spheres impacting an aluminum target with dynamic yield strength $Y_t = 0,4$ GPa [Rosenberg and Dekel, 2012] against results obtained by eq. 3.17 are plotted in figure 3.4.

It is seen that the analytical solution is below the numerical simulation, where the two curves start to approach each other for impact velocities higher than 1 km/s. Another comparison with experimental results is done for further investigation of the model describing the resistance stress in eq. 3.17.

Spherical steel projectiles of 10 mm in diameter are shot on a steel armor plate with 1,47 GPa in dynamic strength, 12 mm thickness and Young's modulus of 207 GPa. Six shots

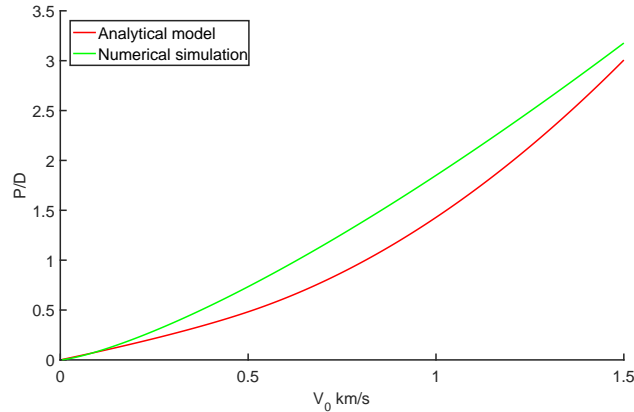


Figure 3.4: *Penetration of rigid spheres of aluminium target.*

at six different impact velocities are done, the maximum impact velocity is 503 m/s which is due to the limitation of the gas cannon used in the lab. A plot of the results and the analytical model can be seen in figure 3.5. The maximum penetration depth in these tests is 1,84 mm which is way less than half the target thickness, furthermore the target dimensions are 400×400 mm, so the assumption of the plate as a semi infinite target is valid [Rosenberg and Dekel, 2012].

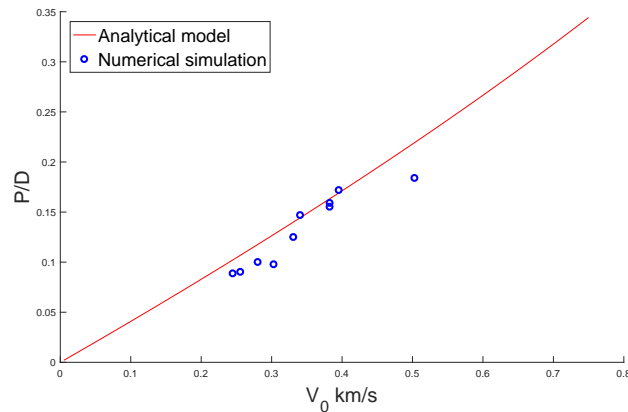


Figure 3.5: *Penetration of rigid spheres of a steel target, experiment against analysis.*

It is seen that all the points are located on the curve or slightly lower. For low impact velocities the deformations in these hard spheres are neglected, where the loss in energy can be the reason why most the points are lower than the analytical curve where the spheres are assumed as a rigid projectile. Thus the model described in eq. 3.17 is expected to yield good results in the moderate impact velocities where the penetration crater has the same diameter as the projectile i.e no cavitation. For higher impact velocities it is still able to describe the energy needed to penetrate the material, which is only target material dependent.

3.2.2 Non rigid projectiles

The section above shows the relation between the penetration depth and the resistance stress of the target material when the projectile is considered as rigid and plastic deformation is neglected. In most cases this assumption is not valid where the projectile could be non rigid or/and the impact velocity could be high enough to cause significant plastic strains in the projectile, the deformations in its front cause a bigger cross sectional area and thereby a bigger resistance force F leading to less penetration depth.

Cylindrical projectiles.

For a better investigation of the deformation effects, the cylindrical projectiles are studied since detecting mushrooming and changes in cross section is relatively simple.

The target resists the penetration of the projectile with force $F = R_t A$, where A is the cross sectional area of the projectile front, this causes a deceleration a leading the projectile to rest after time t . The moment the projectile hits the target an elastic stress wave starts propagating from the impact face towards the projectile tail, at the same time the projectile is penetrating the target, this wave is followed by a plastic wave which causes a plastic deformation in the projectile that increases the cross sectional area to $A_i > A$ for every portion crossed by this plastic wave.

Experiments in [Rosenberg and Dekel, 2012] show that the actual sequence of impact events with increasing impact velocities, figure 3.6, is as follows:

1. at low impact velocities the rod penetrates as a rigid body up to a certain threshold velocity v_d which corresponds to the onset of its deformation.
2. for impact velocities higher than v_d the rod deforms with no mass loss, resulting in reduced penetration with increasing impact velocities.
3. at a certain impact velocity rod erosion sets in, and for higher impact velocities the penetration depths are increasing again.

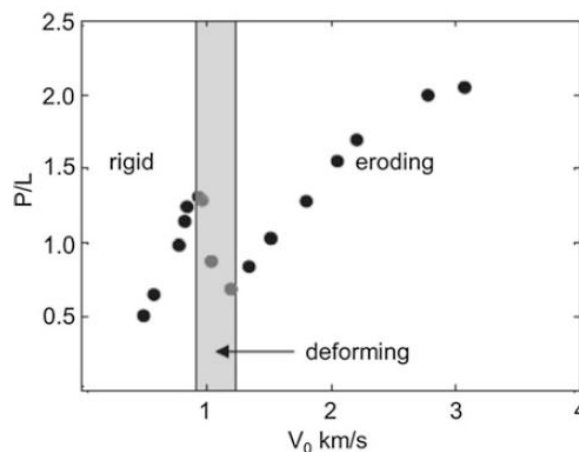


Figure 3.6: Penetration of rigid spherical nosed rod of an aluminum target, [Rosenberg and Dekel, 2012, pg. 115].

3.2.3 Approach for deformation threshold velocity v_d

To estimate the impact velocity where the projectile starts deforming, the forces acting on the projectile nose must be investigated when penetration starts. As discussed before, the resistance R_t can be computed using eq. 3.17. When the projectile starts deforming, the stresses behind the interface reaches the dynamic yield strength of the projectile material Y_D , furthermore, the inertia of the target material $\frac{1}{2}\rho_t v^2$ must be accounted for where the energy consumed by this factor becomes more significant as the impact velocity becomes higher.

The plastic deformation in the front of a projectile occurs when stresses become equal to the dynamic yield strength of the projectile Y_D . This means, when the front nose velocity is decreased to $\dot{x} < v_d$, then the change in kinetic energy between the rear end and the front end of the projectile equals the stresses produced in the front

$$\begin{aligned} \frac{1}{2}\rho_p (v_d^2 - \dot{x}^2) &= Y_D \\ \Rightarrow \dot{x}^2 &= v_d^2 - \frac{2Y_D}{\rho_p} \end{aligned} \quad (3.19)$$

When penetration starts, the resistance of the target becomes the sum of R_t and the inertia term $\frac{1}{2}\rho_t \dot{x}^2$.

Assuming a constant deceleration

$$a = \frac{dv}{dt} = \frac{dv}{dx} \frac{dx}{dt} = v \frac{dv}{dx}$$

and when the front velocity changes from v_d to \dot{x} the penetration changes from zero to x , and $m_p a =$ 'total resistance' $\cdot A$, where m_p and A are the mass and cross sectional area of the projectile, respectively. Arranging the previous terms leads to the equation

$$\int_{v_d}^{\dot{x}} v_d dv = -\frac{A}{m_p} \int_0^x \left(R_t + \frac{1}{2}\rho_t \dot{x}^2 \right) dx \quad (3.20)$$

where $\frac{A}{m_p} x = \frac{1}{\rho_p}$, the later equation gives

$$\frac{1}{2}(\dot{x}^2 - v_d^2)\rho_p = - \left(R_t + \frac{1}{2}\rho_t \dot{x}^2 \right) \quad (3.21)$$

Substituting eq. 3.19 into the later equation leads to the critical impact velocity for the deformed projectile

$$v_d = \sqrt{\frac{2}{\rho_t} \left(Y_D \frac{\rho_p + \rho_t}{\rho_p} - R_t \right)} \quad (3.22)$$

From eq. 3.22 it can be seen that if $R_t > Y_D \frac{\rho_p + \rho_t}{\rho_p}$ the projectile deforms before it is penetrating.

The inertia resistance.

There is another resistance force the target exerts on the projectile during impact which is the inertia of the target material $\frac{1}{2}\rho_t\dot{x}^2$, where ρ_t is the density of the target material and \dot{x} is the penetration velocity. For a penetration depth P the total energy consumed by the resistance R_t is $E_R = R_t A P$, and the energy consumed by the inertia is $E_I = \frac{1}{2}\rho_t\dot{x}_m^2 A P$, where \dot{x}_m is the mean penetration velocity. An assumption to define the critical impact velocity at which the inertia term must be accounted for can be $E_I \geq 1\% E_R$ and this leads to

$$v_I = \frac{1}{100} \sqrt{\frac{8R_t}{\rho_t}} \quad (3.23)$$

where v_I is the critical impact velocity for including the inertia term in the resistance forces the target exerts on the projectile during penetration. It is seen that this critical velocity is a target material parameter, for the steel armour plate used in the experiments (sec. 5.2), with $R_t = 8$ GPa, the critical inertia velocity is 0,9 km/s.

3.3 Analytical model for deformed projectiles

A model derived by the group for predicting stresses, deformations in the projectile and penetration depth is discussed in this section.

As discussed earlier, the projectile front deforms to a cross sectional area A , which is bigger than the initial one A_0 , when the impact velocity exceeds the deformation critical velocity v_d . This leads to less penetration and yields a state of stress in the projectile exceeding the dynamic yield strength causing the plastic deformation. In this study the energy loss by increase of temperature and elastic strain is neglected, thus the total kinetic energy carried by the projectile is only consumed by the penetration and the plastic deformation in the projectile.

3.3.1 Main assumptions

When impact starts and the projectile front face reaches the target surface, the projectile starts losing its kinetic energy k in two directions, penetration of the target and plastic deformation in the projectile itself. The main objective in this section is to estimate the magnitude of energy dissipated in each direction, this estimation allows for dividing the problem into two independent problems as explained below.

From equations of motion it is known that if an object 1 with density ρ_1 and moving with initial speed u_1 , hits an object 2 with density ρ_2 which is in rest $u_2 = 0$, and the two objects cohere together without any deformations or energy loss, and continue after impact at mutual speed u , the total energy in the system is the kinetic energy for object

1 which is distributed among the two objects after impact

$$k_1 = \frac{1}{2}m_1u^2$$

$$k_2 = \frac{1}{2}m_2u^2$$

If the two objects have the same volume, then the energy terms after impact can be written as

$$k_1 = \frac{1}{2}\rho_1u^2$$

$$k_2 = \frac{1}{2}\rho_2u^2$$

The total kinetic energy is $k = k_1 + k_2$ then it can be determined

$$k_1 = \frac{\rho_1}{\rho_1 + \rho_2} \frac{1}{2}\rho_1 u_1^2 = \xi \frac{1}{2}\rho_1 u_1^2 = \xi k \quad (3.24)$$

$$k_2 = (1 - \xi)\frac{1}{2}\rho_1 u_1^2 \quad (3.25)$$

It is seen that the total energy is distributed between the objects based on their densities, the higher the density the bigger the energy gained by impact.

It is assumed that after a finite time dt of the impact process, when the two materials faces meet and just before deformations start, the projectile loses a small part of its kinetic energy, this energy reduction is distributed between the projectile and the target interaction faces in the same manner as eq. 3.25.

The projectile velocity is

$$v = a t + v_0 \quad (3.26)$$

where v_0 is the initial impact velocity, $a = \frac{-R_t A_0}{m}$ is the deceleration of the projectile which is considered a constant during the impact process, and A_0 is the initial cross sectional area of the projectile. The kinetic energy of the projectile is given as

$$k = \frac{1}{2}m v^2 \quad (3.27)$$

where m is the projectile's mass. The change in kinetic energy over the time is

$$\frac{dk}{dt} = m v a \quad (3.28)$$

When impact starts, a stress wave propagates in the projectile and moves towards its rear end at wave velocity c , this wave is a wave of deformations caused by the energy distributed in the projectile. The deformed volume over the time is

$$V = c A_0 t \quad (3.29)$$

and the change in this volume with respect to time is

$$\frac{dV}{dt} = c A_0 \quad (3.30)$$

As mentioned before, the energy absorbed by the projectile material over the time is a fraction of the total change in energy and given as

$$k_1 = \zeta \frac{dk}{dt} = \zeta m v a \quad (3.31)$$

where $\zeta = \frac{\rho_p}{\rho_p + \rho_t}$ is the density ratio and p, t denote the projectile and the target, respectively. When t is in the neighborhood of zero, then $v \cong v_0$ and the energy distributed in one unit volume of the projectile over the time at when impact starts is

$$k_u = \left(\frac{k_1}{dV/dt} \right)_{t \rightarrow 0} = \zeta \frac{m v_0 a}{A_0 c} \quad (3.32)$$

This equation describes the energy density at the front face of the projectile when impact starts for velocity v_0 , where the target material consumes the rest of the energy lost. This energy density is only distributed in infinitesimal volume, thus just a slice of the projectile front can have this energy density, the thickness of this slice is proportional to the ratio between the impact velocity and the wave velocity, which defines the volume deformed in the projectile before penetration starts.

The above assumption leads to the deformation magnitude in the projectile front face as the impact starts. The deformation velocity depends on the strain rate and it may not reach its maximum value before the penetration starts, however it is assumed that the deformation of the projectile front completes before any penetration, which is an acceptable assumption for impact velocities ($\leq c$) and/or for the high resistance targets. When R_t is small and the penetration is faster than the deformation, this assumption is then only used for obtaining the stress at the projectile front.

3.3.2 Derivation of the model equations

Assuming that the projectile material is linear elastic-plastic

$$\sigma_1 = Y_D + E_w \varepsilon_p \quad (3.33)$$

where Y_D is the dynamic yield strength, ε_p is the longitudinal plastic true strain of the projectile material, σ_1 is the stress at the material for plastic strain ε_p , and $E_w = c^2 \rho_p$ is the linear strain hardening modulus. The true strain can be written as

$$\varepsilon_p = \ln \frac{x_f}{x_0} \quad (3.34)$$

where x_f and x_0 are the final and initial length of the portion crossed by the stress wave. The kinetic energy is distributed in dV and converted into plastic energy

$$u_p = \int_{\varepsilon} \sigma_1 d\varepsilon = \frac{1}{2} \frac{\sigma_1^2}{E_w} \quad (3.35)$$

where u_p is the strain energy density per unit volume, and the stress can be obtained by equating eqs. 3.32 and 3.35

$$\frac{1}{2} \frac{\sigma_1^2}{E_w} = \zeta \frac{m v_0 a}{A_0 c} \quad (3.36)$$

and the maximum stress at the front end of the projectile can be found as

$$\sigma_1 = \sqrt{2 \zeta \rho_p R_t v_0 c} \quad (3.37)$$

It can be seen from eq. 3.37 that the target properties, the projectile density and the linear strain hardening modulus give the maximum stresses at the projectile's front for a specific impact velocity.

The material is assumed non-compressible thus by conservation of volume the deformed cross sectional area can be found as

$$A x_f = A_0 x_0 \Rightarrow A = A_0 e^{-\varepsilon_p} \quad (3.38)$$

where ε_p is obtained from eq. 3.33.

It can be seen from eq. 3.38 that for penetration as a rigid without deformations in the cross section, $e^{-\varepsilon_p}$ must be equal to one, thus $\sigma_1 = Y_D$ and eq. 3.37 yields

$$v_d = \frac{Y_D^2}{2 \zeta \rho_p R_t c} \quad (3.39)$$

which is the critical impact velocity for deformations in a cylindrical projectile, this critical velocity differs from the definition found in eq. 3.22, where it has only one term. Although the target inertia term is not included in eq. 3.39 the target density is included.

Eq. 3.39 shows relatively low deformation velocity threshold which is the case for the blunt projectile as the force acting at its nose is much bigger than the conic or ogive nosed projectile, a different and higher threshold can be derived for the other types of nose shapes based on the change of the resistance force with respect to the change in cross section of the nose.

Deformations in the projectile

The rigid projectile with cross sectional area A_0 is called, by the group, an equivalent projectile of the deformed one if:

1. It has the same initial length and thus the same volume as the deformed projectile.
2. It has the same density and material properties.
3. It penetrates the same target as a rigid and the penetration depth is equal to the penetration depth caused by the deformed projectile.

Based on these assumptions a relation between velocities and cross sections can be found as

$$\frac{v_r^2}{v_0^2} = \frac{A}{A_0} \quad (3.40)$$

where v_0 , A and, v_r , A_0 are the impact velocity and cross sectional area for the deformed projectile and its equivalent rigid, respectively.

The deceleration of penetration is assumed to be constant in this study and thereby the penetration depth for the deformed projectile can be given as

$$P = \frac{m v_0^2}{2R_t A} \quad (3.41)$$

when the equivalent rigid projectile penetrates the target for the same depth its impact velocity is v_r where

$$v_r = v_0 \sqrt{\frac{A_0}{A}} \quad (3.42)$$

and the energy used in deformation is

$$k_d = \frac{1}{2} m (v_0^2 - v_r^2) = \frac{1}{2} m v_0^2 \left(1 - \frac{A_0}{A}\right) \quad (3.43)$$

so the other part of the total kinetic energy is used for penetration

$$k_p = k - k_d = \frac{1}{2} m v_0^2 \frac{A_0}{A} \quad (3.44)$$

Note that the assumption made for the first iteration and the energy loss is only used to obtain the stress magnitude at the front face of the projectile, thus the maximum strain and penetration depth can be obtained.

During the impact time, the plastic stress wave travels towards the rear end of the projectile leaving the material in plastic state of strain as long as the stresses are higher than the dynamic yield strength Y_D , where the highest stresses occur at the first cross section and the stresses magnitude decreases as the wave propagates resulting in a gradual decrease in the deformed cross sectional areas until it becomes equal to A_0 after some distance L_p from the front end.

The energy consumed in deforming the projectile which is defined in eq. 3.43 is distributed over the deformed volume in a parabolic manner since the kinetic energy is a second order function of the velocity. As k_d and the maximum stress σ_1 are known, it is possible to assume a projectile with impact velocity $v_d = \sqrt{2 k_d/m}$ hitting a rigid target and all its kinetic energy turns to plastic deformation

$$dk_d = \frac{1}{2} m (v_d^2(i+1) - v_d^2(i)) \quad (3.45)$$

where i is the iteration number defining the velocity of the projectile at time $T(i)$

$$v_d(i + 1) = \frac{-Y_D A_0}{m} t + v_d(i) \quad (3.46)$$

Assuming that the stresses don't vanish before the rear end of the projectile, while keeping in mind that the deformation stops as the stresses become equal or less than the dynamic yield strength Y_D , this leads to a parabolic stress distribution between max stress σ_1 at the front to zero stress at the rear end passing by Y_D at some distance L_p from the front end of the projectile. The equation describing the stresses can be found by the three points mentioned above, where L_p for short projectiles is approximated as

$$L_p = L_0 \left(1 - \sqrt{\frac{Y_D}{\sigma_1}} \right) \quad (3.47)$$

Since the maximum cross section area A is known, the change in cross section is proportional to the stress distribution, using eq. 3.47 it is found that the change in cross section area is

$$A(x) = \frac{A - A_0}{L_p^2} x^2 + A_0 \quad (3.48)$$

where x is the distance from the rear end towards the front end.

The stress distribution over the projectile is shown in figure 3.7 with the mushrooming shape after impact at initial velocity of 350 m/s for a steel projectile. The dynamic yield strength used in the model for the steel projectile is the one derived in sec. 3.5 which is proportional to the impact velocity, the other material parameters are listed in table 5.1.

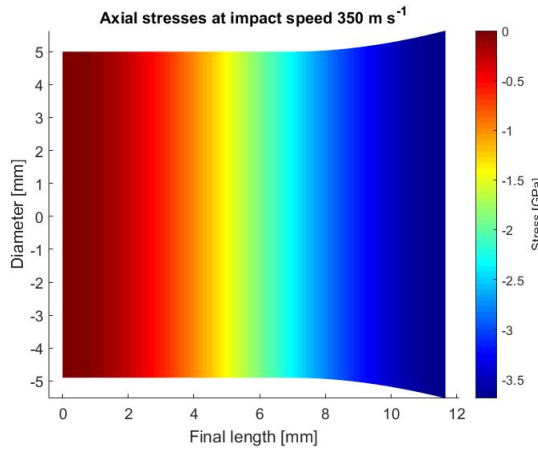


Figure 3.7: *Stress distribution and deformations of a short cylindrical projectile.*

The figure shows the maximum compression stress at the front where it is zero at the rear end as expected.

The shortening in the projectile length can be obtained by subtracting the distance the front end crosses from the distance the rear end crosses during the impact as it is shown in figure 3.8.

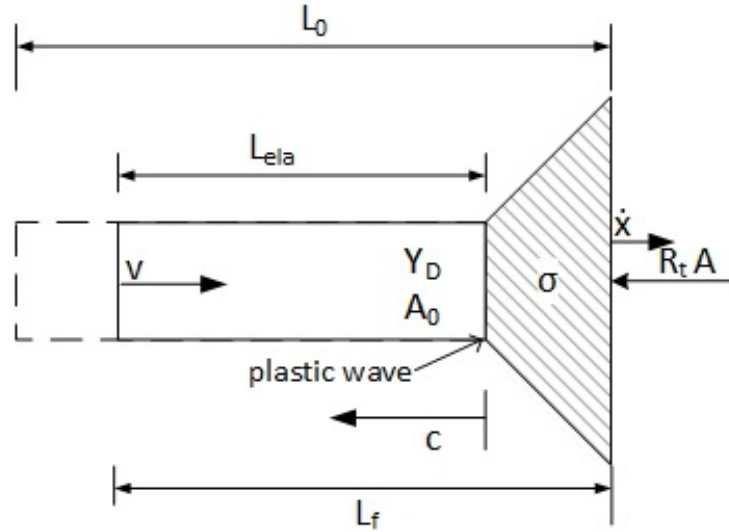


Figure 3.8: *Plastic wave propagation in deformed projectile.*

During impact the rear end decelerates by the force $Y_D A_0$ acting at the plastic wave interface where the equation of motion for the rear part of the projectile is given as

$$v = \frac{-Y_D A_0}{m} t + v_0 \quad (3.49)$$

and the total distance the rear end crosses while the projectile velocity v changes from v_0 to zero is

$$x_r = \frac{m v_0^2}{2Y_D A_0} \quad (3.50)$$

The front part moves a distance equal to the penetration depth which is given by eq. 3.41, and the final length of the projectile is

$$L_f = L_0 - (x_r - P) \quad (3.51)$$

The above analysis shows that the stresses, final length, strains, deformations and even fracture can be found through the maximum stresses at the front end eq. 3.37 or even by finding the final length eq. 3.51 and the longitudinal shortening can be used to obtain the maximum strains and thereby stresses at the front.

3.3.3 Verification of the model

Within the range of the relatively low impact velocities, seen in chapter 6, the model yields a good correlation with the experimental data.

Another comparison is made, based on experimental data obtained in [Włodarczyk et al., 2012] for three different impact velocities. The dynamic yield strength for the projectile material is obtained from [Taylor, 1947], as seen in section 3.5. The projectile is a uniform chromium-nickel steel rod of the initial dimensions, length $L = 0,0127$ m and the diameter $D_0 = 0,00864$ m. Mechanical parameters of the steel are as follows: the density $\rho_p = 7800$ kg/m³, and the strain-hardening modulus $E_w = 3500$ MPa. The target in the experiment is assumed as a rigid, which is not the case for the model, although it has a relatively high resistance of $R_t = 8$ GPa.

The results are listed in table 3.1.

Impact velocity v_0 [m/s]	D_1/D_0	L_f/L_0	
196	1,16	0,93	Model
	1,19	0,94	Experiment
266	1,24	0,87	Model
	1,30	0,90	Experiment
300	1,28	0,83	Model
	1,36	0,88	Experiment

Table 3.1: Results obtained by the model and experimentally in [Włodarczyk et al., 2012] for a short cylindrical steel projectile.

It is seen from the results in table 3.1 that the model predicts lower values for the front end diameter, which could be due to cracks and local fractures in the projectile after impact which allows a more free expansion and thereby increase the measured area cross section. The normalized final length is also lower than the experimental results. An explanation of this is not available, but it is noted that the eq. 3.51, which is used in obtaining the final length, shows a very good correlation with the in-house experiments as treated in chapter 6.

During this study it is found that some parameters have a significant affect on the results, the dynamic yield strength and the linear strain hardening modulus of the projectile material, besides the resistance force of the target, are the most important parameters as the aboved derived model is very sensitive to any of them. An analytical method derived in [Hawkyard et al., 1968] is used to obtain the dynamic yield strength of the projectile, the method is only valid for impact velocities lower than the plastic wave velocity c which makes it limited and maybe not even robust for all cases. The method shows an over estimation of the dynamic yield strength Y_D in some cases although the results in general have a good correlation with other studies and experimental data.

The correct way of obtaining the dynamic yield strength of the materil is to perform a

Split-Hopkinson-Bar-Test. Another important parameter is the linear strain hardening modulus E_w for the projectile material, and for more accurate results the material tests, seen in appendix C, has to be better.

3.4 Modified model by den Reijer

The following section is a summation of the model by den Reijer, [den Reijer, 1991], and the modifications made for implementation of the model on the present study. This means, that the necessary equations are presented along with the needed figures necessary for understanding the model in its core. Additional explanation is found in the full description of the model as seen in appendix A. It is sought to make the report section and the appendix section readable separately, but this induces some repetition.

The model was developed by P. C. den Reijer during his Ph.D.-studies, [den Reijer, 1991]. The model treats the impact of a blunted cylinder on a ceramic face with an aluminium back plate, and is included in this project as it models the three main phases of projectile impact, i.e the mass erosion phase, the mushrooming phase and finally the rigid phase, among others. The study by den Reijer also contains a comprehensive target modelling part, with interactions to the projectile modelling, all compiled in a piece of software named ALARM (Analytical Lightweight Armour Response Model). This part of the study is omitted, with the following limitations of the full den Reijer model this may prompt.

The model is hereafter modified by the project group for implementation on a direct impact on a steel plate, and to account for complications experienced during implementation of the model.

It is shown by Wilkins, [Wilkins et al., 1968], that a great amount of the energy loss from the projectile in the initial stages of the impact is consumed by erosion of the projectile, and not absorbed by the armour or plastic deformation/mushrooming of the projectile, why it is deemed necessary to include this in the model. Erosion, as defined in sec. 2.2.2, means a separation of material which influences and decreases the momentum of the projectile and thereby reduces its armour perforation capabilities.

When the erosion of the projectile ends, the remaining energy in the projectile is i.a. deposited as plastic deformation or mushrooming of the projectile or penetration of the target, why this is included in the model as well.

Armour piercing projectiles are often made of tungsten or a similar high hardness material. These materials are distinctive by their usual brittle nature. This probably means, that it would be unjustified to model their plastic deformation as mushrooming, as it would more likely happen in chunks. The model of den Reijer, and thereby the implementation of plastic deformation as mushrooming, is therefore applicable for ball projectiles, i.e. usually of lead, and fragment simulating projectiles (FSP), i.e. projectiles that behaves like fragment from e.g. an IED, which are distinctive for their blunt impact face. This is similar to the cylindrical projectiles the group has used during the experimental work.

3.4.1 Assumptions and simplifications

The main concern of applying the model on the present case is, that the model originally is developed for a projectile striking a ceramic experiencing dwelling, whereafter the projectile starts penetration of the comminuted ceramics until it reaches the backplate.

The assumptions taken for applying the model on a direct projectile-against-backplate impact are;

Assumption 1: The dwelling phase, in which the ceramic fractures, and the projectile is losing mass and velocity without penetrating the ceramic is disregarded in this implementation as a similar phenomena is not observed for the present case, i.e. impact on a steel plate.

Assumption 2: The penetration phase of the projectile through the comminuted ceramic is kept. During this penetration a resistance force from the ceramic applies on the projectile. A similar resistance force is determined for penetration of a metallic back-plate, sec. 3.2.

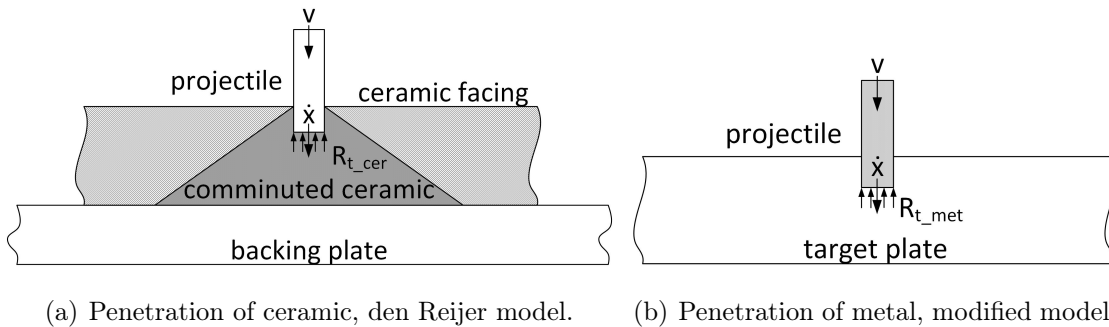


Figure 3.9: *Penetration of ceramic in den Reijer [1991] model, and the penetration of the metallic back-plate in the implementation.*

Assumption 3: The projectile is simulated as a blunt cylinder, and is assumed to not break into large fragments during impact. As previously mentioned, erosion of the projectile is permitted, [den Reijer, 1991]. The projectile material is furthermore assumed to behave linear elastic plastic and incompressible.

Assumption 4: As the model of den Reijer originally is developed for impact on ceramics, the projectile experience a set time of dwelling, depends on the thickness, while the fracture cone develops in the ceramic. This means, that the initial penetration velocity of the projectile is $\dot{x}_0 = 0$.

This is not the case for impact on metallic targets, which are researched in the present study. An approximation of the initial penetration velocity is made in sec. 3.5 regarding the implementation of the present model.

3.4.2 Projectile model

The projectile response when impacting the armour is described in three phases. A phase where the projectile undergoes mass erosion, i.e. the projectile front disintegrates. This is followed by a phase in which the projectile deforms to a mushroom-like shape which is a transition stage between the mass erosion phase and the last phase in which the projectile is rigid and defeats or is defeated by the armour.

Erosion phase:

At a high velocity, a ductile material striking an armour plate spatters or flow out parallel to the armour surface in an erosion mechanism implying that the material physically separates from the projectile and therefore no longer contributes to the momentum of the projectile, [Florence and Ahrens, 1967]. In fact, as the projectile to a certain degree is brittle this may happen in chunks but at the time of developing of the model, the physics for this were not developed and the projectile erosion is therefore governed by the plastic flow, [den Reijer, 1991]. This is adopted in this present work, and shown in figure 3.10.

The governing equations for the erosion phase are derived using the continuity equation, momentum fluxes between the different control volumes shown in figure 3.10 and force equilibrium.

The deceleration of the tail end of the projectile, while the front end is eroding, is governed by Newton II and the dynamic yield strength of the material as

$$\frac{dv}{dt} = -\frac{Y_D}{\rho_p L} \quad (3.52)$$

where L is the present length of the projectile, Y_D is the dynamic yield strength and ρ_p is the density of the projectile material.

The rate of erosion, or the change in length of the projectile, is dependent on the relative velocity of the plastic wave in the material compared to the tail-end of the projectile.

$$\frac{dL}{dt} = -c = -(v - \dot{x}) \quad (3.53)$$

where c is the relative plastic wave speed and v and \dot{x} are the velocities of the tail- and front-end respectively. This is also the stop condition for the erosion phase. As long as the relative velocity of the tail-end is larger than the front-end, by the plastic wave speed, erosion takes place and the plastic wave is 'stationary'.

The penetration velocity of the projectile is approximately constant during the erosion phase. This is consistent with long-rod penetration, [Tate, 1967], [Rosenberg and Dekel, 2012], and used for the relatively short projectiles in this project.

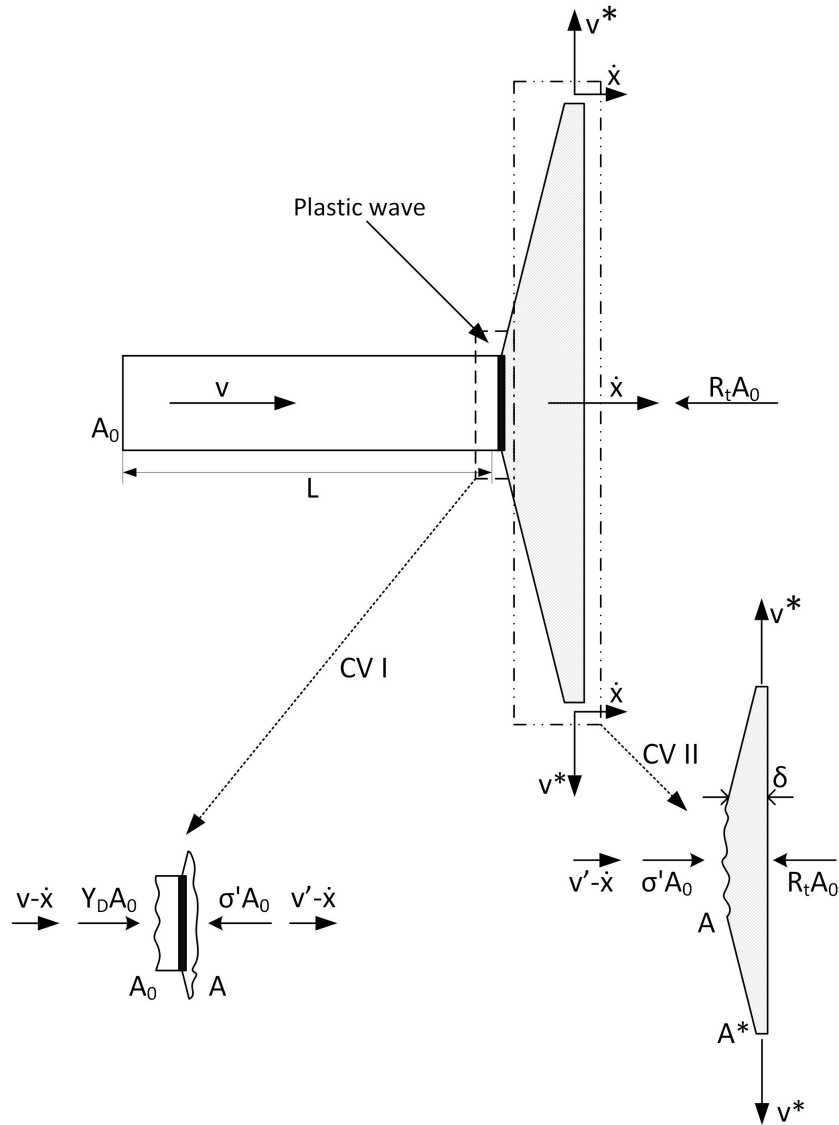


Figure 3.10: *Erosion phase and governing parameters. The control volumes, CV I and CV II, are used in the derivation of the governing equations. From den Reijer [1991].*

Mushrooming phase:

In this phase, the relative velocity of the projectile, $v - \dot{x}$, has fallen below the hydrodynamic transition velocity, i.e the velocity of the plastic wave u_{plas} , meaning the relative displacement between the tail-end of the projectile and the interface is accommodated by plastic deformation of the projectile known as mushrooming. The velocity is still higher than the critical rigid velocity though, so the projectile is in a transition between erosion and rigid state in which it deforms with no mass loss, [Lou et al., 2014]. The plastic wave moves towards the tail-end of the projectile resulting in plastic deformation of the projectile material it passes. The velocity of the tail-end is noted v , while the deformed mushroomed section has the velocity \dot{x} . The situation is sketched in figure 3.11.

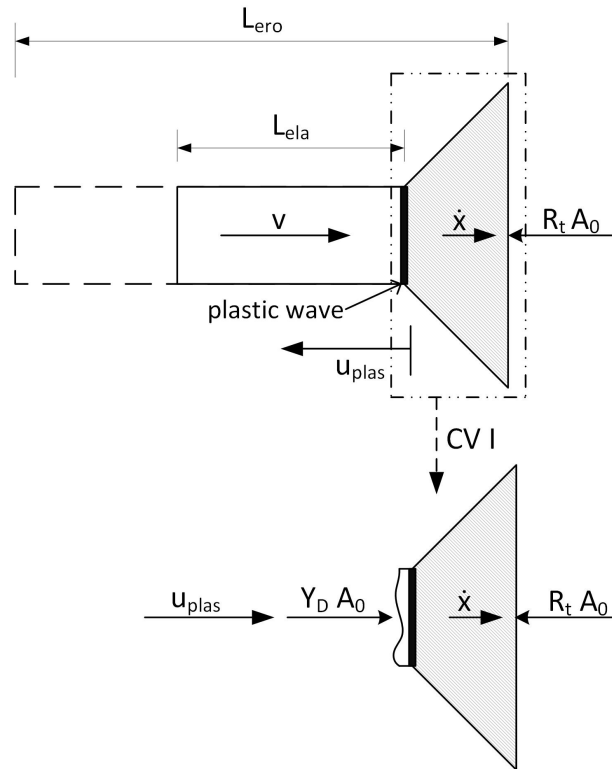


Figure 3.11: *Mushrooming phase and governing parameters. From den Reijer [1991].*

The derivation of the governing equations are performed based on the change of momentum in CV I. The deceleration of the tail-end of the projectile continues to be governed by the dynamic yield strength, and is therefore identical to eq. 3.52. However, the derived equation for the deceleration of the mushroomed front-end of the projectile has turned out to be unusable without tuning parameters. It simply yields a far to large deceleration, and this is discussed in appendix A. Modifications of the model by considering change in momentum and equating this to the external forces have all been unsuccessful as it yields a model with a bad fit, i.e. 3-4 mm off which is not satisfying.

A modification, or a fit, of the interface deceleration has been made, which gives a sufficient correlation between model and experiments as seen in chapter 6. The fit is based on the earliest of the assumptions for deceleration during penetration of a target by Euler and Robins, as described in section 3.2. This assumption is used for the penetration velocity, and the general equation of motion for constant deceleration is applied. Furthermore, the tail-end carries a momentum that exerts a force on the front end of the projectile, which tries to accelerate the front-end. Finally, the tail-end is still subjected to the retarding due to the dynamic yield strength of the projectile material as used in the erosion phase. This yields the following model-fit for the deceleration of the projectile front-end.

$$\ddot{x} = \frac{\dot{x}^2 - \dot{x}_0^2}{2P} - \frac{1}{2}\rho_p v^2 \frac{A_0}{m_{ero}} + \frac{Y_D}{\rho_p L_{ela}} \quad (3.54)$$

where P is the penetration depth into the target as seen in eq. 3.41. This term includes

the resistance of the target plate R_t and is repeated here.

$$P = \frac{m_0 v_0^2}{2 R_t A}$$

Non-physical fits can also be employed, and good correlation between these fits and experimental findings have been found. But, all of these are unjustifiable, and therefore disregarded.

Hereby is the deceleration of the projectile front end/interface described.

The final part of the mushrooming phase is to determine the rate of change in length of the elastic part of the projectile, as the plastic wave propagates through the cylinder. As the relative velocity is now sufficiently low, the rate of plastic deformation of the elastic length of the projectile is governed by the velocity of the plastic wave, as it is no longer considered 'stationary'

$$\frac{d}{dt} L_{ela} = -u_{plas} \tag{3.55}$$

and u_{plas} is the plastic wave speed in the material.

Rigid-body phase:

In the final phase of the projectile penetration, the projectile behaves as a rigid-body. This phase begins when the velocity, v , of remaining elastic section of the projectile is equal to the velocity, \dot{x} , of the mushroom deformed part of the projectile.

As the projectile does not lose any mass during the above-described mushroom-phase, the mass of the projectile is equivalent to the mass of the projectile just after the erosion phase, $M_p = \rho_p A_0 L_{ero}$. The deceleration of the remainder of the projectile, now assumed completely rigid, is therefore given from Newton II as

$$\ddot{x} = \frac{R_t}{\rho_p L_{ero}} \tag{3.56}$$

which concludes the projectile penetration as developed by [den Reijer, 1991] and modified of need.

See appendix A for additional explanations.

3.5 Implementation of model on present study

The following section treats the implementation of the models on the present study in this project. This includes determining the necessary projectile and target parameters for the combination of chosen projectile materials (steel, aluminium and brass) and the target plate of Quardian 500 steel. In this section, it concerns the determination of the dynamic yield strength of the projectile material, and the initial penetration velocity of the projectile into the target. Both empirical approaches, and analytical approaches are presented. Parameters based mostly on material tests etc. are presented later in the experimental chapter 5. In chapter 6, a comparison of models and experiments is found.

Projectile dynamic yield strength.

The dynamic yield strength of the projectile material can be determined through various of experiment and/or approximations. [Tate, 1967] recommend to use the Hugoniot Elastic Limit (HEL) as the dynamic yield strength of the material during his studies, [Tabor, 2000] approximate the dynamic yield strength based on the Brinell Hardness number of the material and [Taylor, 1947] determined the dynamic yield strength based on experiments on impact of cylinders against rigid flat targets.

The group has adopted the method of Taylor, [Taylor, 1947], and use his equation for determining the dynamic yield strength as described in [Rosenberg and Tsaliah, 1990] whom found good correlation between the estimate and experimental findings. During the derivation of the equation, assumptions are made that only makes it applicable for velocities up to u_{plas} . Furthermore, the dynamic yield strength is strain-rate dependent, meaning a higher impact velocities means a higher dynamic yield strength. The ratio between the static yield strength, and the dynamic yield strength in steel is

$$\frac{Y_D}{\sigma_y} = 1 + k \dot{\epsilon}^n \quad (3.57)$$

where σ_y is the static yield strength, k and n are constants, and $\dot{\epsilon}$ is the strain rate, [NagarajaRao et al., 1966].

Small deviations from this is seen in the following, as the data obtained for the equation is based on experiments conducted by the group, and external effects might have influenced the quality of this data.

The equation relates the impact velocity, shortening of the cylinder and the dynamic yield strength as

$$\ln \frac{L}{L_0} = -\frac{\rho_p v_0^2}{2Y_D} \quad (3.58)$$

where L/L_0 is the shortening of the projectile, ρ_p is the material density, v_0 is the impact velocity and Y_D is the desired dynamic yield strength.

Experiments performed with metal cylinders, see chapter 5 for the test campaign etc., for as broad a velocity range as possible with the experimental equipment have been

conducted, and the results are listed in table 3.2. The table states the impact velocity and the calculated dynamic yield strength Y_D . See table 5.3 for relevant before and after length of the projectile.

Steel		Aluminium	
Velocity [m/s]	DYS [GPa]	Velocity [m/s]	DYS [GPa]
223	1,62	291	0,764
283	1,84	368	0,738
322	1,66	416	0,687
351	1,62	453	0,633
395	1,79	510	0,689
428	1,87	530	0,598

Table 3.2: *Experimental determined Dynamic Yield Strength (DYS). As the brass projectiles shatters on impact, a dynamic yield strength is indeterminable using this method. The decrease in DYS of the aluminium with increasing velocity is due to poor experiments. Theory and equations dictate an increase with increasing strain rate.*

There is some discrepancy in the increase of dynamic yield strength and increase in impact velocity, i.e. strain rate. This is deemed acceptable, as it most likely is prescribed crudeness in the experiments. The results are very similar for the results obtained for steel in den Reijer [1991] at $\approx 1,7$ GPa, and Rosenberg and Tsaliah [1990] at $\approx 1,9$ GPa.

Another approach for determining the dynamic yield strength.

As eq. 3.58 needs an experiment to determine the final length before obtaining the dynamic yield strength, another method is used in conjunction with Taylor's maximum strain equation as it is explained here, [Taylor, 1947]. An estimate of the dynamic yield strength can be obtained by equating kinetic energy at impact with plastic strain energy [Hawkyard et al., 1968]. If the mean representative dynamic yield stress is \overline{Y}_D , the plastic work dW_d absorbed by an elemental volume dV in straining by a representative natural strain $\overline{\epsilon}$ is

$$dW_d = \overline{Y}_D \overline{\epsilon} dV \tag{3.59}$$

Integrating over the entire deformed volume yields the total plastic work for the dynamic operation

$$W_d = \int_V \overline{Y}_D \overline{\epsilon} dV \tag{3.60}$$

By assuming that the axes of principal stresses lie on the cylindrical coordinate system, so the elements are considered to be subjected to uni-axial compression, and the shear between elemental slices is neglected, the following apply

$$\begin{aligned} \overline{\epsilon} &= \epsilon_z = \epsilon && \text{for the axial strain} \\ \text{and} &&& \\ \overline{Y}_D &= \sigma_z = Y_D && \text{for the axial stress} \end{aligned}$$

and the work equation becomes

$$W_d = Y_D \int_V \varepsilon dV \quad (3.61)$$

Neglecting elastic and temperature energy losses and assuming complete conversion of kinetic energy to plastic work leads to

$$\frac{1}{2} V \rho_p v_0^2 = Y_D \int_V \varepsilon dV \quad (3.62)$$

and the dynamic yield strength can be written as

$$Y_D = \frac{\frac{1}{2} V \rho_p v_0^2}{\int_V \varepsilon dV} \quad (3.63)$$

If ε_m is the mean strain over all the deformed volume, the specific plastic work is

$$\begin{aligned} \frac{W_d}{V} &= Y_D \varepsilon_m = \frac{Y_D}{V} \int_V \varepsilon dV \\ \Rightarrow \varepsilon_m &= \frac{1}{V} \int_V \varepsilon dV \end{aligned} \quad (3.64)$$

and eq. 3.63 becomes

$$Y_D = \frac{\rho_p v_0^2}{2 \varepsilon_m} \quad (3.65)$$

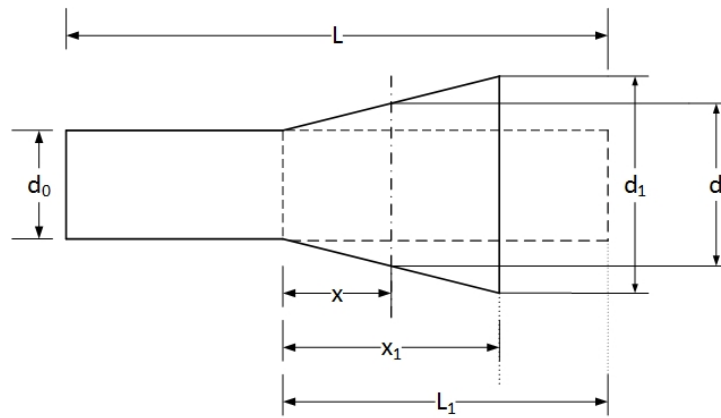


Figure 3.12: *Strain analysis of a cylindrical projectile impacting a rigid target.*

The mean strain in eq. 3.64 can be obtained from figure 3.12 as follows

$$dW_d = Y_D \varepsilon dV = 2 Y_D \ln \frac{d}{d_0} dV = 2 Y_D \ln \frac{d}{d_0} \frac{\pi}{4} d^2 dx \quad (3.66)$$

where ε is the true strain.

From geometrical considerations, see figure 3.12, it can be found

$$\frac{d_1 - d_0}{x_1} = \frac{d - d_0}{x} \quad (3.67)$$

which gives

$$d = d_0 \left(1 + \left(\frac{d_1}{d_0} - 1 \right) \frac{x}{x_1} \right) \quad (3.68)$$

Substituting in eq. 3.66 gives

$$dW_d = Y_D \frac{\pi}{2} d_0^2 \left(1 + \left(\frac{d_1}{d_0} - 1 \right) \frac{x}{x_1} \right)^2 \ln \left(1 + \left(\frac{d_1}{d_0} - 1 \right) \frac{x}{x_1} \right) dx \quad (3.69)$$

Integrating the latter equation between $x = 0$ and $x = x_1$ gives

$$W_d = \frac{2 Y_D \pi d_1^3 x_1}{9(d_1 - d_0)} \left(3 \ln \frac{d_1}{d_0} - \frac{d_1^3 - d_0^3}{d_1^3} \right) \quad (3.70)$$

Eq. 3.70 gives the plastic work in terms of the dynamic stress Y_D , the projectile diameters d_1 , d_0 and the deformed length x_1 . The deformed volume is obtained from figure 3.12

$$V = \frac{\pi x_1}{3} \left(\frac{d_1^3 - d_0^3}{d_1 - d_0} \right) \quad (3.71)$$

and the specific work becomes

$$\frac{W_d}{V} = Y_D \left(\frac{2 d_1^3}{d_1^3 - d_0^3} \ln \frac{d_1}{d_0} - \frac{2}{3} \right) \quad (3.72)$$

Using eq. 3.64 with eq. 3.72 leads to the mean strain

$$\varepsilon_m = \left(\frac{2 d_1^3}{d_1^3 - d_0^3} \ln \frac{d_1}{d_0} - \frac{2}{3} \right) \quad (3.73)$$

If the maximum diameter of the projectile is known the mean strain is known and from eq. 3.65 one can obtain the dynamic yield strength for the projectile.

To find the maximum diameter d_1 for a projectile, Taylor's max strain equation is used, [Taylor, 1947]

$$\varepsilon = \frac{d_1^2 - d_0^2}{d_1^2} = \frac{v_0}{c} \quad (3.74)$$

where v_0 is the impact speed and c is the velocity of the plastic stress wave in the projectile material. This equation is only valid for impact velocities less than c as it yields an infinite deformed diameter at $v_0 = c$.

This method shown above seems to yield a good results for the dynamic yield strength when the data collected by the experiments are not really convenient to be used for obtaining Y_D , or experiments cannot be performed beforehand. The results obtained here are used in the calculations for the model derived in section 3.3.

The results for the dynamic yield strength for the different projectiles are listed in table 3.3.

Steel		Aluminium		Brass	
Velocity [m/s]	DYS [GPa]	Velocity [m/s]	DYS [GPa]	Velocity [m/s]	DYS [GPa]
223	1,45	291	0,64	223	1,05
283	1,73	368	0,75	283	1,22
322	1,90	416	0,80	322	1,30
351	2,00	453	0,83	351	1,35
395	2,15	510	0,87	395	1,38
428	2,23	530	0,88	428	1,4

Table 3.3: *Analytical determined Dynamic Yield Strength (DYS). The impact velocity of steel is used for the brass, as a full test campaign for brass is not conducted.*

It is seen that the values obtained analytically are higher than those obtained experimentally. The measurements following the experiments may not be precise enough for high impact velocities which can yield a deviation from the correct results, besides that in the analytical solution, the values for the maximum deformed diameter are obtained based on eq. 3.74 which is used for rigid targets.

The initial penetration velocity \dot{x}_0 .

The initial penetration velocity has to be determined, as, unlike in cases of impact against ceramics where the projectile experiences dwelling meaning $\dot{x}_0 = 0$, the initial penetration velocity into metallics are different from zero.

The initial penetration velocity is dependent on the ratio of acoustic impedance, i.e. the product of the material density and sound velocity, of the materials [Rosenberg and Dekel, 2012]. As the speed of sound is very similar in most metals, the ratio is often dependent on the density ratio alone.

It is from experimental results determined, that there exist a linear relation between the impact velocity v_0 , and the initial penetration velocity \dot{x}_0 as

$$\dot{x}_0 = \alpha + \beta v_0$$

where α and β are the linear fitting parameters and velocities are in km/s, [Orphal and Anderson, 2006].

The group simply do not possess the means to conduct the necessary experiments for determining these parameters where α is purely a fitting parameter, and test data does not exist for the velocity range the present experiments are to be conducted in as the research in [Orphal and Anderson, 2006] suggest that the linear relation somewhat breaks down at low velocities.

Some contradictions regarding if this is the most correct way of approximating the initial penetration velocity have been seen. But on the other hand, articles in which this specific approximation have also been seen. Especially for long-rod penetrators and high-velocity impact the approximation seems to be almost exact, [Rosenberg and Dekel, 2012]. Furthermore, [den Reijer, 1991] use a similar approximation of the penetration velocity when deriving the resistance force in penetration of comminuted ceramics, using standard military armour piercing projectiles, and suggest that the penetration velocity afterwards is fitted to experimental observations. Similarly, a research group for determining the dynamic yield strength of balls made of steel uses the same approximation of the penetration velocity, [Manjit Singh et al., 2008].

This confirm the partial truth in this approximation, and the group adopts a similar approach, and the β parameter is material dependent by the density as previously mentioned

$$\beta = \frac{1}{1 + \sqrt{\frac{\rho_t}{\rho_p}}} \quad (3.75)$$

and assume $\alpha = 0$. This assumption is likewise used for incompressible penetration.

The results for the projectile/target combinations used in this project are summarised in table 3.4.

Target	Projectile	β
Quardian/(ARMOX)	Steel	0,499/(0,498)
Quardian/(ARMOX)	Aluminium	0,374/(0,373)
Quardian/(ARMOX)	Brass	0,508/(0,507)

Table 3.4: β parameters to be used in $\dot{x}_0 = \beta v_0$ to determine the penetration velocity. The difference in density between Quardian and ARMOX is assumed to be 50 kg/m³.

Hereby are all the necessary parameters for the models determined. Parameters such as dimensions, mass and densities are presented in chapter 5.

CHAPTER 4

NUMERICAL SIMULATIONS

Numerical simulations for impacts are usually done in hydrocodes. Hydrocodes are numeric programs specialised in solving impact problems. According to [Zukas, 2004] the name hydrocode stems from the earliest codes where hydrodynamic behaviour was assumed for high strain rate impact problems. Most hydrocodes solve transient problems by an explicit formulation as this is, usually, superior for small time steps.

The commercial hydrocodes Ansys Autodyn and Ansys explicit dynamics are used to simulate the impacts. As the names suggest both programmes are part of Ansys simulation suite, version 17.2. In fact, Ansys explicit dynamics is in reality only a pre- and post-processor, as it uses the Autodyn solver. Ansys Autodyn gives more possibilities and control to the user, while Ansys explicit dynamics is more easy to use and gives the possibility of parametrising inputs and outputs. Parametrising is especially useful when conducting multiple similar studies, such as convergence study, and also gives the possibility of using optimisation on a simulation.

Both Ansys Autodyn and Ansys explicit dynamics are used during the project, but only Ansys explicit dynamics for the final studies, mainly due to its parametrising possibilities. Both also have access to a library of explicit material models, this is subsequently called the Ansys material library. It is of course also possible to implement custom materials based on user given data.

4.1 Methods

Ansys Autodyn contains multiple methods for solving problems of different characteristics, which can also be combined for highly complex problems. Some of them are:

- Finite element for structural dynamics (Lagrange)
- Finite volume for transient fluid dynamics (Euler)
- Adaptive mesh for structural dynamics with large deformation (ALE)
- Mesh-free particle for large deformation and fragmentation (SPH)

When using Ansys explicit dynamics only Lagrange and Euler are directly available. Systems can be pre-processed in Ansys explicit dynamics and then migrated to Ansys Autodyn and converted to or have SPH and ALE parts added. Post-processing the results back in Ansys explicit dynamics has not been found to be possible.

4.1.1 Lagrange

In Lagrange method the mesh follows the material as it deforms, the material in a cell or element is the same before and after deformation. This makes it easy to keep track of material and material flow during the simulation. Contact is also handled more easily as

it can be determined as contact between meshes with distinct nodes and element edges. The downside is when large deformations occur the elements can distort and thereby lose accuracy and as the time step is determined from the smallest element length in the system the simulation can begin to use such a small time step that it effectively grinds to a halt. To counter this the method of erosion is often employed, this is different from the physical erosion and is simply the removal of elements that fulfil certain conditions, often related to the size of the time step. When employing erosion it is possible to retain the nodes from eroded elements, as the nodes contain the mass of the element, as well as displacement, velocity and acceleration. It is therefore possible to keep the kinetic energy in the system, the potential energy from stresses is however lost.

4.1.2 Euler

In the Euler method the mesh is fixed and material flows through the mesh from cell to cell. The downsides of Lagrange are therefore omitted as the cells do not distort and large deformations do not affect the time step of the simulation. As material boundaries are not defined by the mesh these, and contact, must be defined and tracked by different means. This adds extra complexity to the simulation and as the mesh is static it needs to be defined for the entire zone that material may move to. The Euler method is not used in this project and is not described further.

4.1.3 ALE

Arbitrary Lagrange Euler is, as the name may suggest, a mixture of the Lagrange and the Euler method. It works as a Lagrange simulation, with deforming mesh, which at a set interval of iterations restructures the mesh so that highly skewed elements are avoided. The restructuring is usually conducted on internal nodes so that the boundary of the material is kept. During the restructuring, the deformations and stresses are transferred from former nodes and elements to new nodes and elements. This process is similar to deformation with Euler method, hence the name, and if the restructuring is done at each iteration ALE becomes, more or less, pure Euler. ALE gives the advantages of both Lagrange and Euler at the cost of higher computational demands, more complexity and loss of history of each node.

4.1.4 SPH

Smoothed-Particle Hydrodynamics, also known as mesh less simulation, is a method where the nodes are not connected by elements or cells and is thereby mesh less. By not connecting the nodes by elements the problem of large distortion and infinitesimal time steps are avoided. Break up and fracture of material are also handled more naturally. The SPH method is highly complex and have many tuning parameters. It is the most recent of the mentioned methods and is still under heavy development.

4.2 Material models

The model for a material in dynamic simulations is build up of multiple parts. For each part there exist many different models depending on behaviour and application. From simple linear model identical to static behaviour to complex ones taking many factors into account, even lookup tables from extensive lab tests. Different parts can be mixed and matched to fit a specific use or available data.

4.2.1 Equation of State

Equation of State (EOS) is the relation between the pressure, or hydrostatic stress, the local density, and the local specific energy. The simplest EOS is Hooke's law, in hydrocode it is often formulated by means of the bulk modulus. The bulk modulus gives a linear relation between hydrostatic stress and change in volume, and does not take temperature into account. Hooke's law is valid for linear elastic materials and yields good results for relatively small volumetric change, around 2%.

$$\sigma_{hyd} = -p = 3 K \epsilon_{hyd} \quad (4.1)$$

In Ansys Autodyn this EOS is called linear EOS.

The aluminium models in Ansys material library use a linear shock EOS. According to [ANSYS Inc., 2016] this EOS is based on Rankine-Hugoniot equations for the shock jump conditions and relates the pressure to the change in density (change in volume), specific energy and particle velocity. It is formulated in equation 4.2.

$$\begin{aligned} p &= p_H + \Gamma \rho(e - e_H) \\ p_H &= \frac{p_0 C_0^2 u(1 + \mu)}{(1 - (S - 1)\mu)^2} \\ e_H &= \frac{1}{2} \frac{p_H}{p_0} \left(\frac{\mu}{1 + \mu} \right) \\ \mu &= \frac{\rho}{\rho_0} - 1 \end{aligned} \quad (4.2)$$

where p is pressure, e is specific energy, u is particle velocity, ρ is density, C_0 is the bulk sound speed called C_1 in the library, S is the Hugoniot linear slope coefficient called S_1 in the library, and Γ is the Gruneisen coefficient and relates energy and volume to pressure. Both EOS are combined with a shear modulus for deviatoric distortion.

4.2.2 Strength

During large deformation the material often starts to yield and deform plastically. When and how this happens is often termed as strength of the material. One of the most used ones for ductile materials is Johnson-Cook's strength model, see [Johnson and Cook, 1983], which takes strain, strain rate and temperature effects into account, eq. 4.3. This makes it highly applicable for transient problems where strain rate hardening and thermal

softening can not be ignored. The model contains five constants, A is the yield strength, B is the strain hardening constant, n is the strain hardening exponent, C is the strain rate constant and m is the thermal exponent. ϵ_p is the effective plastic strain, $\dot{\epsilon}_p$ is the effective plastic strain rate, $\dot{\epsilon}_0$ is the reference strain rate, and T is temperature. A, B and n can be determined independently of C and m by testing at strain rate 1 s^{-1} at room temperature, the strain rate term and thermal term thereby equates to one. The remaining terms are typically determined by fitting to data at varying strain rates and temperatures.

$$Y = [A + B\epsilon_p^n] [1 + C \ln(\dot{\epsilon}_p^*)] [1 - T^{*m}] \quad (4.3)$$

$$\dot{\epsilon}_p^* = \frac{\dot{\epsilon}_p}{\dot{\epsilon}_0}$$

$$T^* = \frac{T - T_{room}}{T_{melt} - T_{room}}$$

The Steinberg-Guinan model is another strength model often used in hydrocode. It is the strength model used for most of the aluminium models in the Ansys material library. Steinberg-Guinan takes the saturation of strain rate effects, compared to other factors, some materials exhibit at strain rates greater than 10^5 s^{-1} , into account. It also accounts for changing shear modulus due to pressure and temperature. It takes the form of eqs. 4.4 and 4.5.

$$G = G_0 \left\{ 1 + \left(\frac{G'_P}{G_0} \right) \frac{P}{\eta^{1/3}} + \left(\frac{G'_t}{G_0} \right) (T - 300) \right\} \quad (4.4)$$

$$Y = Y_0 \left\{ 1 + \left(\frac{Y'_P}{Y_0} \right) \frac{P}{\eta^{1/3}} + \left(\frac{Y'_t}{G_0} \right) (T - 300) \right\} (1 + \beta\epsilon)^n \quad (4.5)$$

Where Y is the yield strength, G is the shear modulus, G_0 is the shear modulus at 300 kelvin, Y_0 is the yield strength at Hugoniot elastic limit, T is temperature in kelvin, ϵ is effective plastic strain, η is compression ratio, $\eta = V_0/V$, β is the strain hardening constant and n is the strain hardening exponent. Primed parameters subscripted with T and P are the derivatives of the parameter with respect to temperature and pressure respectively, at a reference state with $T = 300 \text{ K}$, $P = 0$ and $\epsilon = 0$.

In Ansys it has an built-in failure mechanism as the shear modulus and yield strength are set to zero if the temperature exceeds the specified melting temperature.

4.2.3 Failure

At a sufficiently high load, any material will fail. This is especially true in hydrocode where stresses can reach very high magnitudes. Breakup of structures are often an important factor in hydrocode studies. To model this in hydrocode, failure is divided into two parts, failure initiation and post failure response. *Failure initiation*; model when failure occurs in a given element. Several different criteria exist to determine failure initiation; plastic strain, principle stress failure, Johnson-Cook failure and more. *Post failure response*; model a given element's strength characteristics after failure. Two different models exist for post failure response, instantaneous failure and gradual failure. Gradual failure is also called damage. For instantaneous failure the deviatoric stresses are set to zero immediately upon failure and subsequently kept there. The element is additionally only able to support

compressive pressure. For gradual failure, the stresses in the element are gradually limited. Failure can also be used as a criterion for element erosion. Due to time constraints failure is not investigated further or applied to the material models.

4.3 Simulations and results

The following section treats the simulations of cylinders impacting an armour plate. It is investigated whether it is sufficiently accurate to simplify the simulations to 2D with axisymmetry, the size of a sufficiently fine mesh as well as convergence of deformation, and the final simulations mimicking the experimental setup. Most of the simulations involve impact onto a plate of ARMOX 500 or equivalent. The data for EOS and Johnson-Cook strength for ARMOX 500 are obtained from [SSAB Oxelösund AB, 2007].

4.3.1 Comparing axisymmetric and full 3D

The nature of numerical explicit problems make them computationally heavy and thereby time consuming. To reduce the computation time it is possible to introduce simplifications of the system. In general all problems are spacial, expanding in all three dimensions. Modelling this accurately causes the largest and computationally heaviest system. Often problems contain some sort of symmetry and including this can often half or quarter the size of the system. The problems investigated in this project are all symmetric around an axis of rotation, called axisymmetric. The axisymmetric simplification is a modification of the two dimensional formulation. By using the axisymmetric simplification the system is reduced by an entire dimension, making the computation much lighter. The very non-linear nature of hydrocode require that symmetry should be used with great care as symmetry conditions may cause non-physical effects due to boundary conditions. These can be absorption or reflection of stress waves at symmetry boundaries. There can especially be problems with free nodes from eroded elements that collect at symmetry boundaries and move along these like a jet penetrating the remaining material.

To verify if the use of axisymmetry is applicable, and do not cause significant differences in results, a comparison of a full 3D and an axisymmetric simulation is conducted. The comparison is conducted on a system modelling the impact of a cylinder of 4340 steel from the material library on an ARMOX 500 plate. The cylinder is modelled with a diameter of 10 mm and a length of 15,2 mm, the plate is also modelled as a cylinder with a thickness of 12 mm and diameter of 100 mm. The plate is modelled as a cylinder to comply with the axisymmetric model and the dimensions are chosen to emulate the physical target used in experiments. The plate is constrained at the outer edge. The full 3D model consist of 198930 nodes and 183204 elements while the axisymmetric model consist of 2220 nodes and 2070 elements. Additionally each node of the axisymmetric only contains two degrees of freedom, compared to three for the full 3D, as it is in essence a 2D system. The axisymmetric system is thereby reduced to less than 1/140 of the computations of the full 3D system.

The most relevant section of each mesh is shown in figure 4.1.

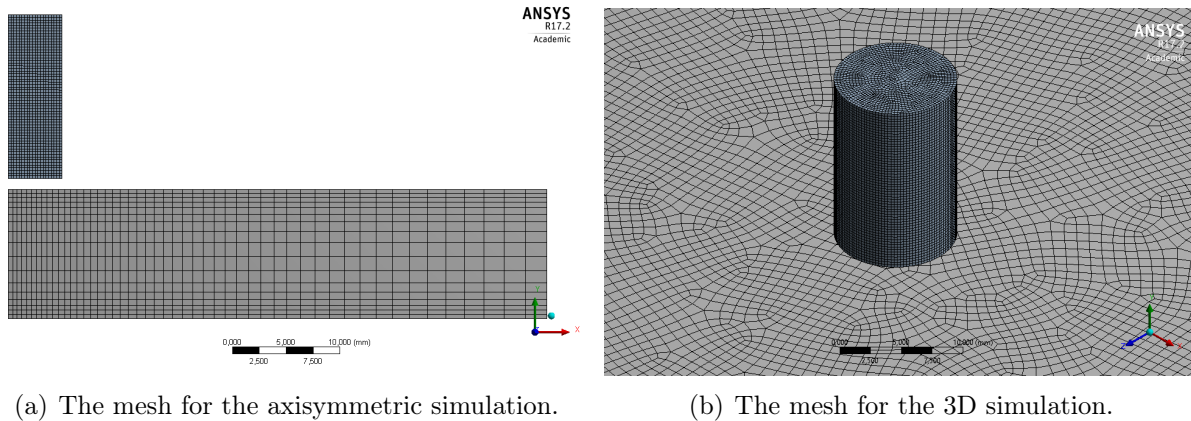


Figure 4.1: *The meshes for the 3D and axisymmetric simulations.*

Figure 4.2 shows the deformation at the top and bottom of the cylinder as it impacts the plate, it also shows the total length of the cylinder determined from the deformations. Figure 4.2 shows that there is no noticeable difference of deformation of the cylinder between full 3D and axisymmetric. This is to be expected as both systems have nice regular shaped elements. In a case with for instance spherical or ogive shape it may prove difficult to mesh the model into nice regular elements in either 3D or 2D. In such a case there may be more difference between full 3D and axisymmetric. There is also no erosion which is often an issue with axisymmetry. As there are practically no difference between full 3D and axisymmetric there are no reasonable reason not to use axisymmetry when this is applicable.

4.3.2 Convergence study of hydrocode

One of the most common and important criterion for validating a numerical method is convergence. The convergence criterion states that as the model is discretized progressively finer, the solution should converge on a fixed value. For hydrocode the discretization is the mesh size, meaning element size for the Lagrange method. To check that a given numerical code converges, a convergence study is performed. Performing a convergence study also gives insight into the necessary mesh size to obtain sufficiently accurate results.

A convergence study is performed for a cylinder with a length of 15 mm and a diameter of 10 mm, impacting a rigid target at 300 m/s. This is a relevant system as it resembles the experimental set up. The problem is modelled as axisymmetric 2D, and mesh sizes of 0,5 mm, 0,25 mm, 0,125 mm, and 0,0625 mm. The material is steel 4340 from the Ansys material library with linear EOS and Johnson-Cook strength.

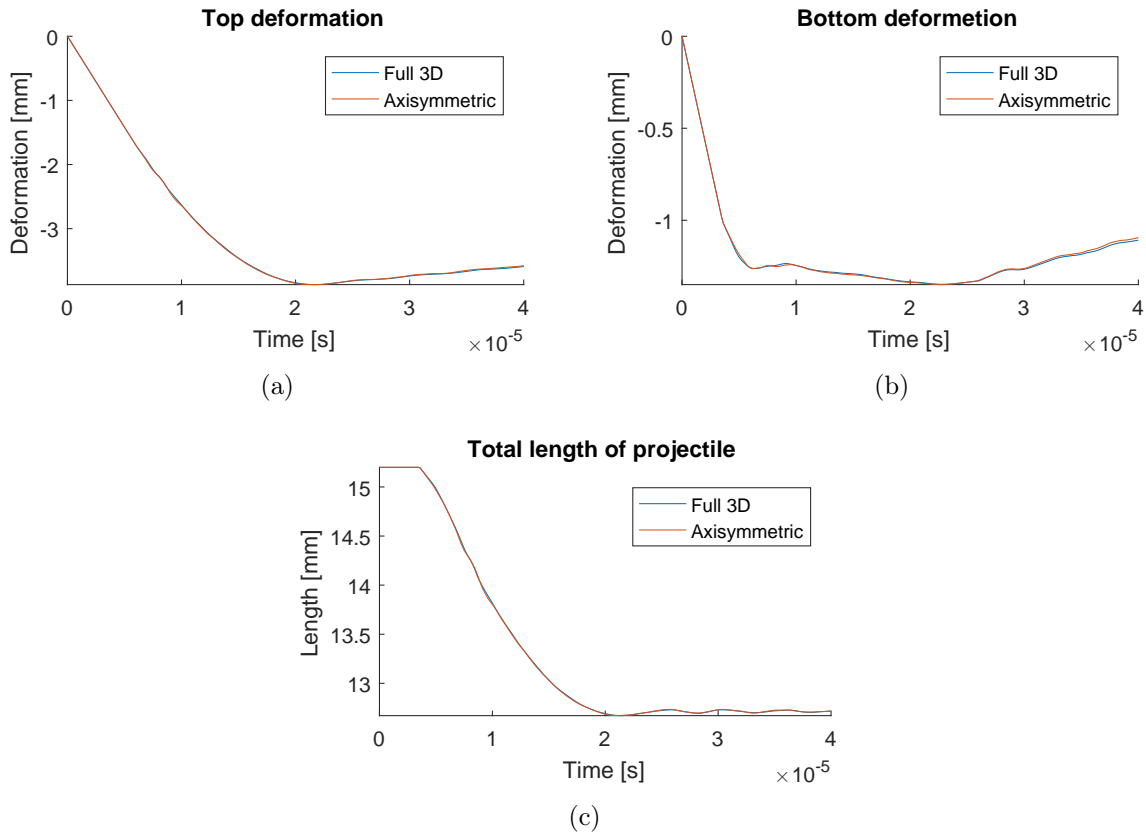


Figure 4.2: Comparison of the deformation at the top and bottom of a cylinder and the total length for an axisymmetric and a full 3D simulations.

Deformation data are extracted from the centre topmost point and bottom most point. The difference in deformation between these points effectively equates to the reduction in length of the projectile. The data over time are shown in figure 4.3. As can be seen in figure 4.3 the results are reasonably close to each other, with the line for 0,5 mm mesh as the most diverging. Figure 4.3(b) shows some nonconsistent differences between all four lines at $0,4 \cdot 10^{-5}$ to $1 \cdot 10^{-5}$ seconds, where the projectile hits the rigid plate and the projectile centre bounces. It is important to note that the model is set up so that there is a gap of 1 mm between the bottom of the projectile and the rigid plate, this is represented by the dotted line at -1.

Figure 4.4 shows how the mesh of the projectile penetrates and overlap the mesh for the plate. In figure 4.3(b) it is seen that the incompatible penetration is largest for 0,5 mm mesh size and gets smaller as the mesh is refined. This is due to the way the time step size is determined, larger elements mean larger time step, so change in displacement from one cycle to the next also gets larger. This then means more penetration before contact is activated. Even though the four mesh sizes give quite different results for displacement at the bottom right at the start of impact, they all, more or less, reach the same displacements after the initial impact, albeit in slightly different phase of vibration. Please note, that the 0,5 mm mesh gives results that are slightly different from the remaining. While there

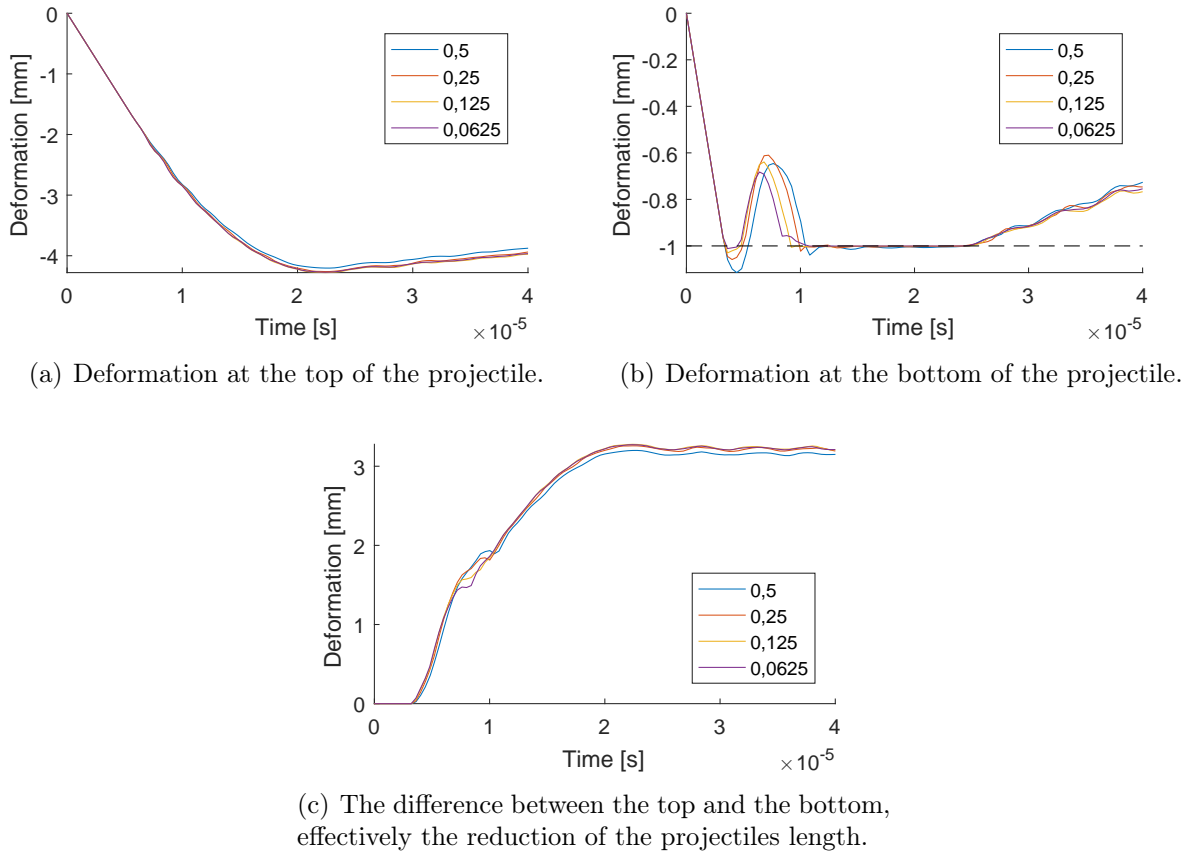


Figure 4.3: Comparison of deformation and reduction of length of a cylinder impacting a rigid target with different mesh sizes.

are no noticeable differences for 0,25 mm, 0,125 mm and 0,0625 mm mesh at the end of the simulation. It can therefore be concluded that a mesh size of 0,25 mm is sufficient for this specific problem as there is only little to no benefit of finer mesh, in regards to deformation.

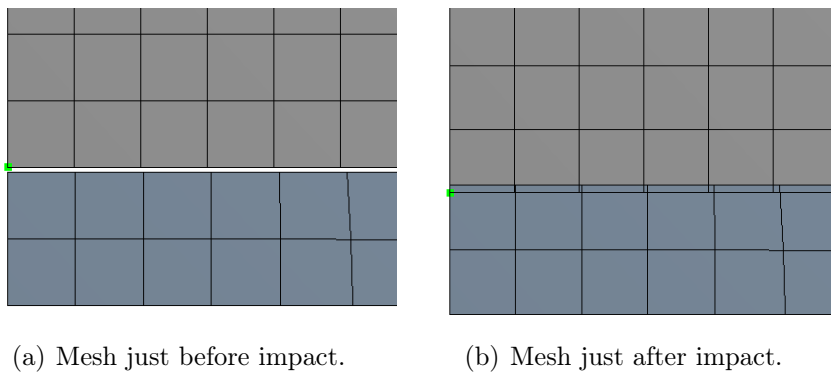


Figure 4.4: A large time step may cause overlapping of meshes.

4.3.3 Simulation of experiments

The experiments described in chapter 5 are recreated in Ansys explicit dynamics using axisymmetry. Only steel and aluminium are investigated as experiments showed brittle failure for brass, and brittle failure has not been successfully simulated during this project. The materials used in the simulations for the projectiles are both from the Ansys material library. Steel 4340 for the steel projectiles and Al 2024-T4 for the aluminium projectiles, which represents the actual materials sufficiently. The model for 4340 steel consist of a linear EOS with a bulk and a shear modulus and Johnson-Cook strength model. The 2024-T4 aluminium model consist of a linear shock EOS and a Steinberg-Guinan strength model. Non of the materials contain a failure model.

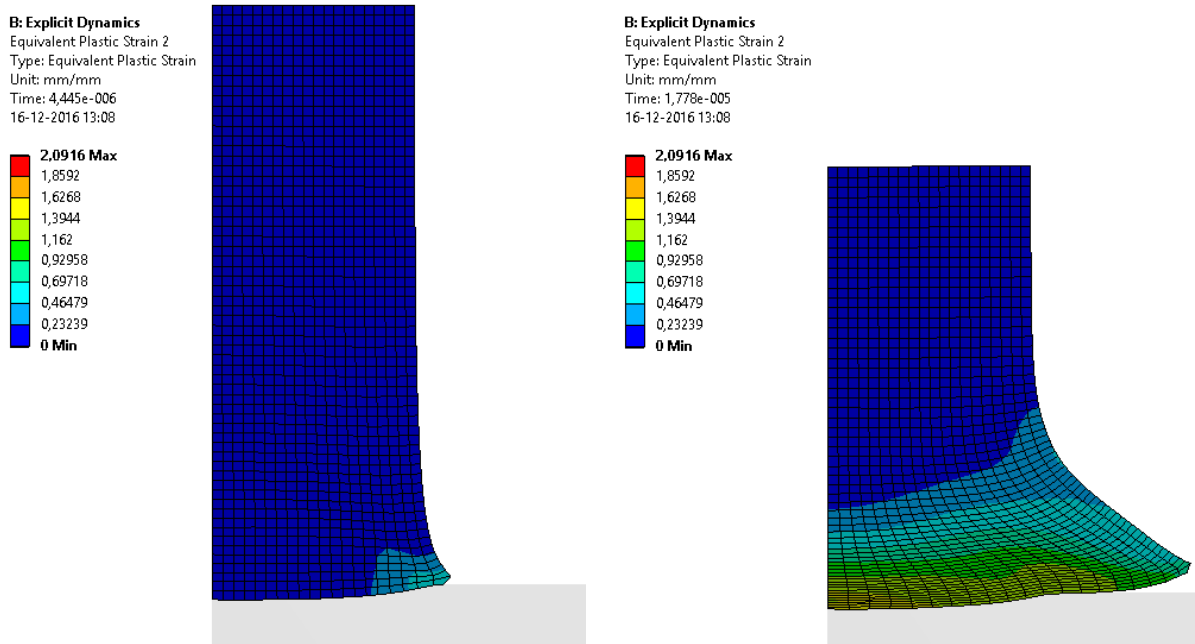
The simulations are run without erosion. From the simulations axial deformation values for both the top and bottom of the projectile are obtained. From these the total axial deformation can be determined and thereby the deformed length. The deformation values are taken at the last time step. The obtained lengths of projectiles are shown in chapter 6, table 6.6 for steel and table 6.7 for aluminium.

4.3.4 Choosing materials

As stated earlier the cylinders are modelled with material models and data from the Ansys material library, steel 4340 and Aluminium 2024-T4. The data for steel 4340 are from [Johnson and Cook, 1983] and the data for aluminium 2024-T4 are from [Steinberg, 1991]. These materials where chosen on the basis that they are the materials in the library that yield results that best mimics the results from experiments, see chapter 6 for comparison. This can in ways make the simulations be regarded as self fulfilling. It should be noted that the simulation results don't fit at one impact velocity only, but the entire tested range, especially for steel. Explicit material models are often derived for a specific strain rates and/or temperatures, use of the model outside the range at which the data is obtained may give results far from that of the actual material the data is for. The best solution is of course to do material test and obtain data for the specific material batch and at the relevant strain rates and/or temperatures.

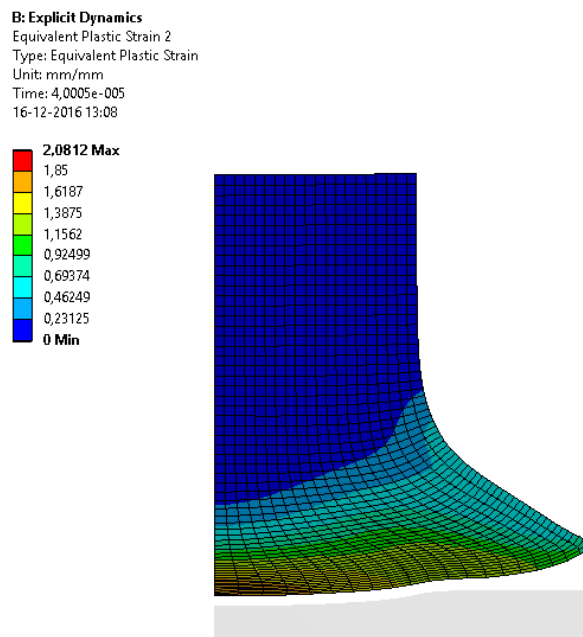
It may also be that simulation results for impact ballistic are not that sensitive to material properties. The Ansys library contains 211 explicit material models (three just for water) whereas eight of those are types of steel and seven are aluminium. In comparison SolidWorks comes with 31 types of steel for linear finite element analysis as standard and can easily be expanded with hundreds more as official downloads. This of course has to do with the fact that explicit material models require much more work to make than linear models. But it must also be taken into consideration whether the lack of material data is an indication of a lack of demand for more specific material data. Impact ballistic is a field with quite large tolerances compared to many other fields of mechanics.

For a description on how material constants can be obtained see appendix D. This method is however definitely self fulfilling and if not used over a wide test range it would not change the results much from those obtained with library materials.



(a) 4,445 μs into the simulations.

(b) 17,78 μs into the simulations.



(c) End of simulation after 40,00 μs .

Figure 4.5: *Equivalent plastic strain in a steel cylinder impacting an ARMOX 500 plate at 427,65 m/s.*

CHAPTER 5

EXPERIMENTS AND LABORATORY WORK

The following chapter describes the impact experiments performed by use of a gas cannon, and the laboratory work performed for obtaining the necessary data for comparison with the analytical and numerical findings.

5.1 Presentation of experimental equipment and set-up

This section presents the equipment and set-up used for the live firing experiments. The experiments are performed in the terminal ballistics laboratory in the basement of Fibigerstræde 14, Aalborg University.

5.1.1 Ballistic test facility

The gas cannon in the terminal ballistics laboratory, figure 5.1, is approved to a pressure of up to 200 bar. A chamber in the cannon is filled with compressed atmospheric air to the desired pressure by use of a regular industrial compressor capable of generating the desired pressure. A remote operated valve, by chord, permits release of the pressure from safety outside the room. Barrels in different diameters exist, but in the present studies all projectiles are manufactured or ordered for a diameter of 10 mm.

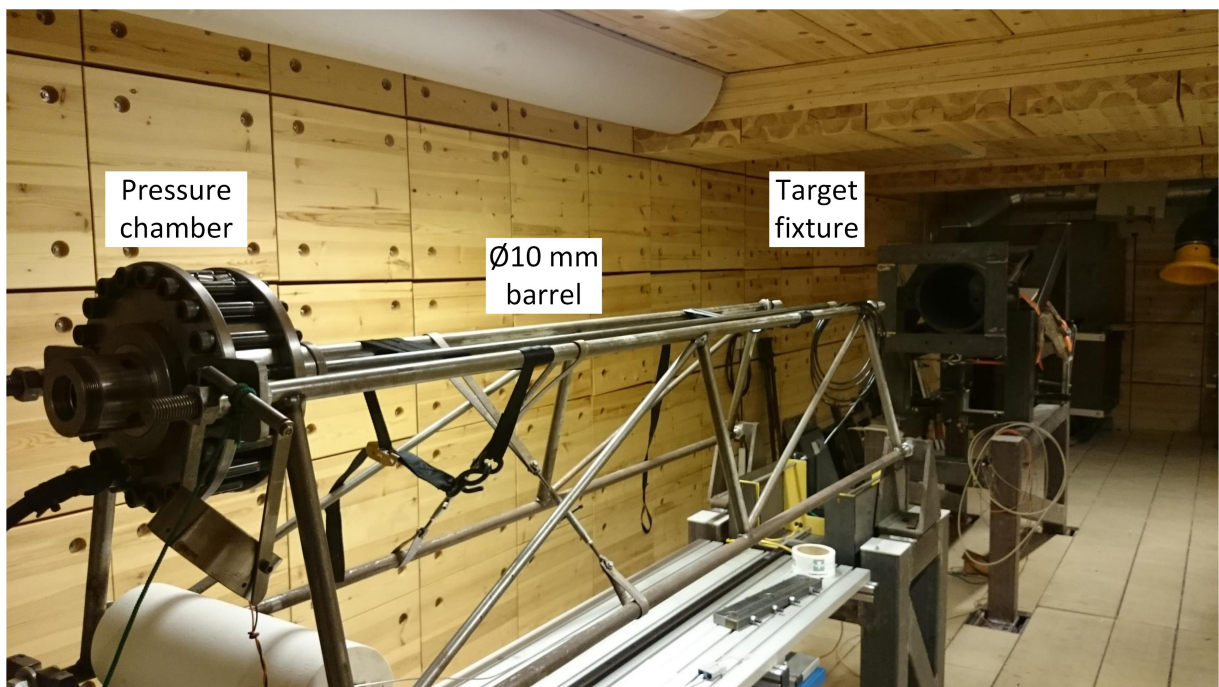


Figure 5.1: *The ballistic test facility in the basement of Fibigerstræde 14.*

In front of the target fixture, a chronograph is located to measure the time it takes for the projectile to travel the set distance between its two photo sensors and thereby outputting the strike velocity of the projectile. Furthermore, a projectile catcher is mounted to the target fixture for collection of projectile and any fragments.

5.1.2 Projectiles

This section presents the projectiles used in the models and experimental work. The projectiles consists of cylinders of three different materials, and high hardness steel spheres for use in e.g. ball bearings have been used for calibration shots. These are not presented in the following.

The hardness tests for the cylindrical projectiles are performed on two representatives for each material, to detect an anomaly if one existed. The projectiles are made by use of a recessing tool on a lathe, and the hardness tests are conducted on the free surface by the following procedure. The procedure on especially the steel cylinder generated a lot of thermal energy, and even though cooling is used, it cannot be disregarded that it might have an effect on the hardness. Figure 5.2 shows the approximate measurement locations on the cylinder. As seen from the values in table 5.1, the standard deviation of, specifically the steel cylinder, is so small that if the hardness of the steel has been influenced, at least it has been influenced over the entire surface. It is difficult to say anything about a possible influence in the depth of the material. In appendix B, a table of the hardness values obtained is found.

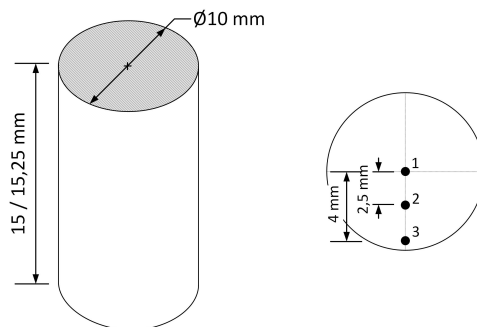


Figure 5.2: *Points of measure for the hardness test on the cylinders. The shaded face indicate the surface at which the tests are performed. The cylinder is Ø10 mm.*

The projectile parameters are given in table 5.1;

			Steel	Aluminium	Brass
Density	(ρ_p)	[kg/m ³]	$7,75 \cdot 10^3$	$2,79 \cdot 10^3$	$8.32 \cdot 10^3$
Proof strength	(σ_y)	[MPa]	725	350	471
Youngs' modulus	(E)	[GPa]	205	70	100
Dynamic yield strength	(Y_D)	[GPa]	{1,62-1,87}	{0,598-0,764}	{1,05-1,40}
Linear Strain Hardening modulus	(E_w)	[GPa]	3,09	1,29	2,01
Hardness		[BHN]	$209 \pm 3,61$	$116 \pm 0,577$	$157 \pm 1,73$

Table 5.1: *Projectile material parameters for the models and experimental work. The hardness tests, HRB for brass, aluminium and steel, are converted to brinell hardness for the 3000 kg/f scale. Proof strength obtained from compression tests, appendix C. The test data is so poor, that common values of Youngs' modulus is used. The linear strain hardening modulus is approximated by Ramberg-Osgood, as seen in appendix C, and a range is given for the dynamic yield strength as it is strain rate dependent.*

5.1.3 Targets

This section presents the target plates used in the models and experimental work. The target plates consist of armour plates from SSAB Oxelösund AB [2007] from the ARMOX series and Quardian 500 from NLMK Clabecq [2016].

The target parameters are given in table 5.2;

			ARMOX 500	Quardian 500
Modulus of Elasticity	(E_t)	[GPa]	$2,07 \cdot 10^2$	$2,08 \cdot 10^2$
Density	(ρ_t)	[kg/m ³]	7850	7800*
Dynamic Yield Strength	(Y_{Dt})	[GPa]	1,47	1,47*
Resistance to penetration	(R_t)	[GPa]	8,00	8,01
Thickness		[mm]	{6 - 10}	12
Hardness		[BHN]	$451 \pm 7,52$	$441 \pm 11,4$

Table 5.2: *Target material parameters. For ARMOX the data sheet SSAB Oxelösund AB [2007]. Quardian data sheet is not available, so * indicates a common value/or the ARMOX value is assumed, the remaining properties are from tests. The resistance against penetration is approximated as described in section 3.2.*

5.2 Test campaign

The following section presents the test campaign that is conducted for obtaining the necessary data for comparison of the models, chapter 6. The purpose is to cover as great a velocity range as possible. As mentioned earlier, the gas cannon is approved for a pressure of up to 200 bar or $20,0 \cdot 10^6$ Pa, and two shots are the least amount of shots necessary at each pressure to avoid any significant outliers.

The projectiles are cylindrical, with a diameter of $\varnothing 10$ mm. The test campaign, and the results, are given in table 5.3.

Pressure [Pa]	Strike Velocity [m/s]	Before/After [mm]		[g]		Note
Steel						
$20,0 \cdot 10^6$	427,65	15,20	/ 10,40	9,3	/ 8,2	
$15,0 \cdot 10^6$	394,6	15,20	/ 10,85	9,3	/ 8,4	*
$10,0 \cdot 10^6$	350,65	15,20	/ 11,325	9,3	/ 8,9	
$7,50 \cdot 10^6$	322,05	15,20	/ 11,925	9,3	/ 9,3	
$5,00 \cdot 10^6$	283,35	15,20	/ 12,84	9,3	/ 9,3	
$2,50 \cdot 10^6$	222,55	15,20	/ 13,50	9,3	/ 9,3	
Aluminium						
$20,0 \cdot 10^6$	529,5	15,00	/ 7,80	3,3	/ 2,6	†
$16,0 \cdot 10^6$	509,7	15,00	/ 8,85	3,3	/ 2,8	†
$10,0 \cdot 10^6$	452,5	15,00	/ 9,55	3,3	/ 3,0	†
$7,50 \cdot 10^6$	416,2	15,00	/ 10,55	3,3	/ 3,0	†
$5,00 \cdot 10^6$	368,05	15,00	/ 11,61	3,3	/ 3,2	†
$2,50 \cdot 10^6$	291,1	15,00	/ 12,85	3,3	/ 3,3	*†
Brass						
$5,00 \cdot 10^6$	282,0	15,00	/ shatters	9,8	/ 5,5	
$2,50 \cdot 10^6$	214,7	15,00	/ shatters	9,8	/ 9,1	
$2,50 \cdot 10^6$	213,7	15,00	/ shatters	9,8	/ 9,0	
$2,50 \cdot 10^6$	212,2	15,00	/ shatters	9,8	/ 9,5	

Table 5.3: Test campaign for the cylindrical projectiles, for a total of 12 applicable shots for each material. 4 shots is made for the brass, due to the brittle state. * is based on one-shots-statistics as the projectiles are lost. † means the projectile is heavily pitched, and an average is made of measurements, see figure 5.3.

In case of highly pitched projectile impacts, and thereby skew projectiles from the experiments, an average of three measurements performed on the cylindrical projectile after impact is the stated value in table 5.3. This is seen in figure 5.3.

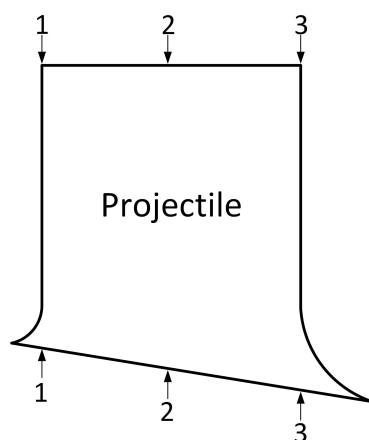


Figure 5.3: *Measurements are taken; (1): At intersection between vertical left side, and pitched face of projectile. (2) At center of the two faces of the projectile. (3): Opposite of (1).*

5.3 Experimental observations on projectiles

This section describes the observations made during the test campaign. It is primarily observations on the projectile, both during impact with the use of a high-speed camera, and after impact by studying projectile and eventual fragments. These observations indicate the defeat mechanisms the projectile undergoes during impact.

Deformation and fragmentation.

A range of deformation schemes and fragmentation schemes have been observed in the projectiles after impact. These schemes are presented and discussed in the following section.

A sequence of the steel projectiles with increasing impact velocity is seen in figure 5.4.

It is seen from the sequence of images, figure 5.4, that there exist a nice correlation between impact velocity, and development of plastic zone or mushroom which gradually begins to break apart as the impact velocity becomes even higher. The projectiles shows every sign of ductile fracture, as the cracks are only developed after extensive plastic deformation, and the cracks seem to be stable, i.e. the length of the crack is consistent with the impact load and thereby stress in the projectile.

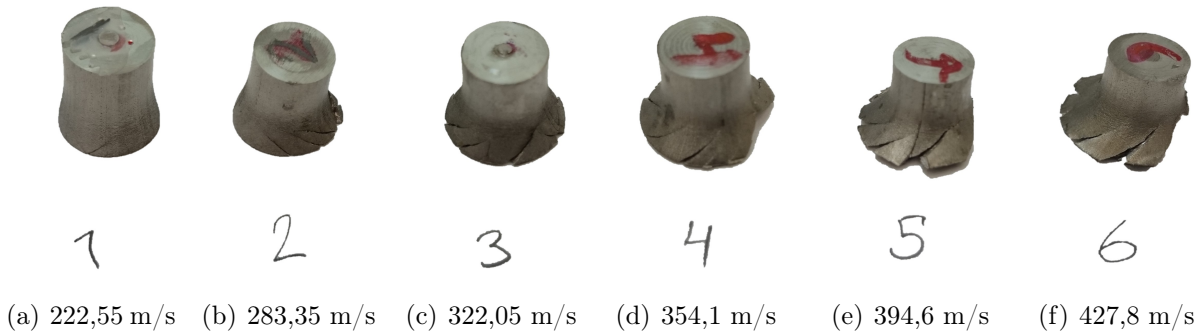


Figure 5.4: *Steel projectiles following impact on 12 mm ARMOX 500 plate.*

Similarly, a sequence of the aluminium projectiles is shown in figure 5.5.



Figure 5.5: *Aluminium projectiles following impact on 12 mm ARMOX 500 plate.*

As was the case for the steel projectiles, a nice correlation between impact velocity and the amount of deformation exists, as seen in figure 5.5. As the impact velocity is higher and the material parameters of aluminium is more pliant than for steel, the amount of deformation in the projectiles is larger.

Direct comparison of the projectiles across the materials is possible by considering figure 5.5(b) and figure 5.4(d) as the impact velocity is approximately the same, and the projectiles are not badly influenced by a high-pitched impact angle. A similar correlation between figure 5.5(c) and figure 5.4(f) exists. This is in agreement with Taylor's definition for strain, which is independent of material density. It is seen for these cases, that deformation and failure/crack formations in the 'mushroom' are very similar, and it is concluded that both materials undergo the same failure phenomenon.

As expected, the projectiles all show the characteristic mushroom-shape, i.e. a deformed frontal area which size is dependent on the velocity of impact, and a gradual reduction in area for each increment until the cross-sectional area returns to normal for the unaffected remaining part of the projectile. This is perhaps best observed in figure 5.4(c).

The other distinctive features of the deformed projectile are the crack formations. These seem to indicate that large radial stresses develop during impact, figure 5.6(a). Furthermore, the crack trajectories are rotated to an angle very close to the angle of maximum

shear stresses, the shear angle of 45° to the principal planes, in the longitudinal direction of the projectile, like a helix, figure 5.6(b). This is due to large compression stresses developing in the projectile during impact, [Meerkamm, 2014].



(a) Projectile #4 - Steel. Strike face. Guidelines implemented to help track the cracks, which indicate radial stresses. The cracks are slightly curved, like a helix, into the material, which indicate the cracks are not developed purely by radial stresses.

(b) Projectile #6 - Steel. The distinct slip bands in a trajectory similar to a helix. This indicate compression stresses.

Figure 5.6

Another distinctive feature on some of the projectiles, most notably for steel projectile #3 (fig. 5.4(c) or fig. 5.7(a)), and aluminium projectile #3 and #4 (fig. 5.5(c), 5.5(d)), is the development of a tetrahedral in 45° to the strike face for each side and a trajectory for each crack approximately perpendicular to each other. In some cases, as for the steel projectile, the crack propagation is not deep enough and a 'wedge' remain, fig. 5.7(a), and in other cases, e.g. the aluminium projectiles, the triangle is disregarded as a fragment. These crack likewise follow the shear angle, and as there always exist two perpendicular directions of maximum stress (α and β line from slip line theory, [DoITPoMS, 2016]), crack initiation has started along these for thereafter to propagate and intersect for creating the tetrahedral fragment.

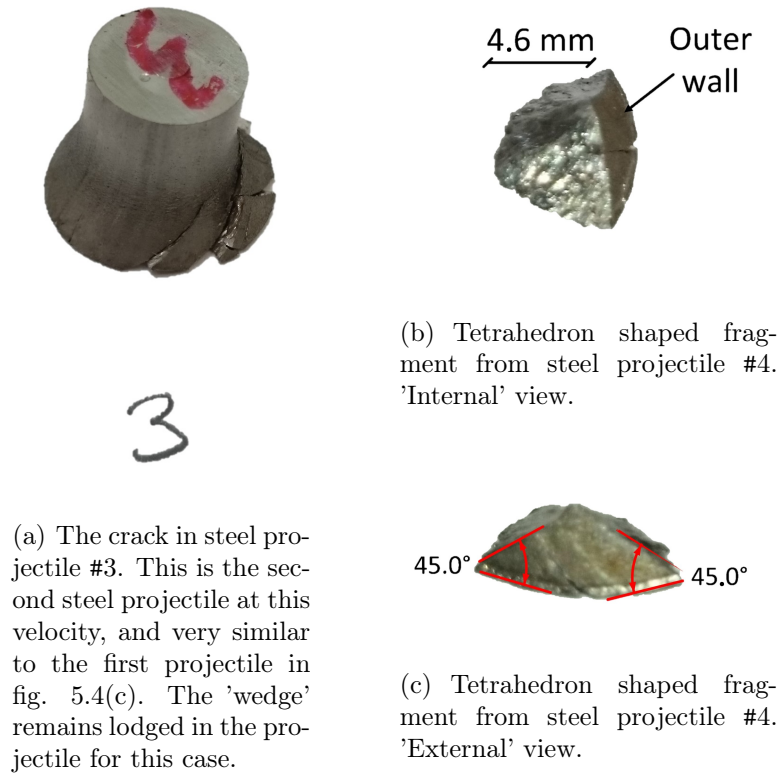


Figure 5.7

In several of the projectiles, only for steel, a perfectly straight crack in the longitudinal direction has been observed, figure 5.8. This type of crack is usually seen in rods that have been exposed to a torsional force [Meerkamm, 2014]. Analyses of video sequences of impact do not show any visible roll, as if the barrel had rifling, of the projectiles causing a torsional force when the strike face impact the target, and the tail end keeps rolling. This explanation is therefore disregarded. Another possible explanation is, that it is a case of direct shear due to an uneven impact because of unwanted pitch or yaw of the projectile. But, as seen in figure 5.8, the projectiles do not show any signs of a high-pitched or yawed impact. So, it is deemed that it is due to a weakness in the steel rod from which the projectiles are made.

Brittle impacts have not been an area of study for this project mainly because it is very complex to make an analytical model, and numerical models likewise have shown to be difficult. A brittle brass is chosen for the projectile material. Brass with a copper-zinc composition, where the zinc content is '45 % <' changes the material to BCC (β') crystal structure - a phenomena called allotropy. This type of brass is brittle for impacts at room temperature. So, a series of three brittle impacts is conducted at ≈ 213 m/s and they all show the same fracture pattern, as seen in figure 5.9, and show almost no plastic deformation before crack initiation, which is the direct opposite of the steel and aluminium projectiles. BCC crystals experience slips in their most dense packed atomic structure, i.e. 45° but it is a little bit uncertain whether that is what is seen in this case. A similar fracture is seen in the quasi-static compression test performed on the brass projectile as



(a) Projectile #5 - Steel. A straight crack in the longitudinal direction. In this case, it initiate from another crack.
 (b) Projectile #2 - Steel. Similar straight crack in the longitudinal direction. Initiated from edge, i.e. not a branch of another crack.
 (c) Projectile #4 - Steel. This crack initiate from a small chip, so something in between the two previous images.

Figure 5.8

well, appendix C. In this fracture, observing the transverse section and the fracture has an almost perfect circular shape, and observing the longitudinal section, the fracture is almost perfectly parabolic. This is a very close representation of shear band in cylindrical test specimens undergoing compression, [Odeshi et al., 2006].



(a) Brass - Impact velocity: ≈ 213 m/s.



(b) Brass - Impact velocity: 214,7 m/s. Top view.
 (c) Brass - Impact velocity: 214,7 m/s. Side view.

Figure 5.9: *Brass projectiles showing brittle impacts.*

Another impact with brass at 282,0 m/s is made. This projectile shatters in a complete projectile defeat against the 12 mm ARMOX 500 plate. The projectile is shown in figure 5.10, and the nature of this failure makes it very difficult to say anything specific.



Figure 5.10: *Brass - Impact velocity: 282,0 m/s. Complete projectile defeat, and no pattern in the fracture planes.*

Flash during impact.

During projectile impacts, an emission of light has been seen in the video sequences. This flash might be due to what is known, in general, as mechanoluminescence or more specifically fractoluminescence. Fractoluminescence is due to fracture of a crystal where each new part of the crystal is either positively or negatively charged. If the electric potential between these charges are large enough, a discharge and thereby light emission is seen, [Chmel and Shcherbakov, 2014]. Furthermore, it is understood that it should be closely linked to electromagnetic radiation likewise observed during deformation of metals.

Another and more plausible explanation is, that it simply is the ignition of metallic particle dislodged during impact and the temperature increase due to deformation, or a combination of both mechanoluminescence and ignition of particles. The flash is shown in figure 5.11 for an aluminium projectile. On these images, especially the last two, fig. 5.11(c) and 5.11(d), it indicates that it is projectile/target particles that are burning or glowing. Similar, but not as grand, the phenomena is seen for impact of steel projectiles as well. Only evidence of this on the projectiles are the increase in temperature, due to deformation, and burn marks on the strike face.

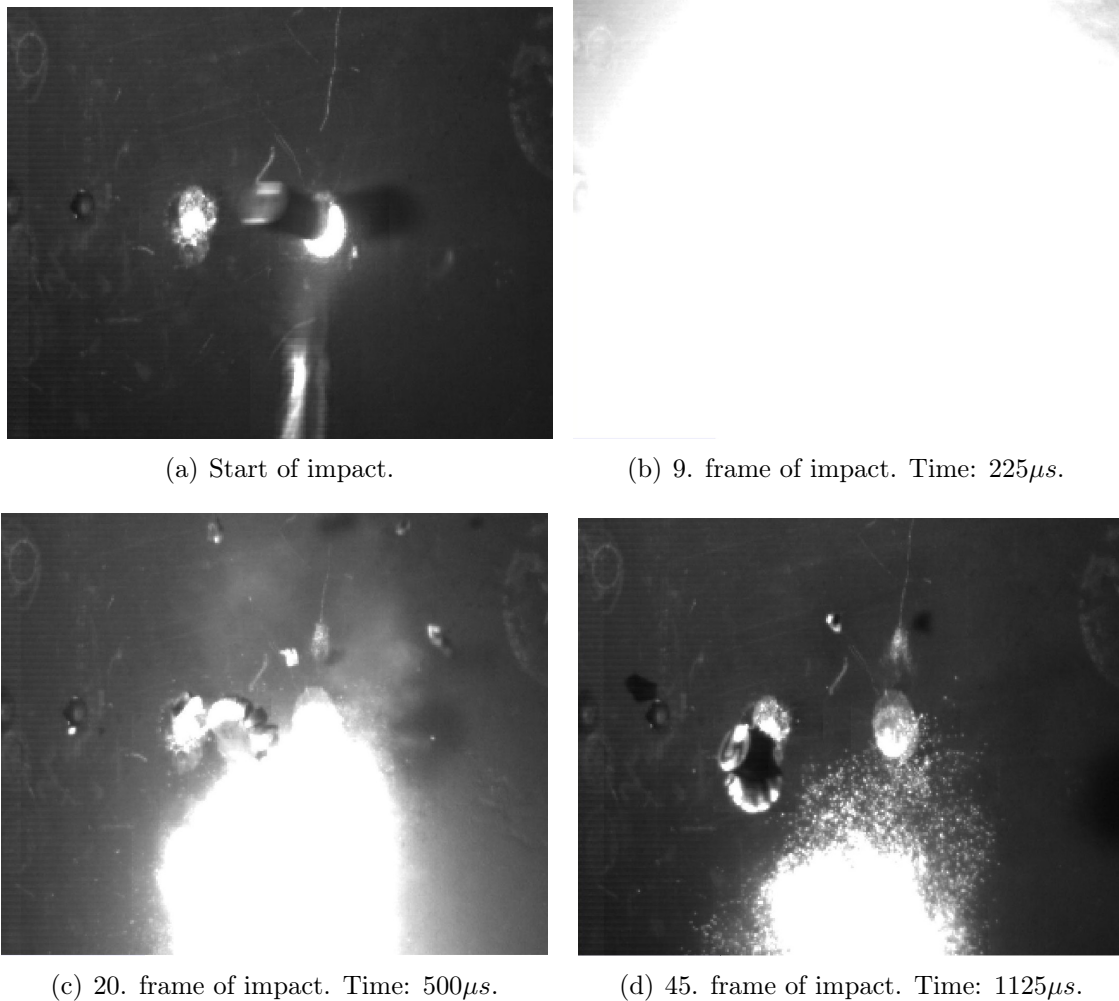


Figure 5.11: Recorded at 40000 frames per second. Projectile material: Aluminium.

5.4 Failure criteria

One of the most intricate problems in terminal ballistics are the physics underlying penetration and perforation of the target. Several penetration modes are well identified, such as petalling, plugging, spall failure and fragmentation. As the aim of this project is to analyse and study the possible failure mechanisms of the projectile, an attempt of applying a failure criterion is made.

Failure of projectiles may have different definitions, but in general failure of the projectile means losing its capability of penetration due to changes in its geometry and loss of its energy. Many possible failure modes can occur based on the projectile material behaviour under dynamic impact. Some of the failure modes can be due to brittle material behaviour, as seen in the case for the brass projectile, but the majority of the experiments show a great amount of plastic deformation in the front of the projectile, i.e. ductile behaviour.

Whatever the theory adopted, the necessary material data have to be obtained from a

simple test, like that of a uni-axial tension, pure torsion or compression test. From this, the state of stress or strain which causes the failure of the material concerned can easily be calculated, neglecting the strain hardening effects of higher strength but less ductility.

Maximum strain to failure ε_f is used in this section based on the simple compression test, appendix C. An even material is assumed, and expected for the used material, meaning the yield or proof strength in compression is equivalent to the yield/proof strength in tension. The projectile is compressed statically until failure, in the case of aluminium and brass, and until the machine limitation for steel. A crack propagation or separation in the material is considered as failure as can be seen in figure C.4 in app. C. As the test is abandoned before fracture in the case of the steel projectiles, a ε_f for the steel projectile is obtained from a monotonic tensile test in [Stephens et al., 2013], for the used steel, as follows

$$\varepsilon_f = \ln \left(\frac{A_f}{A_0} \right) = \ln \left(\frac{100}{100 - \%RA} \right) \quad (5.1)$$

where A_f, A_0 are the final and initial cross sectional area for the tested material, $\%RA$ is the critical percent reduction in area for the material.

Using [Stephens et al., 2013, table A.1] gives $\%RA = 64$ for steel 4130. Substituting this value into eq. 5.1 gives the failure strain for the steel projectile

$$\varepsilon_f^s = \ln \left(\frac{A_f}{A_0} \right) = 1.01 \quad (5.2)$$

where the superscript indicate 's' for steel.

Using the stress strain relation for the model and it is rewritten here

$$\varepsilon = \frac{\sigma - Y_D}{E_w} \quad (5.3)$$

And from eq. 3.37 the strain at the front end of the projectile is found

$$\varepsilon = \frac{\sqrt{2 \zeta \rho_p R_t c v_0} - Y_D}{E_w} \quad (5.4)$$

Rearranging this equation and replacing the strain by the failure strain gives the critical impact velocity

$$v_{crit} = \frac{Y_D^2 + E_w^2 \varepsilon_f^2 + 2 Y_D E_w \varepsilon_f}{2 \zeta \rho_p R_t c} \quad (5.5)$$

The dynamic yield strength is proportional to the impact velocity as seen before, thus the mean value of $Y_D = 1,74$ GPa is used in eq. 5.5 for the steel and $Y_D = 0,74$ GPa for the aluminium projectiles.

Hereby, the critical impact velocity for the steel projectile is determined as

$$v_{crit}^s = 496 \frac{\text{m}}{\text{s}}$$

which is a pretty serious overestimation of the velocity at which failure or crack propagation is noticed in the experiments, i.e. an optimistic assessment is for projectile #3 or 322 m/s.

The aluminium projectile is also subjected to a compression test, the final cross sectional area at fracture is measured and the failure strain is obtained is

$$\varepsilon_f^{al} = 0,74$$

Substituting this value into eq. 5.5 gives the critical velocity for the aluminium projectiles

$$v_{crit}^{al} = 374 \frac{\text{m}}{\text{s}}$$

In this case, the overestimation is not as bad, as observations of the projectiles suggest initiation of crack propagation between projectile #1 and #2, i.e an optimistic assessment of 330 m/s. An additional shot of 305 m/s with the aluminium at a perfectly normal impact showed no cracks, as seen in the annex videos. Additional tests need to be conducted, but time constraints rule this out.

The relative poor correlation for steel is probably because the data is obtained from a tensile test from [Stephens et al., 2013], where the aluminium is based on the compression material test data performed by the group.

Alternatively the failure strain can be taken directly from experimental measurements. This demands a number of impact tests with relatively short steps between impact velocities. Defining the failure strain for a projectile can be consider as a material parameter and thus can be used as a criterion even when impacting different targets.

Since the kinetic energy and work done by the projectile are the basic principles used in the analytical solutions, a failure criterion based on plastic strain energy density is probably the most accurate criterion. However, a dynamic compression stress strain curve is needed for conducting the critical strain energy, where it is found that the dynamic behavior of material under compression can be quiet different from that for the static compression.

CHAPTER 6

COMPARISON OF THE ANALYTICAL, NUMERICAL, AND EXPERIMENTAL RESULTS

The following chapter includes a comparison of the findings obtained by the analytical, numerical models, and the experiment work. Furthermore, an attempt of explaining the discrepancies in the findings is made. The chapter is concluded by a section where the observations made are treated, and the components influencing projectile defeat are highlighted.

The models simulate impact of a blunted cylinder, of aluminium and steel, on an 12 mm Quardian 500 plate. The brass projectiles cannot be used in these models due to the brittle and distinct fracture. The results are compared against experimentally obtained results for near identical cases. The dynamic yield strength used in the model for the steel projectile is the one derived in sec. 3.5 which is proportional to the impact speed, the other material parameters are listed in table 5.1.

6.1 Model derived in section 3.3 and Experiments

The results for the deformations obtained by the model derived in 3.3 are shown here and compared to the results obtained experimentally. Table 6.1 shows the final length for the steel projectile obtained by the model and the deviation from the experimental data.

Table 6.1 shows the deviation from the experimental data.

Steel/Quardian				
		Model. [mm]	Exp. [mm]	Deviation
222,6	m/s	13,20	13,50	-0,30
283,4	m/s	12,60	12,84	-0,24
322,1	m/s	12,1	11,93	0,17
350,7	m/s	11,8	11,33	0,47
394,6	m/s	11,10	10,85	0,25
427,7	m/s	10,60	10,40	0,20

Table 6.1: *The final projectile length obtained by the derived model and experimentally for the cylindrical steel projectiles striking against a 12 mm Quardian plate, the initial projectile length is 15,2 mm.*

It seems that the predicted results are shifted by about 1 mm higher than the experimental observations. As mentioned in 3.3 the final length can be obtained in more than one way and the accuracy depends on the accuracy in the material parameters used in the calculations.

The ratio between final and initial projectile diameter obtained by the model and experiments is listed for each impact velocity.

Steel/Quardian				
		Model. $\left(\frac{D_1}{D_0}\right)$	Exp. $\left(\frac{D_1}{D_0}\right)$	Deviation
222,55	m/s	1,31	1,29	0,02
283,35	m/s	1,43	1,32	0,11
322,05	m/s	1,50	1,34	0,16

Table 6.2: *The ratio between maximum and initial diameter obtained by the derived model and experimentally for the cylindrical steel projectiles striking against a 12 mm Quardian plate, the initial projectile diameter $D_0 = 10$ mm.*

Results are only listed for the three projectile without fracture, i.e. the three lowest impact velocities. The other projectiles diameters deviates because of fracture. It is seen from table 6.2 that the deviation from the experiments increases as the impact velocity increases, which could be due to the cracks growth and voids created in the front face which increase the measured cross sectional area.

The penetration depths observed in experiments are too small to be measured. The models predicts a penetration depth of 0,2 and 0,7 mm for the lowest and highest impact velocity, respectively.

The aluminium projectile results are also compared with the experimental data as seen in table 6.3. The maximum diameter of the projectile couldn't be measured because of fracture of the projectile even for the lowest impact velocity, thus only a comparison regarding the final length of the projectile is shown here. The material parameters from table 5.1 are used for the aluminium projectile, except for the dynamic yield strength which is obtained by the derived equations in sec. 3.5.

Aluminium/Quardian				
		Model. [mm]	Exp. [mm]	Deviation
291,1	m/s	12,4	12,85	-0,45
368,1	m/s	11,50	11,61	-0,11
416,2	m/s	10,80	10,55	0,25
452,5	m/s	10,20	9,55	0,65
509,7	m/s	9,20	8,85	0,35
529,5	m/s	8,80	7,80	1,00

Table 6.3: *The final projectile length obtained by the derived model and experimentally for the cylindrical aluminium projectiles striking against a 12 mm Quardian plate, the initial projectile length is 15 mm.*

As explained in chapter 5, the aluminium projectiles are skewed in all tests which makes it really difficult to get precise measurements out of them, however the results are still close.

6.2 Modified den Reijer Model and Experiments

The following section presents the analytical obtained results using the modified model of den Reijer, and compare it to the experimental findings.

The results of the model compared against the experimental finding for steel projectiles are shown in table 6.4.

Steel/Quardian				
		Mdl. [mm]	Exp. [mm]	Deviation
222,6	m/s	13,1	13,5	-0,4
283,4	m/s	12,8	12,84	-0,04
322,1	m/s	12,6	11,93	0.67
354,1	m/s	12,4	11,35	0.95
394,6	m/s	12,2	10,85	1,35
427,8	m/s	12,0	10,4	1,6

Table 6.4: *Comparison of model results, and experimental results for the cylindrical steel projectiles striking against a 12 mm Quardian plate.*

It is seen that there exist an acceptable correlation between the residual length of the projectile after test firing, and the residual length predicted by the model, especially in the low-velocity impacts. It is worth noting, that even slight changes in the dynamic yield strength moves the predicted length a lot.

A similar comparison for the aluminium projectiles is made using the same model and adjusting the material parameters for aluminium.

Aluminium/Quardian				
		Mdl. [mm]	Exp. [mm]	Deviation
291,1	m/s	12,9	12,85	0,05
368,1	m/s	12,5	11,61	0,89
416,2	m/s	12,3	10,55	1,75
452,5	m/s	12,1	9,55	2,55
509,7	m/s	11,7	8,85	2,85
529,5	m/s	11,6	7,80	3,8

Table 6.5: *Comparison of model results, and experimental results for the cylindrical aluminium projectiles striking against a 12 mm Quardian plate.*

The correlation between experiments and model is not great. The models seriously underestimate the amount of deformation in the projectiles, and it can be concluded that the physical fit of the front-end deceleration during the plastic deformation phase as described in sec. 3.4 is insufficient or wrong. It seems, that the model predicts small changes in residual length for each velocity increment, when in fact the projectiles in the experiments

experience a rather large change in length, i.e the model underestimate the momentum and thereby energy of the projectile? Another explanation might be the material parameters used, but as seen further down, a good correlation of model and experiments have been obtained using the second model. That the aluminium projectiles are very skew due to a high-pitch impact do not ease the measurements of the total amount of deformation, and some of the discrepancy between model and experiments might be located here.

A general conclusion for the modified den Reijer model is, that it is insufficient to use this model for projectile deformation modelling. This is not implying that the original den Reijer model is bad, it is just the modifications made to use in a projectile-metal impact, instead of the intended projectile-ceramic impact, that is the reason for this. In the following section, the second model, developed during these studies, are compared to the experimental findings. Attempts of a better model have been made, but is either non-physical or worse.

6.3 Hydrocode and Experiments

The following section presents the results obtained from hydrocode simulations, and compare it to the experimental findings.

The results from the hydrocode and the experiments are showed in table 6.6 for the steel projectiles and table 6.7 for the aluminium projectiles, along with the deviation of the two.

As is seen from table 6.6 the largest deviation is 0,34 mm for the impact at 350,65 m/s, this equates to a max 3% deviation. This can in most cases of impact ballistic be regarded as a exact correlation.

Steel/Armox model				
		Hyd. [mm]	Exp. [mm]	Deviation
222,6	m/s	13,58	13,50	0,08
283,4	m/s	12,72	12,84	-0,12
322,1	m/s	12,13	11,93	0,20
350,7	m/s	11,67	11,33	0,34
394,6	m/s	10,95	10,85	0,10
427,7	m/s	10,40	10,40	0,00

Table 6.6: Comparison of hydrocode results, and experimental results for the cylindrical steel projectiles striking against a 12 mm Guardian plate.

As is seen in table 6.7 the deviations for aluminium are of greater magnitude than for steel. It is also noted that the deviation gets higher with the velocity. This is more obvious in figure 6.2 where the results are plotted. It is more obvious here that experimental results and results from hydrocode have different slopes. This can be due to multiple factors, the material model is either unfit for this specific alloy or inaccurate at the tested strain rates, another factor may be erosion and fracture failure in the experimental results. As

mentioned in chapter 4, the simulations are run without numeric erosion and failure, there are consequently no mass loss in the simulations. But as is seen in table 5.3 the projectiles experience a significant mass loss at higher velocities. A combination is also a possibility and the most likely.

Aluminium/Armox model				
		Hyd. [mm]	Exp. [mm]	Deviation
291,1	m/s	12,56	12,85	-0,29
368,1	m/s	11,54	11,61	-0,07
416,2	m/s	10,83	10,55	0,28
452,5	m/s	10,28	9,55	0,73
509,7	m/s	9,40	8,85	0,55
529,5	m/s	9,10	7,80	1,30

Table 6.7: Comparison of hydrocode results, and experimental results for the cylindrical aluminium projectiles striking against a 12 mm Quardian plate.

It can be concluded that hydrocode yields accurate results for these kinds of impacts. More accurate material model data and use of element failure and erosion may give better results. But at the investigated stain rates and materials there are not much improvement to gain.

6.4 Graphical comparison of results

Results from the two models, hydrocode and experiments are combined in figure 6.1 for steel projectiles and figure 6.2 for aluminium projectiles.

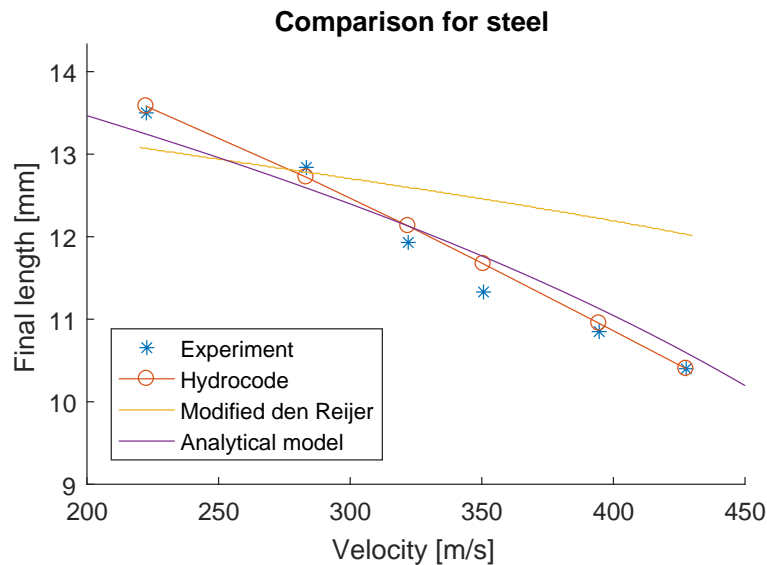


Figure 6.1: Comparison of all results for steel projectiles.

It is seen that for steel it is hydrocode that yields the closest fit to the experimental data, but the derived analytical model is very close as well. The problem with the modified den Reijer model is obvious in this figure, as the slope is flatter than reality and it therefore yields a far to conservative estimate of deformation for each velocity increment. This means it underestimate the residual length for velocities under 280 m/s and overestimate for higher velocities.

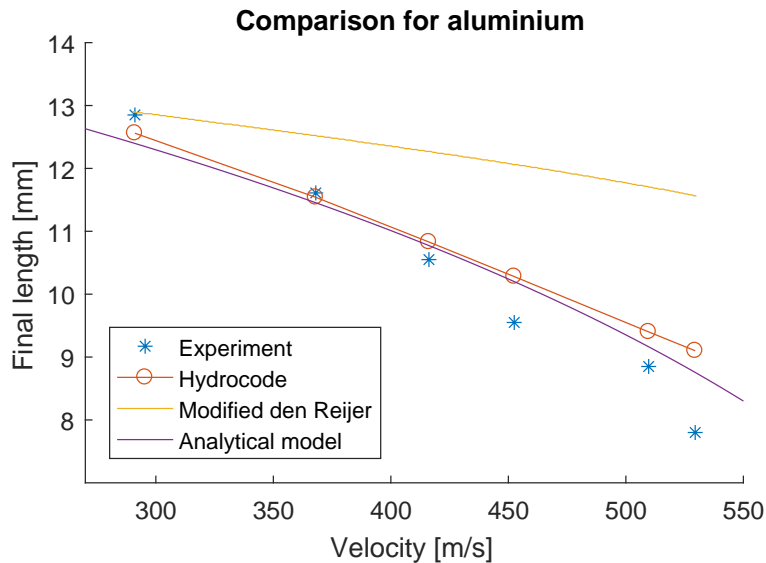


Figure 6.2: Comparison of all results for aluminium projectiles.

In figure 6.2 it is seen that the analytical model yields the closest fit at velocities in the higher range, as both the analytical model and the numerical model in hydrocode yield a very nice correlation with the experiments. Modified den Reijer again shows the same tendency as for steel but overestimates for the entire range except for the lowest velocity where it yields a near perfect fit.

An additional observation is, that none of the models predict mass loss, as the impact velocity is too low or it is not implemented in the model. This is not the case in the experimental results, table 5.3, as great amount of mass loss is observed. The loss of mass, as is furthermore seen on the images of projectiles in chapter 5 indicate, that the primary loss of mass is when the plastic deformation, or mushroom shape, in the projectiles become to great, the crack becomes to deep and some of the material breaks away. This is further enhanced, when a pitched or yawed impact happens. This phenomena has not been possible to implement in the models within the given project boundaries.

CHAPTER 7

CONCLUSION

This project has dealt with investigation of terminal ballistics of metal projectiles impacting metal targets. An analytical model is developed to model the projectile deformation as well as a modification of an existing model. A commercial numerical program is also applied and all methods are compared with experimental results.

An analytical model for the interacting effects between projectile and target is developed. The model is used to determine the retarding force on the projectile by the target. Many existing models treating projectiles assume rigid target, but it is shown that the effects from the target are non-negligible. These effects have been incorporated. An expression for the critical impact velocity for projectile deformation has likewise been developed.

An analytical model for deformation of projectile and penetration depth was developed. The model is able to determine the reduction in length and the profile of the deformation, as well as depth of penetration. The model is developed for short cylindrical projectiles with a blunt end, known as fragment simulating projectiles (FSP), for normal impact. The model makes use of few assumptions from long rod penetrators, but all assumptions are deemed acceptable. The model is verified against experiments and show good correlation, see section 3.3.3. The model can easily be modified for different nose shapes such as spherical or ogive for better representation of projectiles used by tanks, rifles etc.

The analytical model above yields a very good correlation with the experimental and numerical findings, and maximum deviation from the experiments with regards to the residual projectile length is 0,47 mm or 4,4% for steel and 1,0 mm or 12,8% for aluminium. Furthermore, these deviations can probably be prescribed the experiments, see more in chapter 6.

A model developed by [den Reijer, 1991] is modified to accommodate metal targets. The modifications involves omitting the dwelling phase as this is not observed for steel targets and a new equation for the deceleration of the front end of the projectile. This include an approximation of the initial penetration velocity into the steel making use of long-rod penetration theory – sufficient proof of the validity of this in short projectiles has been obtained.

The correlation with the experiments and the numerical models are poor for this model. The model simply underpredicts the amount of deformation in the projectile, for each higher velocity increment. The largest deviation is 15,4% for steel, and 48% for aluminium. It is strongly suspected, that it is due to the modified deceleration term for the projectile front-end, but a better, and still physical valid term, has not been found.

A commercial program for simulating impact and high speed transient problems is applied for the investigated case. The used program is a hydrocode from ANSYS INC.. To analyse the impact case the Lagrange method is applied. A validations study confirms the validity for the use of axisymmetry. A convergence study is also conducted to validate convergence of deformation and to determine the optimal mesh size. The simulations are run as pure plastic deformation problems without element failure and erosion.

The comparison showed that the hydrocode yield results very close to those obtained from experiments, a maximum deviation of 3% for steel and 16,6% for the aluminium. In this case, some of the deviation is likely explained by the experiments once again, but it is also noted, that the hydrocode begins to underestimate the deformation as the velocity increases. From observations of the deformed projectiles, it is concluded that this is due to the absences of failure and erosion in the simulations.

Experiments are conducted in the terminal ballistic test facility, where projectiles of steel, aluminium and brass are shot at an armour plate of Guardian 500. The projectiles are shaped as cylinders with a length of 15 mm and a diameter of 10 mm, representing FSP's commonly experienced in cases of IED attacks. The projectiles are shot at velocities from 210 m/s to 530 m/s, and the limits are governed by the experimental equipment, and the projectiles. Each shot is taken twice to negate outliers. The impacts are documented on a high speed camera and fragments are collected for observations along with measurements of residual length after impact. It has proven to be a challenge achieving perfect normal impacts, and skew projectiles influencing the measurements have been a problem, especially the lighter aluminium projectiles.

Mainly ductile behaviour of the steel and aluminium projectiles are observed, with some degree of material loss due to either deep crack propagation or highly pitched/yawed impacts. The brass projectiles show brittle behaviour. An attempt of explaining these observations is made in the experimental chapter, chapter 5.

The range the experiments covered with respect to velocity, material, projectile dimensions and repetitions are limited due to equipment and time constraints. A wider range of experiments are desired but not achieved.

The preceding work has resulted in the following;

- The resistance of the target against penetration is now determinable independent of the shape of the projectile front-end.
- An analytical method of determining the dynamic yield strength of the projectile material is obtained, based on previous works.
- Deformations, hereby stresses and strains, in the projectile can be obtained analytically.
- Depth of penetration into the target is obtainable analytically.
- Mass erosion of projectile for impact above the plastic wave velocity in the material is determinable analytically, but not validated due to equipment limitations.

Furthermore, the following observations are made;

- The projectile ballistic characteristics depend on the target resistance R_t , the ratio of density, and the dynamic yield strength of the projectile material.
- An axisymmetric analysis is applicable for axisymmetric problems where plasticity is governing deformations.
- The concept of a critical strain to failure is shown to be inadequate for the purpose of predicting ballistic failure.

BIBLIOGRAPHY

- ANSYS Inc.. 2016. *ANSYS Release 17.2 Documentation*. www.ansys.com: ANSYS Inc. 47
- Børvik, T., S. Dey, and A. Clausen. 2009. Perforation resistance of five different high-strength steel plates subjected to small-arms projectiles. *International Journal of Impact Engineering* 36(7), 948 – 964. 6
- Chmel, A. and I. Shcherbakov. 2014. Fractoluminescence from brittle and ductile homogeneous solids. *Journal of Luminescence* 153, 85 – 89. 64
- Chocron, S., C. E. A. Jr., D. J. Grosch, and C. H. Popelar. 2001. Impact of the 7.62-mm APM2 projectile against the edge of a metallic target. *International Journal of Impact Engineering* 25(5), 423 – 437. 9
- Composhield. 2016. <http://www.composhield.com/>. Accessed: 2016-09-22. 1
- Copper Alloys Ltd. 2016. <http://www.copperalloys.net/alloys/htb3.php>. Accessed: 2016-12-10. Brass material data. 94
- Defence Procurement Agency. 2002. Armour Plate, Steel (3-160 mm) [DEF STAN 95-24/3]. <ftp://ftp.iks-jena.de/mitarb/lutz/standards/dstan/95/024/00000200.pdf>. 10
- den Reijer, P. C.. 1991, 11. *Impact on Ceramic Faced Armour*. Ph. D. thesis, Technische Universiteit Delft. 3, 33, 34, 35, 36, 37, 38, 40, 44, 75, 83, 84, 85, 86, 87, 88
- Deníz, T.. 2010. Ballistic Penetration of Hardened Steel Plates. Master's thesis, Middle East Technical University. 6
- DoITPoMS. 2016. http://www.doitpoms.ac.uk/tlplib/metal-forming-3/slip_line_field.php. DoITPoMS (Dissemination of IT for the Promotion of Materials Science) University of Cambridge. Accessed: 2016-12-09. 61
- Florence, A. L. and T. J. Ahrens. 1967. Interaction of Projectiles and Composite Armor. *AMRA CR 67-05(F)*. 35, 83
- Hawkyard, J. B., D. Eaton, and W. Johnson. 1968. The mean dynamic yield strength of copper and low carbon steel at elevated temperatures from measurements of the 'Mashrooming' of flat-ended projectiles. 10, 929 – 948. 32, 40
- Hazell, P. J.. 2015. *Armour: Materials, Theory, and Design*. ISBN: 978-148-22-3830-3. CRC Press. 6, 8, 9, 11, 12
- Interlloy. 2016. <http://www.interlloy.com.au/our-products/high-tensile-steels/4340-high-tensile-steel/>. Accessed: 2016-12-10. Steel material data. 92

BIBLIOGRAPHY

- Johnson, G. R. and W. H. Cook. 1983. A constitutive model and data for metals subjected to large strains, high strain rates and high temperatures. *Proceedings of the 7th International Symposium on Ballistic*, 541 – 547. 47, 53
- Khedmati, M.. 2000. Ultimate strength of ship structural members and systems considering local pressure loads. *Graduate School of Engineering, Hiroshima University*. 96
- Lou, J., Y. Zhang, Z. Wang, T. Hong, X. Zhang, and S. Zhang. 2014. Long-rod penetration: the transition zone between rigid and hydrodynamic penetration modes. *Defence Technology* 10(2), 239 – 244. 28th International Symposium on Ballistics. 36, 84, 86
- Manjit Singh, D., R. Sood, R. Gupta, and P. Kumar. 2008. Dynamic Yield Strength of Mild Steel under Impact Loading. *Defence Science Journal*. 44
- Meerkamm, H.. 2014. *Technical Pocket Guide*. Schaeffler Technologies GmbH. 61, 62
- NagarajaRao, N., M. Lohrmann, , and L. Tall. 1966. Effect of strain rate on the yield stress of structural steel. *ASTM Journal of Materials* 1. 39
- NLMK Clabecq. 2016. http://www.aficor.ch/wordpress/wp-content/uploads/2015/11/en_Quard500.pdf. Accessed: 2016-12-10. Quardian material data. 57, 91
- Odeshi, A., S. Al-ameeri, S. Mirfakhraei, F. Yazdani, and M. Bassim. 2006. Deformation and failure mechanism in {AISI} 4340 steel under ballistic impact. *Theoretical and Applied Fracture Mechanics* 45(1), 18 – 24. 63
- Orphal, D. and C. Anderson. 2006. The dependence of penetration velocity on impact velocity. *International Journal of Impact Engineering* 33(1–12), 546 – 554. Hypervelocity Impact Proceedings of the 2005 Symposium. 43
- Rosenberg, Z. and E. Dekel. 2012. *Terminal Ballistics*. ISBN: 978-981-10-0395-0. Springer. 5, 6, 7, 16, 20, 21, 22, 23, 35, 43, 44
- Rosenberg, Z. and J. Tsaliah. 1990. Applying Tate’s Model for the Interaction of Long Rod Projectiles with Ceramic Targets. *Journal of Impact Engineering* 9. 39, 40
- Schneider, S., S. G. Schneider, H. M. d. Silva, and C. d. Moura Neto. 2005, 12. Study of the non-linear stress-strain behavior in Ti-Nb-Zr alloys. *Materials Research* 8, 435 – 438. 95
- Scientific Academic Publishing. 2013. <http://article.sapub.org/10.5923.s.cmaterials.201310.03.html#Ref>. Accessed: 2016-11-22. 12
- SSAB Oxelösund AB. 2007, 10. *Data Sheet: ARMOX 500T*. www.ssabox.com: SSAB Oxelösund AB. 49, 57, 99
- Steinberg, D. J.. 1991. *Equation of state and strength properties of selected materials*. Lawrence Livermore National Laboratory. 53

- Stephens, R. I., A. Fatmi, R. R. Stephens, and H. O. Fuchs. 2013. *Metal Fatigue In Engineering*. ISBN: 978-81-265-3921-5. John Wiley & Sons Inc. 66, 67
- Tabor, D.. 2000. *The Hardness of Metals*. ISBN: 9780198507765. Oxford University Press. 39
- Tate, A.. 1967. A Theory for the Deceleration of Long Rods after Impact. *Journal of Mechanical Physics Solids* 15. 35, 39
- Tate, A.. 1977. A possible explanation for the hydrodynamic transition in high speed impact. *International Journal of Mechanical Sciences* 19(2), 121 – 123. 83, 84
- Taylor, G.. 1947. The use of flat-ended projectiles for determining dynamic yield stress. *Proceedings of the Royal Society of London. Series A, Mathematical and Physical Sciences* 194(1038), 289–299. 32, 39, 40, 42
- Wilkins, M. L. et al.. 1968. Third progress report of light armor program. *UCRL-50460, Lawrence Livermore Laboratory, Livermore, CA*. 33
- Włodarczyk, E., A. Jackowski, and M. Sarzyński. 2012. Dynamic behaviour of a metallic cylinder striking a rigid target. *Biuletyn Wojskowej Akademii Technicznej Vol. 61, nr 4*, 75–91. 32
- Woodward, R. L.. 1990. A Simple One-Dimensional Approach to Modelling Ceramic Composite Armour Defeat. *International Journal of Impact Engineering* 9(4), 455 – 474. 9
- Zukas, J. A. (Ed.). 2004. *Introduction to Hydrocodes*. ISBN-13: 978-0080443485. Elsevier Science. 45

NOMENCLATURE

Latin		Greek	
<i>a</i>	deceleration	δ	distance from interface to plastic wave
A_0	initial cross-section area	ϵ	strains
<i>b</i>	penetration step length	$\dot{\epsilon}$	strain rate
<i>c</i>	wave speed	ζ	density ratio
d_0	initial diameter	ρ_t	target density
dx	penetration increment	σ_y	static yield/proof strength
<i>E</i>	modulus of elasticity	σ_{hyd}	hydrostatic pressure
E_I	energy consumption (interia)		
E_R	energy consumption (resistance)		
E_w	linear strain hardening modulus		
<i>F</i>	retarding force		
F_s	shear force	-	Miscellaneous designation of 'mean'
<i>I</i>	momentum		
<i>k</i>	kinetic energy		
<i>K</i>	bulk modulus		
L_0	intial length of projectile		
<i>m</i>	mass		
m_p	mass (projectile)		
<i>P</i>	penetration depth		
<i>r</i>	radius		
R_t	retarding pressure		
R_{ts}	retarding pressure (shear)		
<i>t</i>	time		
<i>x</i>	distance (penetration)		
<i>u</i>	speed		
u_p	strain energy density		
u_{ela}	elastic wave velocity		
u_{plas}	plastic wave velocity		
<i>U</i>	strain energy		
<i>v</i>	velocity (instantaneous)		
v_0	initial impact velocity		
v_d	threshold velocity		
v_I	critical impact velocity (inertia)		
<i>V</i>	volume		
<i>W</i>	work		
W_t	work (shear)		
\dot{x}_m	mean penetration velocity		
Y_D	dynamic yield strength (projectile)		
Y_{Dt}	dynamic yield strength (target)		

APPENDIX A

MODEL BY DEN REIJER IN A MODIFIED VERSION

The following appendix chapter contains the additional explanations for the modified den Reijer model, [den Reijer, 1991]. Some repetition from the report exists, as an attempt of making this appendix chapter and the report section standalone is made.

Projectile model

The projectile response when impacting the armour is described in three phases. A phase where the projectile undergoes mass erosion, i.e. the projectile front disintegrates. This is followed by a phase in which the projectile deforms to a mushroom-like shape which is a transition stage between the mass erosion phase and the last phase in which the projectile is rigid and defeats or is defeated by the armour.

Erosion phase:

At a high velocity, a ductile material striking an armour plate spatters or flow out parallel to the armour surface in an erosion mechanism implying that the material physically separates from the projectile and therefore no longer contributes to the momentum of the projectile, [Florence and Ahrens, 1967]. In actual fact, as the projectile to a certain degree is brittle this may happen in chunks but at the time of development of the model, the physics for this were not developed and the projectile erosion is therefore governed by the plastic flow, [den Reijer, 1991]. This is adopted in this present work.

At a time after impact, consider the eroding projectile of length, L , cross-section, A_0 and velocity, v , penetrating the armour at a velocity \dot{x} . The rear-end of the projectile is moving towards the armour, and at some point it encounters a 'standing plastic wave', i.e. a force, velocity and cross-section that are stationary relative to the projectile/armour interface, [den Reijer, 1991]. The relative plastic wave speed to the moving tail is

$$c = (v - \dot{x}) \tag{A.1}$$

When the projectile passes this wave front, it undergoes an increase of the cross-section to A , and a decrease in velocity to v' .

The distance, δ , between the plastic wave and the projectile/armour interface is assumed to be very small ($\delta \ll \sqrt{A_0}$), and the material is assumed to flow away laterally after passing the plastic wave as seen in figure A.1, [den Reijer, 1991].

This erosion continues for as long as the velocity of the rear-end of the projectile relative to the interface ($v - \dot{x}$) exceeds the velocity of which plastic deformation propagates, u_{plas} . The explanation for this criteria is given by [Tate, 1977] and is defined as the hydrodynamic transition velocity. It is found, that this velocity depends on the relative rate of rod erosion, i.e. $v - \dot{x}$, and the plastic wave propagation u_{plas} , by using the theory of dynamic

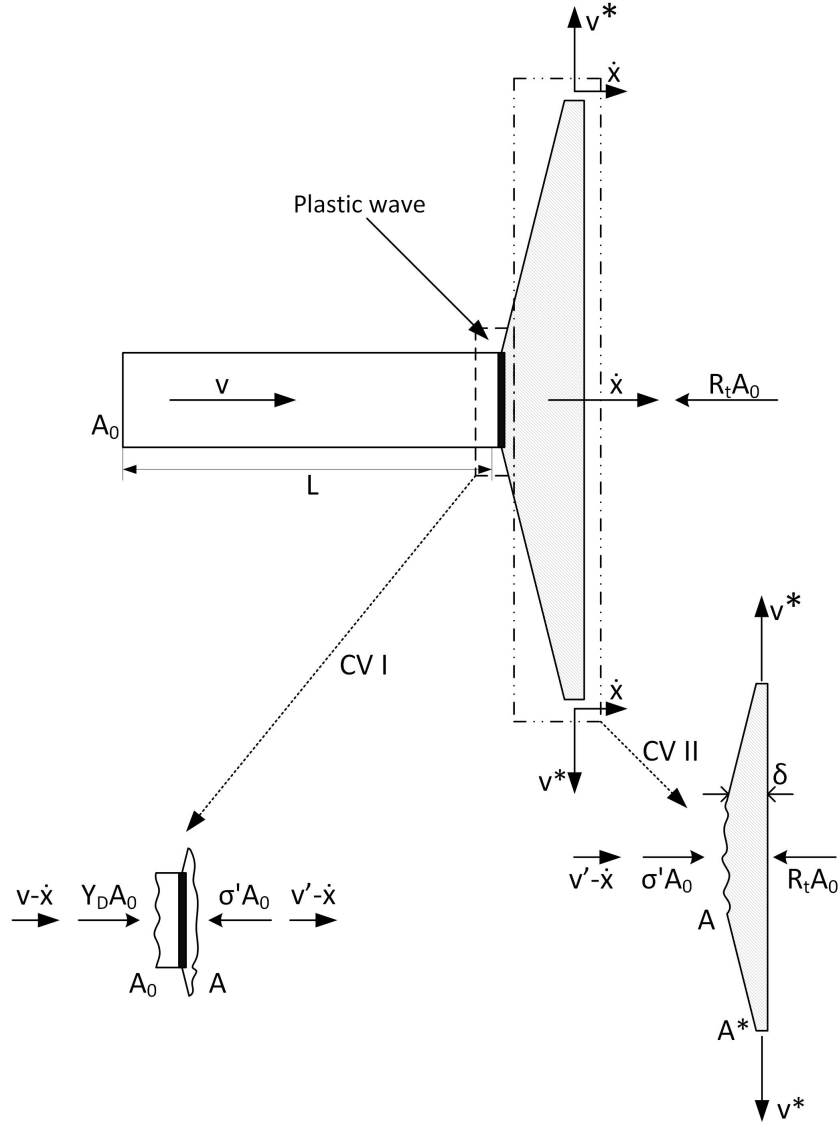


Figure A.1: *Erosion phase and governing parameters. From den Reijer [1991].*

yield strength of target and projectile along with the linear strain hardening modulus of the projectile and the modified Bernoulli equation, [Tate, 1977], [Lou et al., 2014].

First consider the plastic wave, CV I in fig. A.1, and apply the equation of continuity across the wave

$$(v - \dot{x}) A_0 = (v' - \dot{x}) A \quad (\text{A.2})$$

There is no change of momentum across the plastic wave

$$\rho_p (v - \dot{x}) v A_0 - \rho_p (v' - \dot{x}) v' A + Y_D A_0 - \sigma' A_0 = 0 \quad (\text{A.3})$$

where ρ_p is the projectile material density, Y_D is the dynamic yield strength of the projectile material, and $\sigma' A_0$ is the force acting on the right hand side of CV I in figure A.1.

Using eq. A.2 and eq. A.3 can be rewritten as

$$\rho_p (v - \dot{x}) v - \rho_p (v - \dot{x}) v' + Y_D - \sigma' = 0 \quad (\text{A.4})$$

The projectile material between the plastic wave and the armour, CV II in fig. A.1, is considered. Relative to the projectile/armour interface, the plastic wave is stationary. The projectile material is assumed incompressible and conservation of mass then yields

$$\rho_p (v' - \dot{x}) A = \rho_p A^* v^* \quad (\text{A.5})$$

where v^* is the velocity of the material flowing parallel to the armour surface, and A^* is the corresponding area of flowing material.

As the plastic wave is assumed to be a short distance, δ , from the projectile/armour interface, the momentum of the projectile material inside CV II is neglected when equating the momentum fluxes and the forces acting on the control volume, [den Reijer, 1991].

$$\rho_p A (v' - \dot{x}) v' - \rho_p A^* v^* \dot{x} + \sigma' A_0 - R_t A_0 = 0 \quad (\text{A.6})$$

Using eq. A.5, and eq. A.6 is rewritten as

$$\rho_p A (v' - \dot{x}) v' - \rho_p A (v' - \dot{x}) \dot{x} + \sigma' A_0 - R_t A_0 = 0 \quad (\text{A.7})$$

Substitution of σ' based on eq. A.4 and using eq. A.2 yields

$$\rho_p (v - \dot{x}) v - \rho_p (v - \dot{x}) \dot{x} + Y_D = R_t \quad (\text{A.8})$$

or

$$\rho_p (v - \dot{x})^2 + Y_D = R_t \quad (\text{A.9})$$

where R_t is the resistance pressure the metallic plate exerts on the projectile during penetration.

While the projectile erodes, the deceleration of its tail-end is govern by the dynamic yield strength of the material as

$$\frac{dv}{dt} = -\frac{Y_D}{\rho_p L} \quad (\text{A.10})$$

where L is the present length of the projectile.

The final equation for this phase is to determine the rate of erosion, i.e. the reduction in projectile length due to erosion. This is dependent on the relative velocity of the plastic wave compared to the moving tail-end of the projectile. This velocity is define in eq. A.1 and therefore

$$\frac{dL}{dt} = -(v - \dot{x}) \quad (\text{A.11})$$

this equation can be rewritten for the specific length of the projectile after erosion as;

$$\begin{aligned}
 dL &= -(v - \dot{x}) dt && \Rightarrow \\
 \int_{L_0}^{L_{ero}} dL &= \int_0^t -(v - \dot{x}) dt && \Rightarrow \\
 L_{ero} - L_0 &= -(v - \dot{x}) t && \Rightarrow \\
 L_{ero} &= L_0 - (v - \dot{x}) t && (A.12)
 \end{aligned}$$

and this concludes the erosion phase, [den Reijer, 1991].

Mushrooming phase:

In this phase, the relative velocity of the projectile, $v - \dot{x}$, has fallen below the hydrodynamic transition velocity, i.e the velocity of the plastic wave u_{plas} , meaning the relative displacement between the tail-end of the projectile and the interface is accommodated by plastic deformation of the projectile known as mushrooming. The velocity is still higher than the critical rigid velocity though, [Lou et al., 2014]. This means, that erosion of the projectile stops, [den Reijer, 1991]. The plastic wave moves towards the tail-end of the projectile resulting in plastic deformation of the projectile material it passes. The model assumes the velocity, v , of the tail-end, while the deformed mushroomed section has the velocity \dot{x} . The situation is sketched in figure A.2.

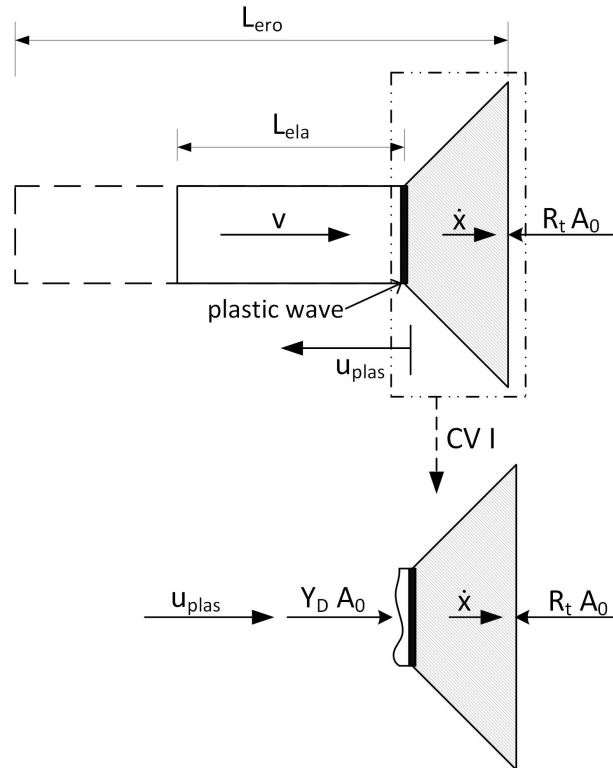


Figure A.2: Mushrooming phase and governing parameters. From den Reijer [1991].

Consider CV I in figure A.2. The change in momentum of this volume is

$$\frac{dI}{dt} = \rho_p A_0 u_{plas} v + Y_D A_0 - R_t A_0 \quad (\text{A.13})$$

where

$$I = \rho_p A_0 (L_{ero} - L_{ela}) \dot{x}$$

L_{ero} is the remaining length of the projectile after the erosion phase previously described, and L_{ela} is the length of the projectile not yet influenced by the plastic wave at present time. Collecting the terms and simplifying yields

$$\frac{d}{dt} [\rho_p (L_{ero} - L_{ela}) \dot{x}] = \rho_p u_{plas} v + Y_D - R_t \quad (\text{A.14})$$

As L_{ero} is constant in this phase, taking the derivative yields

$$\rho_p (L_{ero} - L_{ela}) \ddot{x} - \rho_p \dot{x} \frac{d}{dt} L_{ela} = \rho_p u_{plas} v + Y_D - R_t \quad (\text{A.15})$$

Noticing that

$$\frac{d}{dt} L_{ela} = -u_{plas} \quad (\text{A.16})$$

and eq. A.15 can be rewritten as

$$\ddot{x} = \frac{1}{(L_{ero} - L_{ela})} \left[u_{plas} (v - \dot{x}) + \frac{1}{\rho_p} (Y_D - R_t) \right] \quad (\text{A.17})$$

which yields an equation that describes the deceleration of the projectile/armour interface during mushrooming.

During implementation of the model for the present case, it has been impossible to use the deceleration described in eq. A.17. The deceleration in the first instances of the mushrooming phase is so high, due to the first fraction containing the terms for the different in lengths, that the model breaks down without use of tuning parameters which is deemed indefensible. This is not clearly understood why, but it is known that the model of den Reijer is very complex and also account for target specific behaviour. It is unknown whether some specific terms from the target model neutralises this great acceleration in the special developed software by [den Reijer, 1991] named ALARM.

A modification of the model is therefore implemented, which is presented in the main report, section 3.4. This is a quick modification yielding a sufficient correlation between model and experiments, as seen in chapter 6.

The deceleration of the tail-end of the projectile is still as described in eq. A.10, and this concludes the mushrooming phase.

Rigid-body phase:

This is identical to what is stated in the main report.

In the final phase of the projectile penetration, the projectile behaves as a rigid-body. This phase begins when the velocity, v , of remaining elastic section of the projectile is equal to the velocity, \dot{x} , of the mushroom deformed part of the projectile.

As the projectile does not lose any mass during the above-described mushroom-phase, the mass of the projectile is equivalent to the mass of the projectile just after the erosion phase, $m_p = \rho_p A_0 L_{ero}$. The deceleration of the remainder of the projectile, now assumed completely rigid, is therefore given from Newton II as

$$\ddot{x} = \frac{R_t}{\rho_p L_{ero}} \tag{A.18}$$

which concludes the projectile penetration as developed by [den Reijer, 1991].

APPENDIX B

HARDNESS TEST

The following appendix chapter summarises the hardness tests performed on the projectiles and the target plate.

Cylindrical projectiles

A hardness test is performed on the cylindrical projectiles used in the experiments following a cut to 15 mm or 15,25 mm by a recession tool on a lathe. The hardness test is performed on the free tail/front surface of the projectile, as shown in figure B.1.

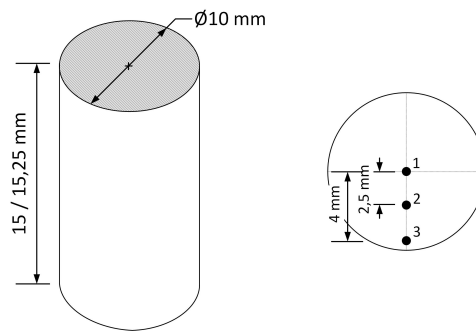


Figure B.1: *Points where the hardness tests were performed on the projectiles.*

Table B.1 summarises the hardness test results.

Hardness Test on Cylindrical Projectiles					
Brass:				Mean	S
HRB	82,1	83	82,2		
BHN	156	159	156	157	1,73
Aluminium:					
HRB	64,5	65,4	65,3		
BHN	115	116	116	116	0,577
Steel:					
HRB	95,2	96,6	96,1		
BHN	205	212	210	209	3,61
Plastic:					
HRH	47,4	44,2	45,3		
BHN	N/A	N/A	N/A		

Table B.1: *Table of hardness measurements. All are converted to brinell hardness for the 3000 kg/f scale. Notice, the plastic test is performed with the Rockwell H scale, but the hardness is lower than what is applicable for the brinell scale.*

Target plate

A single target plate of 12 mm steel is used for the impact tests. The steel plate has the marketing name Quardian. The testspecimen has been cut from an available plate of similar material, and heat effects from the cutting procedure has been minimised. Furthermore, a test of the ARMOX plates has likewise been conducted for determining similarities between the two brands. The test is shown in table B.2.

Hardness Test on Target plate								
Quardian 500:							Mean	S
HRC	45,8	47,4	48,2	46,5	45,7			
BHN	432	449	457	437	432	441	11,4	
ARMOX 500:						Mean	S	
HRC	48,1	47,4	47,2	47,1	48,5			
BHN	455	449	445	444	462	451	7,52	

Table B.2: *Table of hardness measurements. All are converted to brinell hardness for the 3000 kg/f scale. The ARMOX specimen is possibly heat affected.*

APPENDIX C

TENSILE AND COMPRESSION TEST

The following appendix chapter presents the material tests conducted on both the target plates, and the projectiles. The test are performed on the Tensile Testing Machine Zwick Z100 capable of applying a tension or compression force of 100 kN. Data sampling is conducted on a Spider 8-30. Afterwards, the data is used to approximate the material parameters needed in the models.

Tensile tests are performed on the target plates and compression tests are performed on the projectiles.

Tensile test of target plate

From the target plate, two test specimens are obtained with the purpose of verifying the table values from the manufacture.

The specimen is seen in figure C.1.

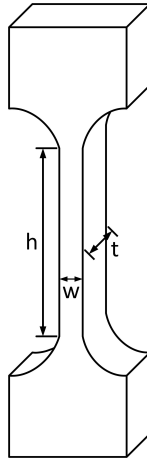


Figure C.1: *The used test specimen in the tensile tests.*

The test specimens are made of an Quardian 500 plate, and used for this test. Each specimen has the dimensions; $w = 5$ mm, $t = 8,14$ mm, $h = 77$ mm and a cross section area $A_0 = 40,7\text{mm}^2$

The test is shown in figure C.2.

The ultimate tensile strength was reached at $F_{tensile} = 66967,45$ N or 1645,39 MPa for the first test, and 1585,63 MPa in the second test. Furthermore, the modulus of elasticity was determined from the slope of the linear part in the second test with a clip-on extensometer to $E_t = 208$ GPa. This is consistent with the datasheet on the Quard 500 steel from Clabecq, [NLMK Clabecq, 2016].

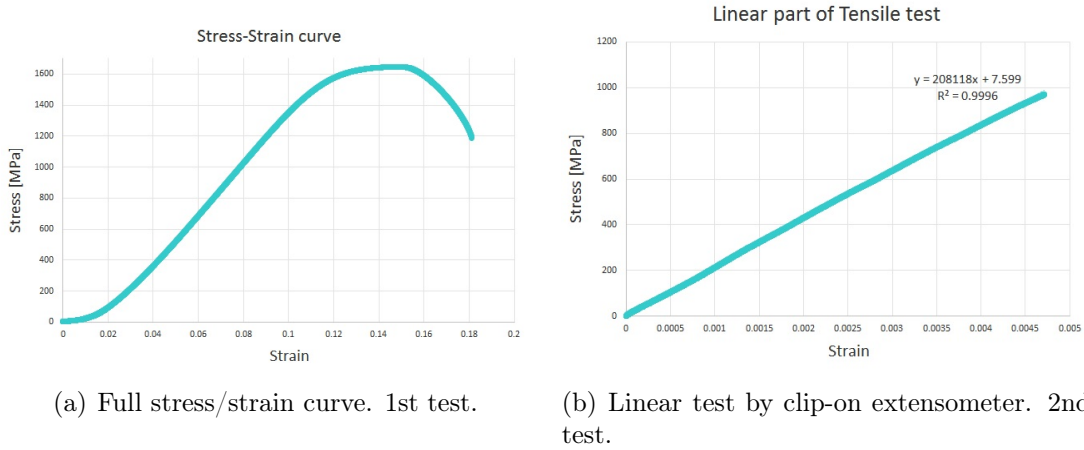


Figure C.2: *Stress-Strain curve for the Quardian target plate.*

Compression test on projectiles

A compression test is performed, as the rods used for the projectiles are not fit for a tensile test, and the principal load during impact is compression. The determination of the modulus of elasticity, and the plastic modulus from the obtained data, is not conducted as no clip-on extensometer is used, and the slopes are deemed unreliable or nonsense.

Steel

A single test is performed on the steel projectiles.

The test yields a proof strength of ≈ 725 MPa. The test is concluded before fracture, due to build in limitation of the machinery, to avoid overloading the load cell. The stress strain curve is given in figure C.3. The data is almost consistent with a heat-treated AISI 4340u steel, [Interlloy, 2016], which is the material used in the simulations, as far as these poor test suggests.

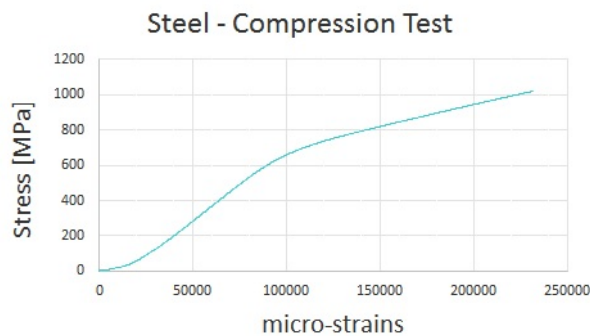
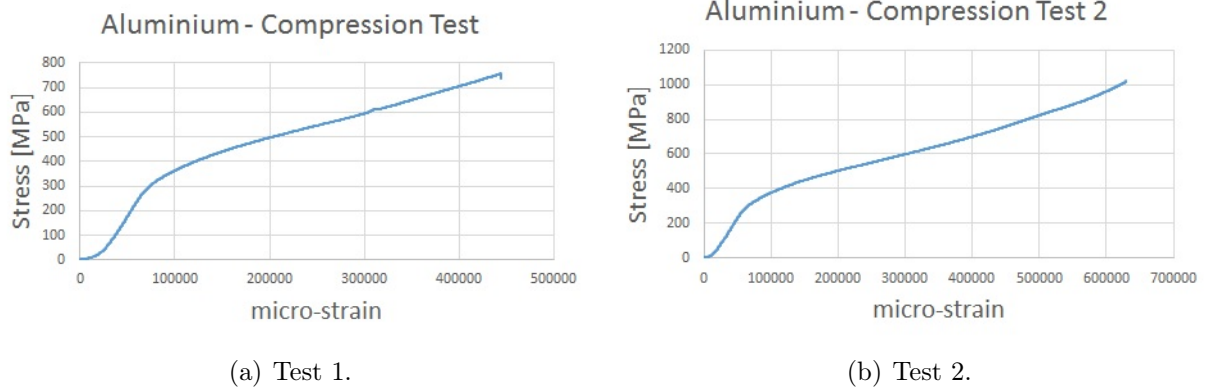


Figure C.3: *Compression test of steel projectile.*

Aluminium

Two tests on the aluminium projectiles are performed.

Test no. 1 yields a proof strength of 369 MPa. Test no. 2 yields a proof strength of 332 MPa. Both tests are aborted before fracture due to limits implemented, first by the group, and then the default limit in the machinery. The test are shown in figure C.4.



(c) Crack propagation in 45° slip plane due to compression. Limit of machinery reached before failure.

Figure C.4: *Compression test of aluminium projectiles.*

Brass

A single test of a brass projectile is conducted.

The test yields a proof strength of 471 MPa. The test is concluded in a fracture of the brass projectile. The test, and the fracture is seen in figure C.5. The test data is consistent with a known beta-brass, BS1400 HTB3, [Copper Alloys Ltd, 2016].

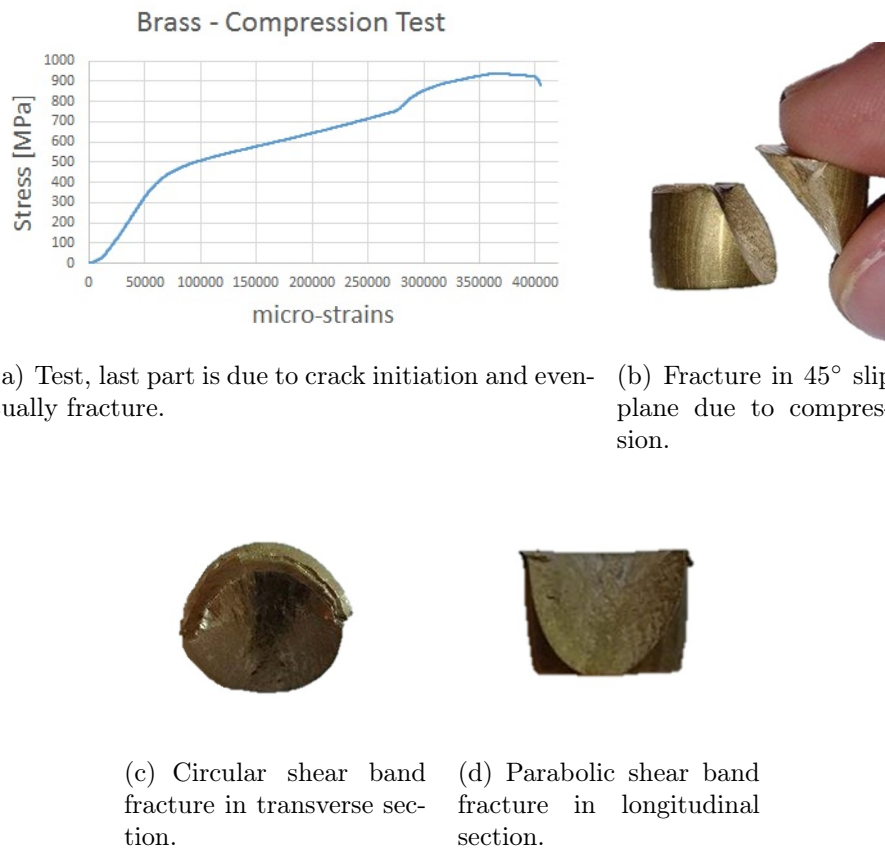


Figure C.5: *Compression test of brass projectile, leading to fracture.*

Approximation of the Linear Strain Hardening modulus

The projectiles are assumed to be linear elastic-plastic. This means, that they have a linear modulus of elasticity, and a linear modulus of plasticity or the Linear Strain Hardening modulus. As mentioned in the previous section, the determination of these modulus from the material data obtained is impossible, as the compression tests have been performed without extensometer and the slopes from the machine are too flat.

A common value of the modulus of elasticity E for each material is therefore used, and it is assessed that it is an acceptable assumption to do this.

The linear strain hardening modulus is approximated by using the Ramberg-Osgood equation for the tangent modulus, E_t . This modulus changes with each stress-increment. An average of the modulus values within the plastic zone of the test data shown in the section above is therefore taken as the linear strain hardening modulus. A stress-increment of 2 MPa is used.

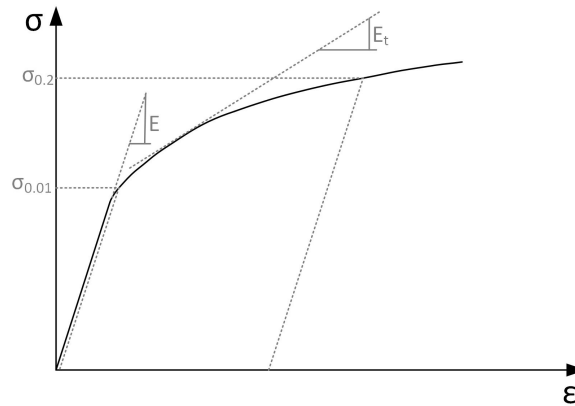


Figure C.6: *Tangent modulus, from Schneider et al. [2005].*

The original form of the Ramberg-Osgood equation is

$$\varepsilon = \frac{\sigma}{E} + 0,002 \left(\frac{\sigma}{\sigma_{0,2}} \right)^n \quad (\text{C.1})$$

where ε is the strain, σ is the stress, $\sigma_{0,2}$ is the proof strength from the test data, E is the assumed modulus of elasticity and n is the Ramberg-Osgood non-linearity exponent. The first term in the equation represents linear behaviour of the material, and the second term represent the non-linear behaviour of the material, [Schneider et al., 2005].

Using the $\sigma_{0,01}$ and $\sigma_{0,2}$ proof stresses, and the non-linear exponent can be approximated. A good correlation for at least aluminium and steel is seen with this, [Schneider et al., 2005].

$$n = \frac{\ln 20}{\ln \sigma_{0,2}/\sigma_{0,01}} \quad (\text{C.2})$$

where $\sigma_{0,01}$ is the 0,01% proof stress, see figure C.6.

The tangent modulus is defined as the slope for each value of stress on the stress-strain curve, and is derived from the Ramberg-Osgood equation as

$$E_t = \frac{E \sigma_{0,2}}{\sigma_{0,2} + 0,002 n E \left(\frac{\sigma}{\sigma_{0,2}} \right)^{n-1}} \quad (\text{C.3})$$

From eq. C.3 and eq. C.2 the following approximations of the linear strain hardening modulus for the different materials, table C.1, are obtained.

	Steel	Aluminium	Brass
Stress range approximated:	{725 - 1000} MPa	{340 - 1000} MPa	{340 - 739} MPa
Avg. tangent modulus:	3092 MPa	1288 MPa	2012 MPa

Table C.1: *Approximation of avg. tangent modulus in plastic zone of material test data.*

The determined values of the linear strain hardening modulus seems reasonable for similar materials in different studies. An extensive study on steels used in the naval industry showed that for a fast approximation, the linear plastic modulus can be taken as 1/65 of the elastic modulus, [Khedmati, 2000]. Using this approximation does in this case yield a $E_t = 3153$ MPa assuming a common value of the modulus of elasticity for steel is 205 GPa. The Ramberg-Osgood approximation is sufficiently close.

APPENDIX D

OBTAINING MATERIAL CONSTANTS USING NUMERICAL OPTIMISATION

The following appendix chapter presents a method for determining material constants for use in numerical simulations, hydrocode. The presented case is the Johnson-Cook strength model for ball bearing steel. Due note that this method is highly self fulfilling.

Method for obtaining material data

As mentioned in section 4.3.4, the cylindrical projectiles are modelled with materials found in the Ansys material library and yields nice results. At the start of this project the main projectile used for experiments was steel spheres from ball bearings. Non of the steel models in the Ansys material library fits the responds of the spheres at impact. A new material model for the ball bearing steel are therefore created. The ball bearing steel is modelled with a linear EOS of bulk modulus of same value as other steels in the library, the two independent components of linear elasticity only varies slightly between steel alloys and it is therefore considered to be sufficiently accurate. The Johnson-Cook strength model is also chosen for the ball bearing steel as experiments shows that they mainly behaved plasticly. Determining the constants in the Johnson-Cook model for a material is, as described in section 4.2.2, typically done through multiple experiments at different strain rates and temperatures.

Due to the size of the samples and lack of testing equipment the commonly used procedures are not possible. As the material model is used exclusively to model impacts at relatively low velocities at same size and shape, an alternative procedure is used. Four ball bearing spheres are shot into an ARMOX 500 plate at four different velocities, the axial deformation of each sphere is measured. Four axisymmetric simulations are set up in Ansys explicit dynamics, replicating the experiments and the deformations are determined for the spheres. The simulations are then connected to an optimisation scheme with A, B, n and C of the Johnson-Cook constants as parameters. The optimisation scheme used is Multi-Objective Genetic Algorithm (MOGA) in the Direct optimisation in Ansys Workbench. The melting temperature and the thermal exponent, m, are copied from other steels in the library, this is justified due to relatively low temperature increase during experiments. The found and applied values of the material parameters are shown in table D.1.

This method is simple and easily applicable for this kind of experiments. It is however also self fulfilling in the sense that the optimisation ensures that the simulations fits with the experiments. It is of cause the purpose with the simulations to mimic the real world, but model data obtained by this method should be used with care. It is unknown whether the constants obtained, Initial Yield Stress, Hardening Constant, etc., actually are the real constants for the specific material or that this particular combination just happens to make the simulations fit the experimental data. To obtain proper material constants, multiple different experiments must be conducted and preferably some where effects can

APPENDIX D. OBTAINING MATERIAL CONSTANTS USING NUMERICAL OPTIMISATION

Parameter	Value	Unit
Density	7750	$\frac{kg}{m^3}$
Specific Heat	477	$\frac{kJ}{kg^\circ C}$
Bulk Modulus	159000	MPa
Shear Modulus	81800	MPa
Initial Yield Stress (A)	2261,3	MPa
Hardening Constant (B)	514,47	MPa
Hardening Exponent (n)	0,29999	
Strain Rate Constant (C)	0,024337	
Thermal Softening Exponent (m)	1	
Melting Temperature (T_{melt})	1490	$^\circ C$
Reference Strain Rate ($\dot{\epsilon}_0$)	1	s^{-1}

Table D.1: *Material parameters for the ball bearing steel.*

be isolated and determined directly.

ANNEX

List of annex content

Matlab files

- **Stress_Destribition_Mushrooming.m** - Is the script containing the analytical model developed by the group.
- **Dynamic_Stress.m** - Is a function for determining the dynamic yield stress used by **Stress_Destribition_Mushrooming.m**.
- **ModifieddenReijerModel.m** - Is the script containing the modified den Reijer model.

Ansys files

- **SteelCylinderOnArmox3D.wbpz** - Contains the full 3D simulation used for comparison with axisymmetric in the section 4.3.1.
- **LagrangeConvergenceStudy.wbpz** - Contains the simulations used for the convergence study in section 4.3.2.
- **SteelCylinderOnArmoxAxisymmetric.wbpz** - Contains the simulation used for comparison with full 3D and for the final study mimicking the experiments with steel projectiles.
- **AluminiumCylinderOnArmoxAxisymmetric.wbpz** - Contains the simulations for the final study mimicking the experiments with aluminium projectiles.
- **SphearSteelAndArmox500T.xml** - Contains the material model for ARMOX 500 from [SSAB Oxelösund AB, 2007] and the material model found in appendix D

Videos from the high speed camera

Videos recorded with the high speed camera are included for reference. Each video file are followed with a data file containing camera settings and video statistics. Not all experiments were capture by the camera.

NB. In VLC media player E can be used to step forward one frame at a time.

Pictures of projectiles after impact

Pictures/Images of the projectiles used in the test-campaign after impact. A portrait and detail images when needed.